

HU ISSN 1586–2070

JOURNAL OF COMPUTATIONAL AND APPLIED MECHANICS

A Publication of the University of Miskolc

VOLUME 7, NUMBER 2 (2006)



MISKOLC UNIVERSITY PRESS

HU ISSN 1586–2070

JOURNAL OF COMPUTATIONAL AND APPLIED MECHANICS

A Publication of the University of Miskolc

VOLUME 7, NUMBER 2 (2006)



MISKOLC UNIVERSITY PRESS

EDITORIAL BOARD

- István PÁCZELT**, Editor in Chief, Department of Mechanics, University of Miskolc, 3515 MISKOLC, Hungary, mechpacz@uni-miskolc.hu
- László BARANYI, Department of Fluid and Heat Engineering, University of Miskolc, 3515 MISKOLC, Hungary, aramb@uni-miskolc.hu
- Edgár BERTÓTI, Department of Mechanics, University of Miskolc, 3515 MISKOLC, Hungary, mechber@uni-miskolc.hu
- Tibor CZIBERE, Department of Fluid and Heat Engineering, University of Miskolc, 3515 MISKOLC, Hungary, aramct@uni-miskolc.hu
- István ECSEDI, Department of Mechanics, University of Miskolc, 3515 MISKOLC, Hungary, mechecs@uni-miskolc.hu
- Wolfram FRANK, Institut für Fluid- und Thermodynamik, Universität Siegen, Paul-Bonatz-Strasse 9-11, 57076 SIEGEN, Germany, frank@ift.mb.uni-siegen.de
- Ulrich GABBERT, Institut für Mechanik, Otto-von-Guericke-Universität Magdeburg, Universitätsplatz 2, 39106 MAGDEBURG, Germany, ulrich.gabbert@mb.uni-magdeburg.de
- Zsolt GÁSPÁR, Department of Structural Mechanics, Budapest University of Technology and Economics, Műegyetem rkp. 3, 1111 BUDAPEST, Hungary, gaspar@ep-mech.me.bme.hu
- Robert HABER, Department of Theoretical and Applied Mechanics, University of Illinois at Urbana-Champaign, 216 Talbot Lab., 104 S. Wright Str., URBANA, IL 61801, USA, r-haber@uiuc.edu
- Gábor HALÁSZ, Department of Hydraulic Machines, Budapest University of Technology and Economics, Műegyetem rkp. 3, 1111 BUDAPEST, Hungary, HALASZ@vizgep.bme.hu
- Ji Huan HE, Department of Mathematics, College of Basic Science, Shanghai Donghua University, No. 1882 Yan'anxilu Road, 200051 SHANGHAI, China, jhhe@dhu.edu.cn
- Károly JÁRMAI, Department of Materials Handling and Logistics, University of Miskolc, 3515 MISKOLC, Hungary, altjar@uni-miskolc.hu
- László KOLLÁR, Department of Strength of Materials and Structures, Budapest University of Technology and Economics, Műegyetem rkpt. 3. K.II.42., 1521 BUDAPEST, Hungary, lkollar@eik.bme.hu
- Vladimir KOMPIŠ, Department of Mechanics, Faculty of Mechanical Engineering, University of Žilina, ŽILINA, Slovakia, kompiv@fstroj.utc.sk
- Imre KOZÁK, Department of Mechanics, University of Miskolc, 3515 MISKOLC, Hungary, mechkoz@uni-miskolc.hu
- József KÖVECSES, Mechanical Engineering Department, Mc Gill University, 817 Sherbrooke Street West, MD163 Montreal, Quebec H3A 2K6, jozsef.kovecses@mcgill.ca
- Márta KURUTZ, Department of Structural Mechanics, Budapest University of Technology and Economics, Műegyetem rkp. 3, 1111 BUDAPEST, Hungary, kurutzm@eik.bme.hu
- R. Ivan LEWIS, Room 2-16 Bruce Building, Newcastle University, NEWCASTLE UPON TYNE, NE1 7RU, UK, R.I.Lewis@NCL.AC.UK
- Gennadij LVOV, Department of Mechanics, Kharkov Polytechnical Institute, 2 Frunze Str., 310002 KHARKOV, Ukraine, lvovgi@kpi.kharkov.ua
- Herbert MANG, Institute for Strength of Materials, University of Technology, Karlsplatz 13, 1040 VIENNA, Austria, Herbert.Mang@tuwien.ac.at
- Zenon MROZ, Polish Academy of Sciences, Institute of Fundamental Technological Research, Swietokrzyska 21, WARSAW, Poland, zmroz@ippt.gov.pl
- Tibor NAGY, Department of Physics, University of Miskolc, 3515 MISKOLC, Hungary, fiznagyt@uni-miskolc.hu
- Gyula PATKÓ, Department of Machine Tools, University of Miskolc, 3515 MISKOLC, Hungary, mechpgy@uni-miskolc.hu
- Jan SLADEK, Ústav stavbenictva a architektúry, Slovenskej akadémie vied, Dubróvska cesta 9, 842 20 BRATISLAVA, Slovakia, usarslad@savba.sk
- Gábor STÉPÁN, Department of Mechanics, Budapest University of Technology and Economics, Műegyetem rkp. 3, 1111 BUDAPEST, Hungary, stepan@mm.bme.hu
- Barna SZABÓ, Center for Computational Mechanics, Washington University, Campus Box 1129, St. LOUIS, MO63130, USA, szabo@me.wustl.edu
- Szilárd SZABÓ, Department of Fluid and Heat Engineering, University of Miskolc, 3515 MISKOLC, Hungary, aram2xs@uni-miskolc.hu
- György SZEIDL, Department of Mechanics, University of Miskolc, 3515 MISKOLC, Hungary, Gyorgy.SZEIDL@uni-miskolc.hu

LOCAL EDITORIAL COUNCIL

T. CZIBERE, I. KOZÁK, I. PÁCZELT, G. PATKÓ, G. SZEIDL

EVALUATION OF LOAD CONTROL END-FEED IN HYDROFORMING OF PRE-BENT DP600 STEEL TUBE USING THE EXTENDED STRESS-BASED FORMING LIMIT CURVE (XSFLC) FAILURE CRITERION

ALEXANDER BARDELICK AND MICHAEL J. WORSWICK
Department of Mechanical Engineering, University of Waterloo
Waterloo, Ontario, Canada, N2L 3G1
abardelc@engmail.uwaterloo.ca

[Received: November 21, 2005]

Abstract. The work presented in this paper utilizes advanced finite element models of the pre-bending and hydroforming processes to investigate the effect of load control end-feed (EF) on the formability of DP600 steel tube in hydroforming. A model of a rotary-draw tube bender was used to simulate pre-bending. Validation of the pre-bending model showed good agreement with the pre-bending experiments. The hydroforming process was also successfully modelled and validated for a zero EF case. Increasing levels of EF were simulated and the corner-fill expansion of the tube was measured to assess the formability of the tube. The new and fully three dimensional Extended Stress-Based Forming Limit Curve (XSFLC) failure criterion was used to predict the onset of necking in the hydroforming simulations. In addition to varying the level of end-feed, two different pressurization schemes were investigated. The models showed that an increase in end-feed improved formability during hydroforming and also sensitivity to pressurization scheme was shown.

Mathematical Subject Classification: 74A10, 74S05

Keywords: hydroforming, stress-based failure criterion, load control end-feed, formability, tube bending

1. Introduction

With increasing fuel costs and the negative impact current automobiles have on the environment, a need to reduce their weight is apparent. One method this can be realized is through the use of hydroforming to manufacture conventional automobile components. The hydroforming process is shown in a simplified schematic (Figure 1) and consists of (a) enclosing a circular tube within a die of different cross-section, (b) pressurizing the tube and (c) expanding the tube to conform to the cross-section of the die.

Hydroforming an automotive structural component from a continuously bent steel tube possesses the following advantages over traditionally stamped and welded parts [1, 2]:

- Weight reduction (improved fuel efficiency)
- Improved strength and stiffness due to work hardening of the tube

- Part consolidation
- Reduced scrap

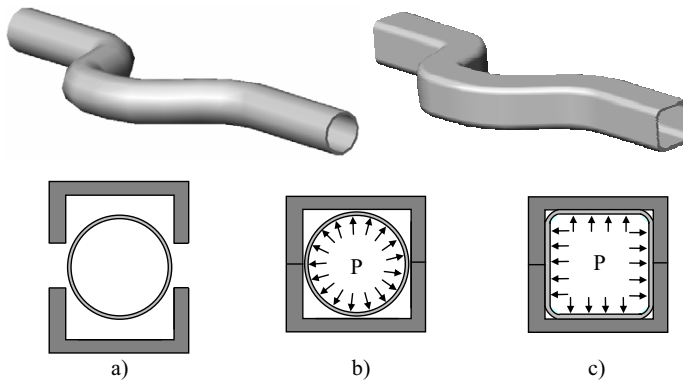


Figure 1. Hydroforming process schematic [3]

Currently, hydroforming is being used by industry to manufacture the typical structural components shown in Figure 2.

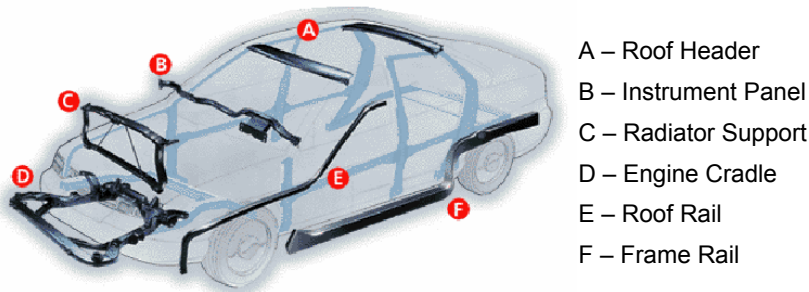


Figure 2. Examples of hydroformed structural components [4]

The main advantage of hydroformed components (weight reduction) can be further improved through the use of high-strength steels. By using high-strength steels, the wall thickness of a hydroformed component can be reduced while strength is maintained. The main challenge encountered when using high-strength steels in hydroforming applications is the limited ductility/formability of these materials. The low formability of high-strength steels limits the practicality of the hydroformed part due to the low degree of corner-fill expansion (CFE) that can be achieved. Low CFE is due to premature failure of the tube by fracture (burst). This is particularly true for DP600 and is the main motivation behind the research activities at the University of Waterloo.

A fully instrumented Eagle EPT-75 servo-hydraulic mandrel-rotary draw tube bender with an R/D (centre-line bend radius to tube diameter) ratio of 2.0 is used to accurately control bend process parameters. The tubes considered for this work are electric resistance seam welded with an initial OD of 76.2 mm (3.0") with a thickness of 1.85 mm. In pre-bending, tubes were bent to a final angle of 90° . Hydroforming experiments were conducted using a 1,000 Ton press. The bent tubes are hydroformed in a square cross-section die. The formability is quantified by measuring the corner-fill expansion of the tube in the die. To overcome the low formability inherent to high-strength steels, end-feed (EF) during hydroforming was implemented. End-feed refers to the application of a compressive axial force along the longitudinal direction of the tube during hydroforming. It pushes the tube into the expansion zone, allowing more material to be available for expansion. Hydraulic actuators are used to apply a maximum of 240 kip EF force during hydroforming. Load control EF applies a controlled load to the tube ends during internal pressurization. Another method of applying EF is through displacement control, where the stroke of the EF actuator is controlled.

Finite element (FE) models provide valuable insight into experimental work and help predict trends and process parameters before experiments are designed. The dynamic explicit code, LS-DYNA v970, was used to develop all of the FE models for this paper. A new failure criterion coupled with LS-DYNA was developed at the University of Waterloo and used to model (with exception to springback) the bending, die-close and hydroforming processes. The material properties and friction characteristics were determined experimentally and used as input for the FE simulations. Different levels of EF load and two internal pressurization schemes were investigated for this work.

1.1. Axial Members. Much of the published work on the effects of hydroforming EF on the formability of steel and aluminium tubes is focused on axial members only. The common hydroforming equipment used in these experiments is shown in Figure 3. Ahmetoglu et al. [5] used FE computation to show an increase in formability of low carbon steel tubes due to a 10% increase in EF stroke using displacement control. Their results also showed reduced thinning, increased thickening and greater final forming pressure. A thin walled axisymmetrical shell model was used by Kim et al. [6] to develop an analytical model which showed that a loading path with increased compressive load (using load control) in the axial direction improved the circumferential expansion of an aluminium tube. The experimental work of Thiruvaudchelvan et al. [7] on aluminium tubes showed that by increasing EF using load control, the EF displacement increased by 42% while the radial expansion and failure pressure increased by 8% and 5%, respectively.

The three dominant failure modes encountered during hydroforming are buckling, wrinkling and fracture (burst) [1, 3, 5, 6, 7, 8, 9]. Figure 4 (a) shows the failure modes. Buckling usually occurs at the beginning of the hydroforming process when there is excessive EF force (increased compressive stress in the longitudinal direction) applied to the tube. Similarly, wrinkling occurs symmetrically along the longitudinal axis of the tube and is also caused by an excessive EF force. Although major wrinkles are

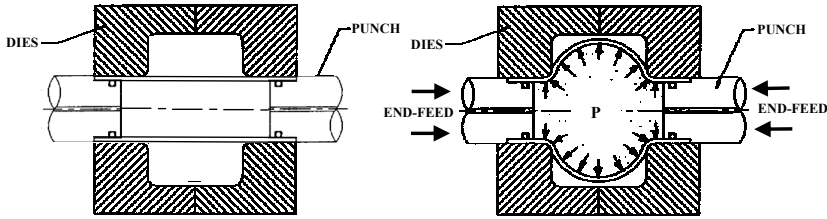


Figure 3. Axial hydroforming with EF [7]

undesirable, minor wrinkles are sometimes created during the hydroforming process and later ironed out with an increase of internal pressure. Fracture occurs due to an excessively high internal pressure which creates high tensile stresses in the tube due to the reduction (caused by friction between tube and die) of material flow into the die cavity [8, 9, 10]. The process parameters involved in successful hydroforming are critical and can be summarized in the axial force versus internal pressure process diagram found in Figure 4 (b) and (c). Analytical [6, 8, 11] and experimental [9] methods have been used to derive these process diagrams and serve as design tools for engineers. Through the use of a validated failure criterion, numerical simulations can also be used to derive process diagrams.

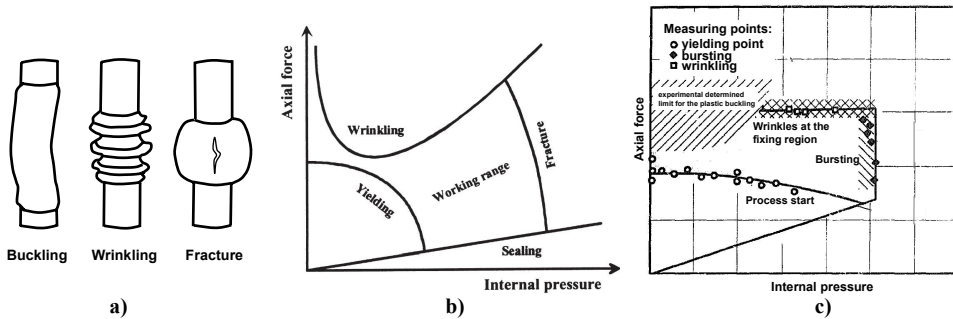


Figure 4. a) failure modes b) general process diagram [8] and c) experimentally derived process diagram [9]

1.2. Pre-Bent Members. The majority of commercial hydroformed components are created from pre-bent tubular members (Figure 2). The major difference between axial and pre-bent hydroforming is the non-symmetric bending axis. Depending on the bending parameters, tensile strains in the range of 20% - 30% are imposed at the outside radius of the bend and compressive strains of the same magnitude are seen at the inside bend radius for a 90° pre-bent tube [1, 3, 12, 13]. To the authors' knowledge, there have been no publications on experimental or analytical work done on the effects of EF on the formability of hydroformed pre-bent tubes. The extent of the published work in this field is simulation based. The numerical trends have shown that increased

EF improves the formability of the hydroformed part by increasing the CFE and reducing thinning using both displacement [12] and load control [14]. Although the trends show improvements in formability, a more accurate failure criterion must be used in these simulations. The same failure modes shown in Figure 4 (a) are also present for pre-bent tubes, but are too difficult to analytically predict due to pre-bending. Therefore, experimental and numerical methods must be used to determine the process diagrams for pre-bent hydroformed tubes.

1.3. Numerical Failure Criterion. In numerical hydroforming simulations of axial members, many failure criteria exist with the stress-based FLD (σ FLD) criterion developed by Stoughton [15] gaining the most attention by the metal forming industry. This criterion was developed to overcome the monotonic strain path dependence of the traditional strain-based FLD (ϵ FLD). The σ FLD is constructed from the ϵ FLD, and is based on a plane-stress assumption. This criterion was validated for free-expansion (tube expands freely and does not conform to a die) experiments with AKDQ steel tubes [16] and showed excellent agreement. This approach does not consider the through-thickness stress component that is present when a tube is hydroformed in an enclosed die. Hydroforming experiments at the University of Waterloo are conducted on pre-bent tubes in enclosed hydroforming dies (Figure 5). Experiments have consistently shown that the fracture (burst) location for hydroformed tubes (zero EF) is at the tube/die contact area, not in the free-expansion zone. This was the motivation behind the development of the new Extended Stress-Based Forming Limit Curve (XSFLC) failure criterion by Simha et al. [17, 18], which is a full three-dimensional stress-based failure criteria.

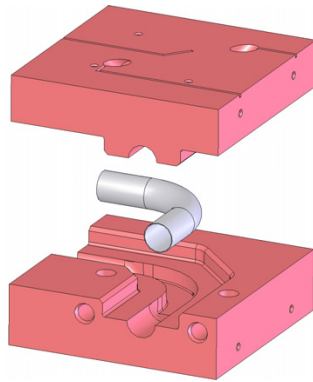


Figure 5. Pre-bent hydroforming dies at the University of Waterloo

2. Tube Bending Model

2.1. Mandrel Rotary-Draw Tube Bending Process. The fully instrumented Eagle EPT-75 servo-hydraulic mandrel rotary-draw tube bender at the University of Waterloo was used to experimentally bend the tubes and was modelled for the tube

bending simulations. The repeatability for this method of bending has been shown to be consistent by Bardelcik et al. [13] and Dwyer et al. [19]. Figure 6 shows the experimental tube bender and a schematic of the tools involved in the tube bending process.

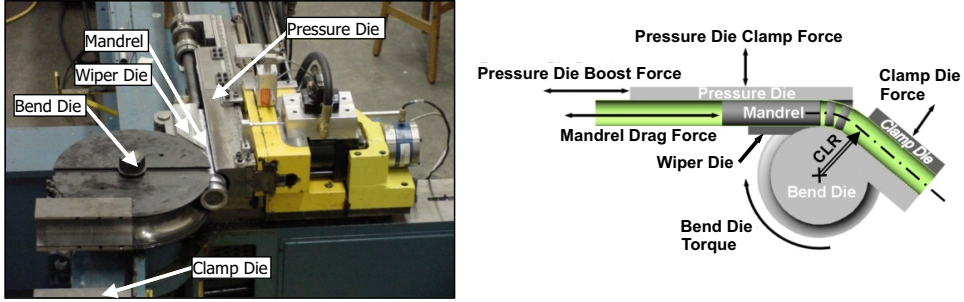


Figure 6. Experimental mandrel rotary-draw tube bender and schematic [3]

The bend die and clamp die hold the end of the tube and rotate together. This action draws the tube around the bend die. The moment created at the left end of the tube during the bending process is reacted by the pressure die. Also, the pressure die can be used to apply boost during the bending process to change the strain distribution along the tube [13]. A flexible two-ball mandrel supports the tube and prevents collapse of the tube during bending. Wrinkling of the inside bend radius is prevented by the wiper die which also reacts to some of the pressure die clamp force.

2.2. Material Characterization. In order to successfully simulate the pre-bending and hydroforming process, accurate representations of the DP600 material properties and friction characteristics are necessary. The uniaxial tensile test was used to measure the stress-strain response of the DP600 and the twist-compression test (TCT) [20, 21] provided the frictional characteristics.

2.2.1. Tensile Testing. The material model used to simulate the DP600 tube material was based on the standard uniaxial tensile test. The tensile test specimens were cut along the longitudinal direction of the tube and from different orientation along the circumference (Figure 7). It was found that specimens from the 3 and 9 o'clock positions resulted in identical material properties while the 6 o'clock position showed a slightly higher yield stress due to additional work hardening from the roll forming process [1, 3]. The engineering stress-strain curves were converted into true stress-strain curves and averaged to produce the following power law relation [12],

$$\bar{\sigma} = 795.8\bar{\epsilon}^{0.115} \quad (2.1)$$

This curve was then converted into a true stress vs. plastic strain curve. The true stress vs. plastic strain curve was extrapolated to (0.60 mm/mm, 943 MPa) and

used as the input curve for the FE simulations. A more accurate representation of the stress-strain behaviour for the tube material would be to conduct free-expansion bulge tests as proposed by Fuchizawa et al. [22].

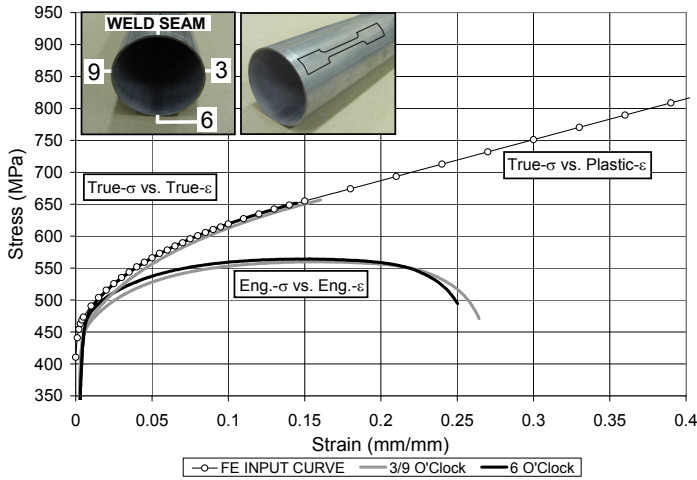


Figure 7. Tensile test results for DP600

2.2.2. *Twist-Compression Test.* The twist-compression test (TCT) is a common bench test used to determine the coefficient of friction (COF) between two flat surfaces. In the TCT, a sheet metal specimen is pressed and rotated against a flat tool steel cup. The torque developed at the interface is measured and with the interfacial pressure the static and dynamic COF is calculated (Figure 8) [20, 21]. The relative velocity between the tube and die during the forming process is replicated in the test. The sheet metal specimen used for these tests was cut from the same coil that was used to roll form the DP600 tubes. The tool steel cups are made from the same material as the bending and hydroforming dies and were heat treated to the same specifications. For the tube bender, cups made from nitrided 4130 steel represent the bend, clamp and pressure die, while the wiper die cup is made from untreated 4130 steel. The hydroforming die cups are made from untreated P20 tool steel.

The interfacial pressure seen by the tools during the experiments was estimated to select the appropriate COF from Figure 8. Table 1 summarizes the lubricants and resulting COF that were used in the FE penalty-based contact models.

	Bend Die	Pressure Die	Wiper Die	Clamp Die	Mandrel	Hydroforming Die
Lubricant	Dry	Dry	D.A. Stuart-Hydrodraw 615	Dry	D.A. Stuart-Hydrodraw 615	D.A. Stuart-Hydrodraw 625
COF	0.08	0.08	0.08	0.08	0.06	0.03

Table 1. Lubricants and resulting COF used for contact algorithms

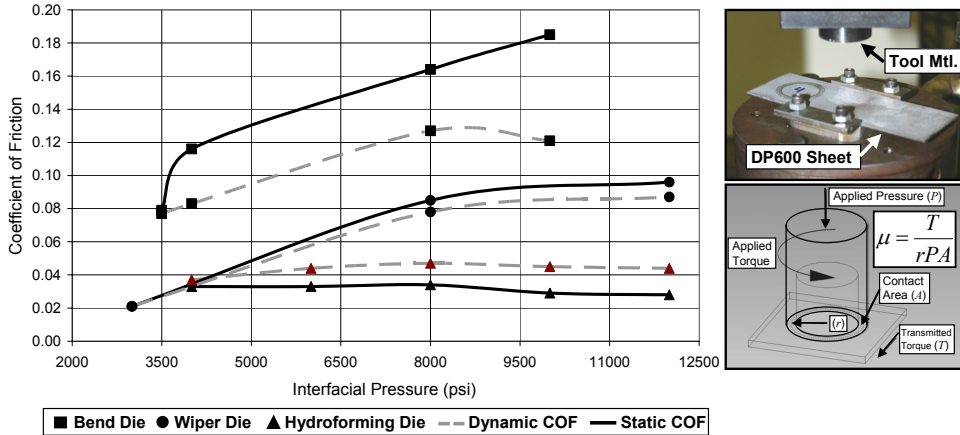


Figure 8. Twist compression test results

2.3. Numerical Model. The mandrel rotary-draw tube bending simulation was developed using LS-DYNA v970. One-half of the model was simulated. The tube bender tools were modelled as rigid surfaces with 4-noded shell elements. The tube was meshed with 8-noded solid elements. Five through-thickness elements were used to represent the tube. A coarse and fine mesh was used for the tube to reduce computational time. A total of 83,000 solid elements were used to model the tube. Figure 9 shows the bender and tube meshes used in the simulations. The bend model was run over 30 milliseconds and required 88.2 hours of processor time. After bending, a springback simulation, which used implicit integration, was carried out. After springback, the tube was trimmed and a die-close simulation was run to prepare the model for hydroforming simulations. The elemental stress and strain histories were transferred to all successive computations to account for the loading history of the elements from the previous deformation.

2.4. Bending Results. To validate the bending model, strain and thickness at different locations along the tube were compared to experimental results. The validation data was compared along the inside and outside of the bend (θ) and around the circumference of the tube (ϕ) at the 45° position (Figure 10). Engineering strains were measured at the outside surface of the tube using circle grid analysis and thickness was measured with an ultrasonic gauge. The inside and outside of bend measurements begin at the mandrel end $\theta = 0^\circ$ and finish at the clamp end $\theta = 90^\circ$. For $\theta < 0^\circ$ and $\theta > 90^\circ$, the measurements were along the straight section of tube and are shown for completeness as they do not correspond to an angle. The measurements made at the 45° position begin at the weld seam $\phi = 0^\circ$ and continue 360° around the tube in the direction indicated in Figure 10.

The experimental and numerical strain and thickness distribution results are shown in Figure 11. Experimental strain distributions for the three different measurement locations are shown as an averaged curve-fit (measured from three tubes) 6th order

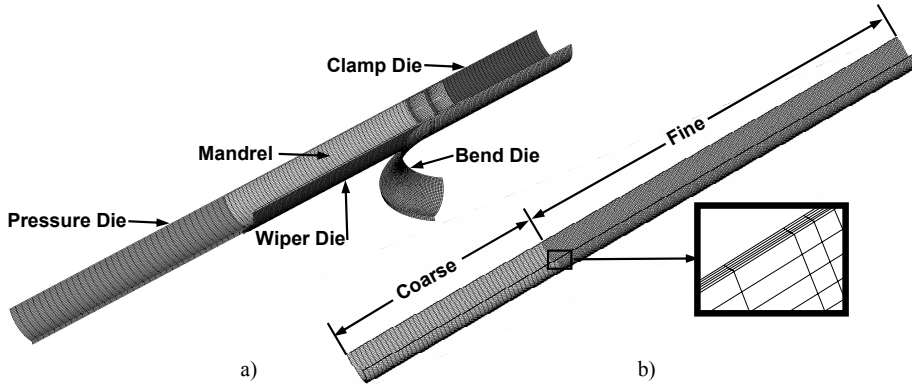


Figure 9. a) tube bender mesh b) tube mesh, not to scale

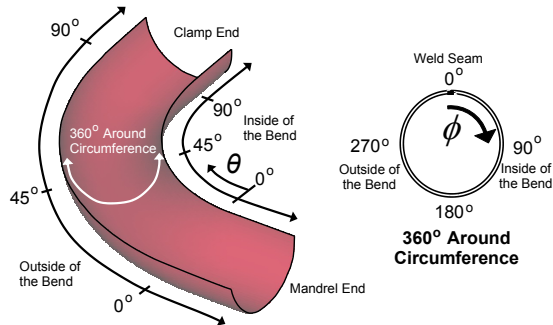


Figure 10. Strain and thickness measurement locations [12]

polynomial line. The experimental error bars represent the 3.0% strain scatter of the circle grid analysis results. The accuracy of the thickness results is 0.001 mm; therefore no error bars are shown. Experimental results were recorded approximately every 3.0° . Numerical results were manually extracted from the model using post-processor software at 10° increments.

2.4.1. *Outside of the Bend Region.* For the outside of the bend region, the major (tensile) strain is in the longitudinal direction of the tube and is the sum of the membrane and bending strain. The minor (compressive) strain occurs in the hoop direction of the tube. Figure 11 (a) shows that experimentally, the steady-state region $20^\circ < \theta < 70^\circ$ experiences an average of 26.0% major strain with a peak of 28.1% at 65° , while the steady-state minor strain is approximately -5.0%. Numerically, the average major strain is 24.2% for the steady-state region with no peak and the steady-state minor strain is -7.0%. With the exception of the peak strain not being captured by the model, the experimental and numerical strain distributions show good agreement.

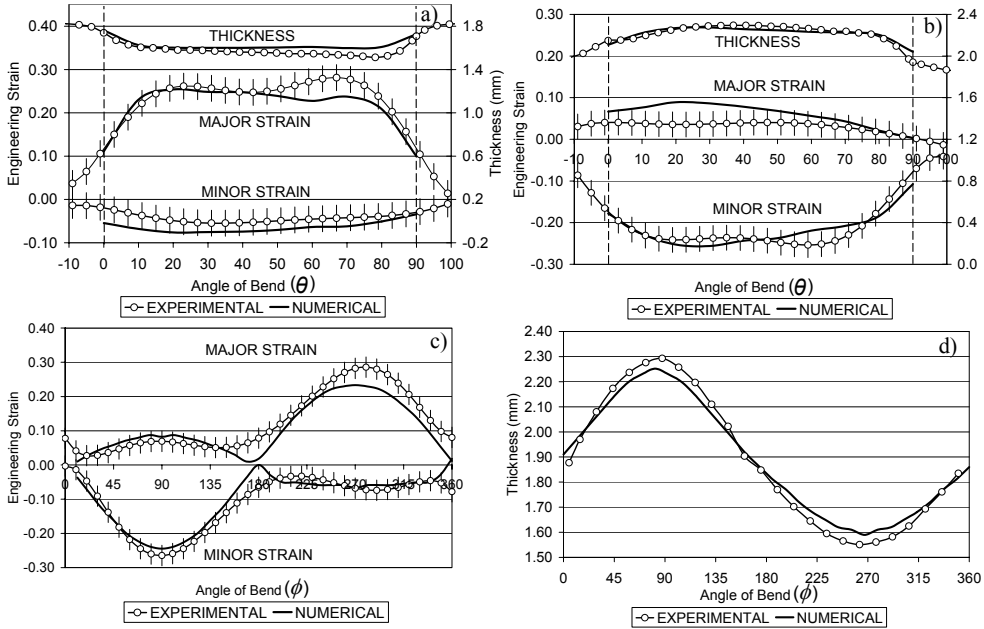


Figure 11. Strain and thickness distribution results for a) outside of the bend, b) inside of the bend, c) and d) 360° around the circumference at 45°

Due to the major strain, thickness is reduced at the outside of the bend. Experimentally, the average steady-state thickness is 1.56 mm (15.7% thinning), while the numerical models predicted a thickness of 1.60 mm (13.5% thinning). Again, the experimental and numerical thickness distributions show good agreement with each other.

2.4.2. Inside of the Bend Region. In this case, the minor (compressive) strain is dominant and along the longitudinal direction of the tube (Figure 11 (b)). It is also the sum of the membrane and bending strain. The minor (tensile) strain occurs in the hoop direction. The experimental steady-state region experiences an average major strain of 3.8% and an average minor strain of -24.3%, while the numerical models predict an average major strain of 7.0% and an average minor strain of -23.6%. The experimental and numerical strain distributions show good agreement.

Due to the large minor strain, thickening occurs at the inside of the bend and the experimental and numerical steady-state average thickness results agree at 2.25 mm (21.6% thickening), showing excellent agreement.

2.4.3. 360° Around the Circumference. Figure 11 (c) shows the strain measured around the tube circumference at $\theta = 45^\circ$. For $0^\circ < \phi < 180^\circ$, the major strain corresponds to the hoop strain and the minor strain is in the longitudinal direction. For $180^\circ < \phi < 360^\circ$, the major and minor strains reverse and the major strain occurs in

the longitudinal direction since the bending strain is now tensile. The agreement between the two distributions is very good with a slight discrepancy at the 270° position where the experimental strain is greater than the numerical strain.

The thickness distribution follows a sinusoidal trend (Figure 11 (d)) and shows a peak in thickening at the 90° position and thinning at 270°. Although there is a slight underprediction of thickening and thinning by the numerical model, the agreement is acceptable.

3. Hydroforming Model

3.1. Hydroforming Process. Hydroforming experiments are conducted on a 1,000 Ton press at the University of Waterloo. Figure 12 shows the hydroforming die and EF actuator that are used for the experiments. The EF actuators are hydraulic with 250 kip capacity each. For hydroforming, the EF actuator rams are inserted into each end of the pre-bent tube until the shoulder engages the edge of the tube (Figure 12). A polymeric o-ring is used to create a seal between the ram and the inside diameter of the tube. This sealing concept is easy to model and minimizes friction in the seal region of the tube. A zero EF case was hydroformed experimentally and simulated numerically. In this case, the ram remains stationary and provides no EF force to the end of the tube. For the case of load control EF, only numerical models were simulated with EF loads of 5, 10, 20 and 30 kip.

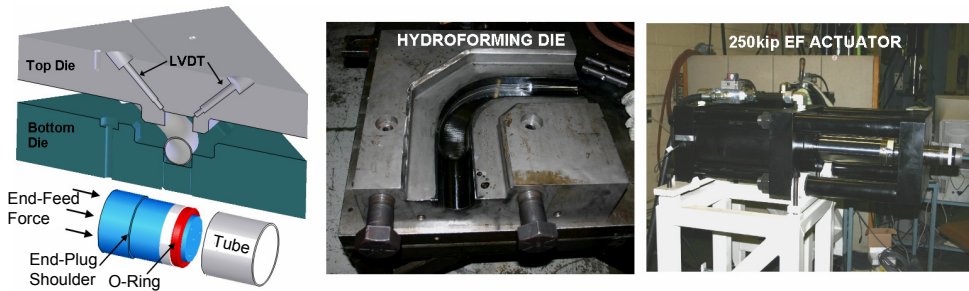


Figure 12. Hydroforming die and EF actuator

3.2. Formability Measurement. To evaluate the formability of a hydroformed tube, CFE was measured. Figure 12 shows a CAD solid model cutaway of the hydroforming die. Two linear variable displacement transducers (LVDT) are located on the inside and outside of the bend at $\theta = 45^\circ$ and $\phi = 45^\circ, 315^\circ$. They are used to measure the corner expansion of the tube.

The following equation is used to calculate the %CFE using the Figure 13 section,

$$\%CFE = \frac{14.83 - d}{14.83} \times 100\% \quad (3.1)$$

where d is in mm.

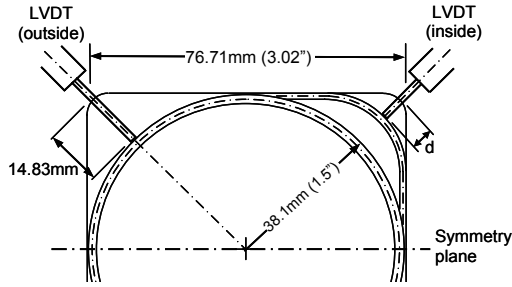


Figure 13. CFE measurement location section [12]

As d approaches zero, the CFE becomes 100%, which indicates a fully formed tube. It is possible to have 'negative CFE'. This is due to tube ovalization during bending or movement of the tube during hydroforming [3, 13]. Due to differences in expansion at the inside and outside of the bend LVDT's, the diametrical corner-fill expansion (DCFE) is also calculated (due to symmetry plane) to quantify the overall formability of the tube,

$$\%DCFE = \frac{\%CFE_{inside} + \%CFE_{outside}}{2} \quad (3.2)$$

3.3. Numerical Model. Similar to the bending model, the hydroforming die and EF rams were modelled as rigid surfaces with 4-noded shell elements (Figure 14). Also, the LVDT's shown in Figure 12 were modelled as a single beam and shell element and can be seen in Figure 14. To simulate the internal pressurization of the tube, a very thin shell mesh was created on the inside diameter tube surface. The nodes between the thin shell mesh and and tube surface were coincident.

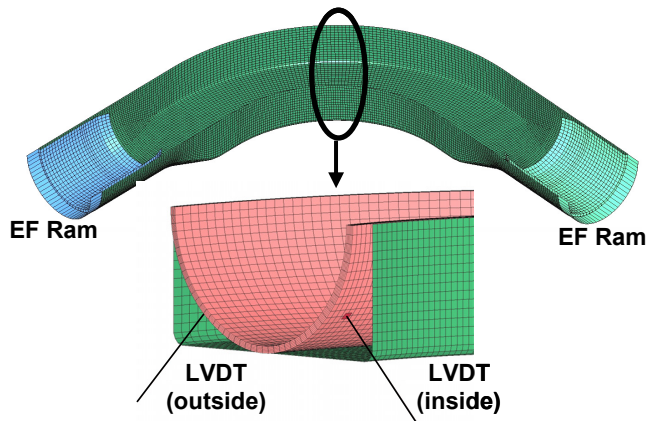


Figure 14. Meshed hydroforming tools and LVDT's

3.3.1. *XSFLC Failure Criterion.* This section briefly describes the theory which supports the XSFLC. For a more rigorous derivation, refer to [18]. The XSFLC is based on the traditional strain-based forming limit (ϵ FLC) curve, as proposed by Keeler et al. [23] and Goodwin [24]. The ϵ FLC curve plots major principle strain (ϵ_1) vs. minor principle strain (ϵ_2) at the onset of necking and is derived from plane-stress experiments. No ϵ FLC was available for the DP600 material; therefore it was approximated using the findings of Keeler and Brazier [25]. The shape of the curve is given and the plain strain intercept (FLC_o) is approximated using the materials' strain hardening exponent, n , and sheet thickness, t .

$$FLC_o(\%) = (23.3 + 14.14t) \left(\frac{n}{0.21} \right). \quad (3.3)$$

The ϵ FLC for the DP600 is shown in Figure 15.

Using Stoughton's method [15], the principal strains (ϵ_1, ϵ_2) from the ϵ FLC are converted into principal stress-space (σ_1, σ_2). The x-axis of the XSFLC is the invariant mean stress (hydrostatic stress) and is calculated from the principal stresses as follows,

$$\sigma_{hyd} = \frac{\sigma_1 + \sigma_2 + \sigma_3}{3}. \quad (3.4)$$

Since the ϵ FLC was measured under plane-stress conditions, $\sigma_3 = 0$, and reduces to,

$$\sigma_{hyd} = \frac{\sigma_1 + \sigma_2}{3}. \quad (3.5)$$

The y-axis of the XSFLC is the Von-Mises effective stress, which is an invariant and calculated as follows,

$$\bar{\sigma} = \sqrt{\frac{1}{2} [(\sigma_1 - \sigma_2)^2 + (\sigma_2 - \sigma_3)^2 + (\sigma_3 - \sigma_1)^2]}. \quad (3.6)$$

Again, $\sigma_3 = 0$, and 3.6 reduces to,

$$\bar{\sigma} = \sqrt{\sigma_1^2 + \sigma_2^2 - \sigma_1\sigma_2}. \quad (3.7)$$

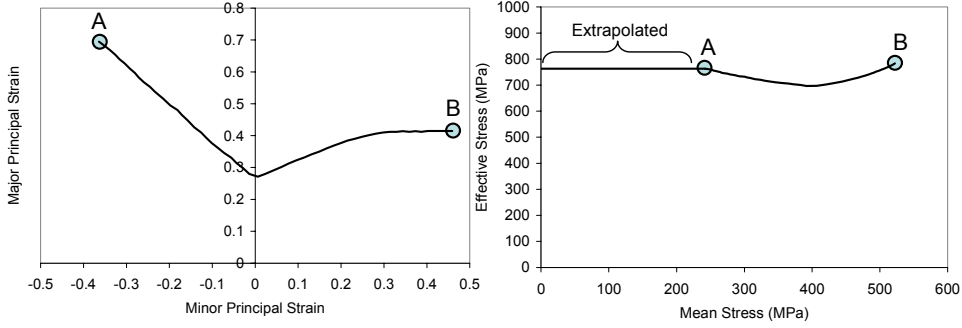
Using the above procedure, the ϵ FLC is converted into the XSFLC and is shown in Figure 15. The extrapolated region shown in Figure 15 is assumed due to the uniaxial stress point (A) of the ϵ FLC.

The following assumptions are made to transform ϵ FLC into the XSFLC,

Assumption 1: The alloys are assumed to be described by the J_2 flow theory with isotropic hardening. Hardening is described by the functional relationship $\bar{\sigma} = \bar{\sigma}(\bar{\epsilon}_p)$.

Assumption 2: The invariants: effective stress and means stress that characterize the formability limit under plane stress loading are representative of the formability limit under three-dimensional stress states.

In order to attain realistic prediction for the pre-bent hydroformed parts, two additional assumptions are required to take into account the tensile and compressive

Figure 15. : a) ϵ FLC b) XSFLC [18]

pre-strain created by the pre-bending operation.

Assumption 3: The formability of a material element that has a tensile effective tensile pre-strain at the end of bending, $\bar{\epsilon}_p$, is assumed to be $\max[\bar{\sigma}(\bar{\epsilon}_p), \bar{\sigma}_{XSFLC}]$.

Assumption 4: The formability of a material element that has a compressive effective plastic pre-strain at the end of bending, $\bar{\epsilon}_p$, is assumed to be $\max[\bar{\sigma}(2\bar{\epsilon}_p), \bar{\sigma}_{XSFLC}]$.

3.3.2. Model Implementation. As previously mentioned, LS-DYNA v970 was used to simulate the bending, springback, die close and hydroforming operations. In order to use the XSFLC to predict the onset of necking in hydroforming, a user subroutine was programmed to model the tube material. The XSFLC serves as an input to the subroutine. In addition to implementing the stress update for the element, the subroutine also tracks whether the load path ($\sigma_{hyd}, \bar{\sigma}$) for each element has crossed the XSFLC. A formability variable, γ , for a given σ_{hyd} , is defined as follows [17, 18],

$$\gamma = \frac{\bar{\sigma}}{\sigma_{XSFLC}} \quad 0 \leq \gamma \leq 1 \quad (3.8)$$

All of the simulations with exception to springback were modelled with the XSFLC subroutine. Using the post processor software LS-PREPOST, contours of γ are plotted to determine when the onset of necking has occurred. It is convenient to represent γ as binary to determine time of necking. Necking is said to occur when all five through thickness elements have crossed the XSFLC curve as shown in Figure 16.

3.3.3. Pressurization and EF Load Schedules. The hydroforming simulations for this work include a zero EF case and four different levels of load control EF. All of the hydroforming simulations were run in 13.0 msec. The first millisecond for all of the simulations was reserved for the activation of the simulated LVDT's (Figure 17).

For the zero EF case, the EF ram displacement was set to zero for the entire simulation. The internal pressure was linearly increased from zero at 1.0 msec to

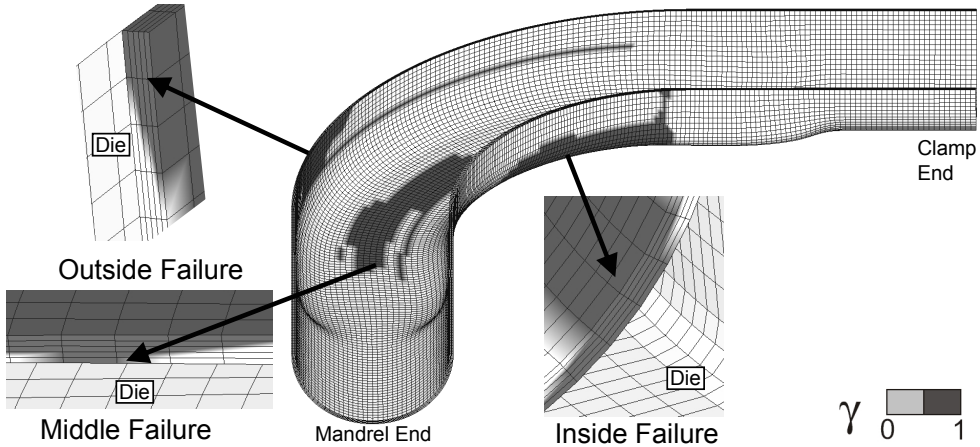


Figure 16. Failure locations during hydroforming using the XSFLC

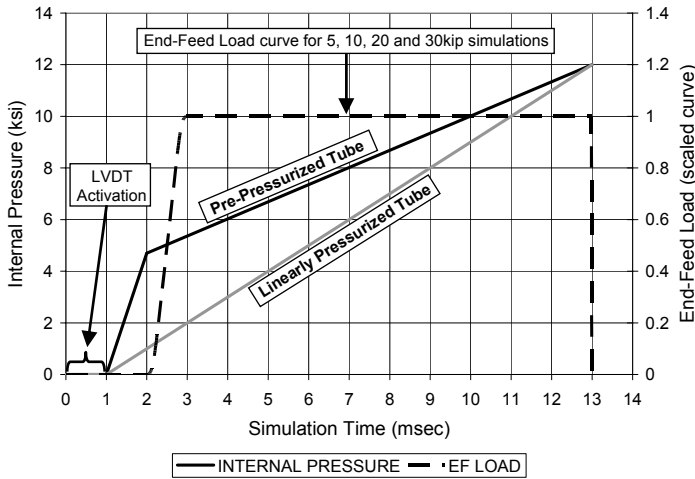


Figure 17. Pressure and end-feed schedules

12.0 ksi at 13.0 msec using the *AIRBAG_LINEAR_FLUID card in LS-DYNA [26] (Figure 17).

For the load control EF simulations, the scaled EF load curve shown in Figure 17 was used. The EF load was varied at 5, 10, 20 and 30 kip (for a full tube). The y-coordinate points of the scaled EF load curve were multiplied by the appropriate EF load scale factor for each simulation. *LOAD_RIGID_BODY [26] cards were used to apply the load in the appropriate direction of action for each ram. Full EF load was applied (ramped) from 2.0 to 3.0 msec of the simulation and remained constant until the end of the simulation. Two different pressurization schemes were used for each

different EF load case. The previously mentioned linear pressurization scheme was used with an additional pre-pressurization scheme. The pre-pressurization scheme increased the internal pressure from zero at 1.0 msec to 4.7 ksi at 2.0 msec. The pressure then increased linearly to 12.0 kip at 13.0 msec. The pre-pressurization pressure of 4.7 ksi is just below the pressure required to yield the tube. This scheme was selected to show if the effect of pre-stressing the tube would affect the formability during hydroforming.

3.4. Hydroforming Results. Using the XSFLC, three distinct failure areas were observed for every simulation. These failure locations can be seen in Figure 16. Although the inside failure location consistently occurred at the lowest internal pressure, all three regions will be discussed. Figure 18 shows the results of the hydroforming simulations.

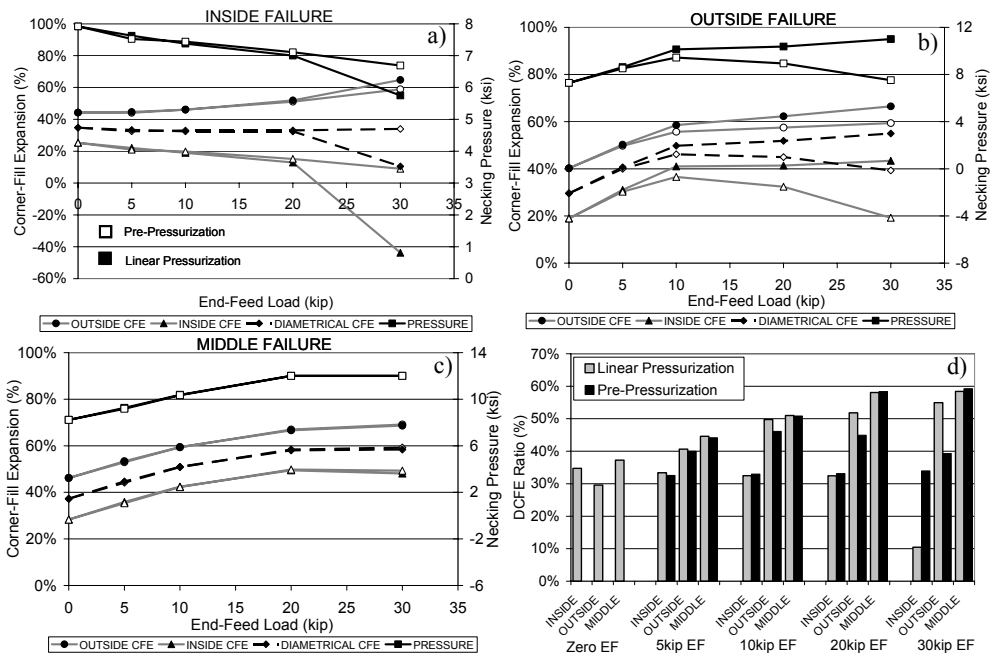


Figure 18. CFE and necking pressure results

3.4.1. Zero End-Feed Case. This EF case was tested experimentally and modelled for the work done by Simha et al. [18]. In the experiment, the tube failed at approximately 6.9 ksi in the middle failure location as shown in Figure 19.

The XSFLC predicted the first failure occurrence at the outside location when the internal pressure reached 7.3 ksi. The next failure occurred at the inside location at 7.9 ksi while the correct middle failure location was predicted at 8.3 ksi. The XSFLC overpredicted the failure pressure by 12%, which is acceptable. The additional failure

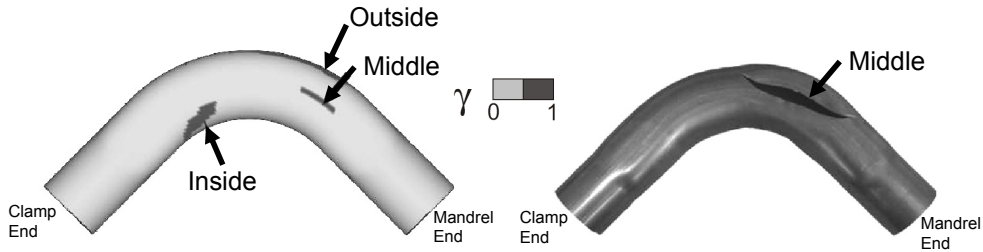


Figure 19. Numerical and experimental results for the zero EF case [18]

locations that were predicted are likely due to the approximations made for the DP600 material. These sources of error include the stress-strain curve (bulge test data is more accurate) and the approximated ϵ FLC. In [17, 18], these approximations were not made for straight and pre-bent aluminium tube and the results showed significantly more accurate predictions.

3.4.2. *End-Feed Case.* Due to the prediction of multiple failure locations, the results for the inside, outside and middle failure locations will be discussed.

Inside Failure Location

This failure location was the first to occur for all of the EF levels and both pressurization schemes. Figure 18 (a) shows an increase in outside CFE from 44% to approximately 60% for both pressurization schemes. The inside CFE has a decreasing trend from a CFE of 25% at zero EF to 9% for the pre-pressurization scheme. The negative CFE for linear pressurization was due to extreme buckling of the tube. Buckling is a result of excessive EF load, which forces the outside radius of the tube to form more than the inside radius of the tube as shown in Figure 20. In addition to the effect of EF load, the thinner outside radius region of the tube is more easily deformed than the thicker inside region of the tube. Buckling usually disappears as the internal pressure of the tube increases and forms the inside CFE region more. The effect of buckling is never entirely removed from the tube and results in the condition that outside CFE is always greater than the inside CFE for all cases and EF levels. At high levels of EF, risk of wrinkling occurs due to excessive EF force (Figure 20).

The DCFE remains constant as EF increases for both pressurization schemes (with exception to linear pressurization at 30 kip). This trend is opposite to that of the published work on the effects of EF on the hydroforming of axial members. The failure pressure also decreases from 7.9 ksi at zero EF to 5.5 ksi at 30 kip EF.

Figure 21 (a) and (b) shows the stress-path in the last element to cross the XSFLC at each failure location. The elements were on the outer layer of the tube. The paths do not begin at the origin due to the non-zero stress after springback. Figure 21 (b) indicates that failure on the inside occurred after the path surpassed the XSFLC. This is because a new hardening limit was reached in pre-bending (Assumption 4). For the path of the inside element, no contact with the die is made. Initially, the EF load is dominant in the longitudinal direction (compression), but as the internal pressure

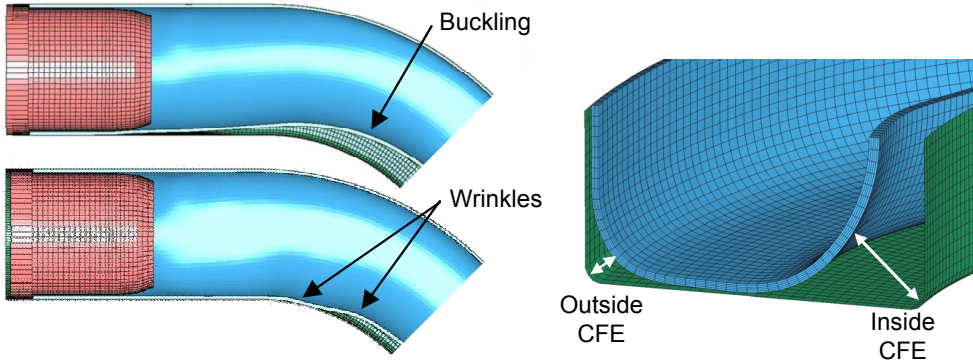
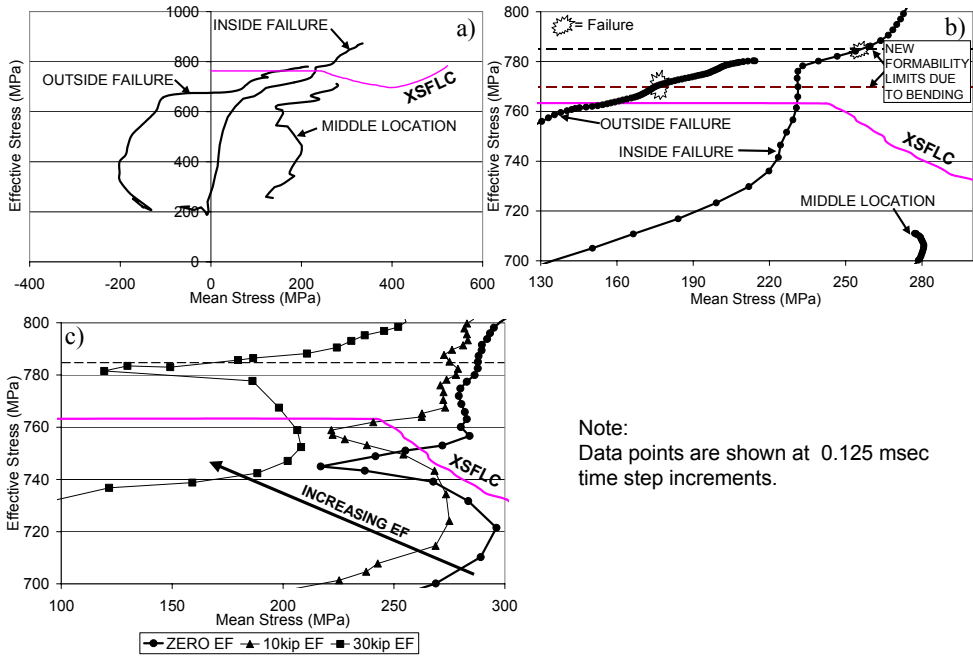


Figure 20. Numerical hydroforming models showing buckling, wrinkling and CFE

increases and friction retards the material flow longitudinally, the dominant stress becomes tensile and is in the hoop direction as the tube experiences free-expansion.



Note:
Data points are shown at 0.125 msec time step increments.

Figure 21. a) and b) Stress-paths for the three failure location elements, pre-pressurization 20 kip case, c) stress-path for inside element failure for increasing EF cases.

Figure 21 (c) is a plot of the stress-path for the inside failure location element at zero, 10 and 20 kip EF. It serves to show how increasing EF affects the stress-path of

the inside element. The trend shows a negative shift along the mean stress axis, as EF increases. This shift is due to an increasing compressive stress component (from EF) in the axial direction of the tube. The effective stress also increases with increasing EF along the effective stress axis. Because the stress-path is in the extrapolated region of the XSFLC at higher EF, the assumption of this extrapolation needs to be verified experimentally. This is also the case for the outside element failure stress-path shown in Figure 21 (a) and (b).

Outside Failure Location

This failure location was the second to occur for all of the EF levels and both pressurization schemes. For the linear pressurization scheme, Figure 19 (b) shows an increase in outside CFE from 40% to approximately 66% and 59% for the pre-pressurization scheme. The inside CFE has the expected increasing trend as well with a CFE of 19% at zero EF to 43% for the linear pressurization scheme and to 32% for pre-pressurization. The DCFE increases for the linear pressurization and decreases (after 10 kip case) for the pre-pressurization case, making the linear pressurization scheme more favourable. The failure pressure increases from 7.3 ksi at zero EF to 11.0 ksi at 30 kip EF for the linear pressurization scheme. Whereas the pressure increases and then decreases to 7.9 ksi for the pre-pressurization scheme.

The outside failure element is in contact with the die cavity at the beginning of the simulation. A dominant compressive principal stress in the longitudinal direction is due to the EF load which causes the mean stress to be negative (Figure 21). As friction between the tube and die wall increases due to the internal pressure, the material flow is impeded longitudinally and the dominant stress becomes tensile and in the hoop direction. The compressive through-thickness stress component becomes equivalent to the compressive longitudinal stress component during the simulation, but both are considerably less than the hoop stress component.

Middle Failure Location

The most promising results come from this failure location because of the experimental findings for the zero EF case. Almost no differences existed between the two pressurization schemes. It should be noted that the final prescribed internal pressure of 12.0 kip was achieved for the 20 and 30 kip EF cases. Figure 19 (c) shows that the outside CFE increases from 46% to 69% and the inside CFE increases from 28% to 48%. The DCFE also increases from 37% to 59%. There is potential for greater CFE due to the fact that necking pressure was not achieved by the 20 and 30 kip cases. The necking pressure increases from 8.2 ksi at zero EF to the maximum prescribed 12.0 ksi at 20 and 30 kip EF.

The middle failure element is in contact with the die wall at the beginning of the simulation. There is no dominant stress component for the first part of the simulation with a tensile stress in the hoop direction and smaller compressive stresses in the longitudinal and through-thickness directions. Near the end of the simulation, a dominant tensile stress occurs in the hoop direction and a smaller tensile stress forms in the longitudinal direction. A small through-thickness component is also present

near the end of the simulation and causes the stress-path to curve left as shown in the zoomed graph in Figure 21. The effective stress at this location never reaches the XSFLC and is therefore safe for the 20 kip EF case in Figure 21.

4. Conclusions

Based on the investigation into the effect of load control EF on the formability of DP600 steel tube using the XSFLC, the following conclusions can be made:

- The mandrel rotary-draw tube bending operation was successfully modelled using the material properties extracted from uniaxial tensile tests and the coefficients of friction from the twist compression test. The strain and thickness distributions were accurately predicted and validated with experimental data.
- The XSFLC was shown to closely predict the failure (necking) pressure for the zero EF case. Other failure locations were also predicted, but within a close necking pressure range, causing questions to arise about the stress-strain relationship used and the approximated ϵ FLC for the DP600.
- With the application of load control EF, the prediction of failure at the three distinct locations resulted in different trends for CFE (Figure 18 (d)). The first location to fail for all models was at the inside which resulted in no change in formability for increasing levels of EF. The outside and middle failure locations indicated the expected results of increasing formability due to increased EF. This will be verified experimentally at the University of Waterloo
- The effect of pre-pressurization showed that it prevents buckling at the highest level of EF for the inside failure location results. Linear pressurization was shown to be advantageous for the outside necking location results.
- For the inside and outside necking locations, the effect of the through-thickness compressive stress component causes a shift in the stress-space load path, proving it is important to consider in hydroforming.

5. Acknowledgements

Financial support for this research was provided by the Canadian Auto21 Network of Centres of Excellence, Dofasco, Stelco, General Motors, Eagle Precision Technologies, D.A. Stuart and Nova Tube.

References

1. SINGH, H.: *Fundamentals of Hydroforming*. Society of Manufacturing Engineers, 2003.
2. MORTIMER, J.: BMW breaks new ground with hydroforming. *Assembly Automation*, **21**(4), (2001), 317–320.
3. DYMENT, J.: *The Effects of Bending Process on the Hydroformability of Steel Tubes*. Master's thesis, University of Waterloo, 2004.
4. MORPHY, G.: Tubular hydroformability: ability and flexibility of pressure sequencing. In *Proceedings of the Tube and Pipe Association Conference on Hydroforming*, Tube and Pipe Association, 1997, pp. 199–213.

5. AHMETOGLU, M., SUTTER, K., LI, X. J., and ALTAN, T.: Tube hydroforming: current research, applications and need for training. *Journal of Materials Processing Technology*, **98**, (2000), 224–231.
6. KIM, S. and KIM, Y.: Analytical study for tube hydroforming. *Journal of Materials Processing Technology*, **128**, (2002), 232–239.
7. THIRUVARUDCHELVAN, S., SEET, G. L., and ANG, H. E.: Computer-monitored hydraulic bulging of tubes. *Journal of Materials Processing Technology*, **57**, (1996), 182–188.
8. ASANFI, N.: Analytical modelling of tube hydroforming. *Thin-Walled Structures*, **34**, (1999), 295–330.
9. DOHMANN, F. and HARTL, C.: Tube hydroforming - research and practical application. *Journal of Materials Processing Technology*, **71**, (1997), 174–186.
10. KOC, M. and ALTAN, T.: Prediction of forming limits and parameters in the tube hydroforming process. *International Journal of Machine Tools and Manufacture*, **42**, (2002), 123–138.
11. XIA, Z. C.: Failure analysis of tubular hydroforming. *Journal of Engineering Materials and Technology*, **123**, (2001), 423–429.
12. BARDELCEK, A. and WORSWICK, M. J.: Numerical investigation into the effects of bending boost and hydroforming end-feed on the hydroformability of DP600 tube. *SAE Transactions: Journal of Materials and Manufacturing*. In Press.
13. BARDELCEK, A. and WORSWICK, M. J.: The effect of element formulation on the prediction of boost effects in numerical tube bending. In *NUMISHEET 2005*, 2005, pp. 774–780.
14. KIM, J., LEI, L., HWANG, S., KANG, S., and KANG, B.: Manufacture of an automobile lower arm by hydroforming. *International Journal of Machine Tools and Manufacture*, **42**, (2002), 69–78.
15. STOUGHTON, T. B.: A general forming limit criterion for sheet metal forming. *International Journal of Mechanical Sciences*, **42**(1-27).
16. GREEN, D. and STOUGHTON, T. B.: Hydroforming severity using stress-based forming limits. In *2nd Annual North American Hydroforming Conference and Exhibition*, 2004.
17. SIMHA, C. H. M., GHOLIPOUR, J., BARDELCEK, A., and WORSWICK, M. J.: Application of an extended stress-based flow limit curve to predict necking in tubular hydroforming. In *NUMISHEET 2005*, 2005, pp. 511–516.
18. SIMHA, C. H. M., GHOLIPOUR, J., BARDELCEK, A., and WORSWICK, M. J.: The prediction of necking in tubular hydroforming using an extended stress-based forming limit curve. *Journal of Engineering Material and Technology*. Submitted MATS-05-1169.
19. DYWER, N., WORSWICK, M. J., GHOLIPOUR, J., XIA, Z. C., and KHODAYARI, G.: Pre-bending and subsequent hydroforming of tube: Simulation and experiment. In *NUMISHEET 2002*, 2002.
20. SCHEY, J. A. and NAUTIYAL, P. C.: Effects of surface roughness on friction and metal transfer in lubricated sliding of aluminium alloys against steel surfaces. *Wear*, **146**(37-51).
21. KHODAYARI, G., REID, J. V., and GARNETT, M.: Analyzing tubes, lubes, dies and friction. *Tube and Pipe Journal*, **13**, (2002), 72–74.

22. FUCHIZAWA, S. and MARAZAKI, M.: Bulge test for determining stress-strain characteristics of thin tube. In *4th International Conference on Technology of Plasticity, Advanced Technology of Plasticity*, 1993, pp. 488–493.
23. KEELER, S. P. and BACKOFEN, W. A.: Plastic instability and fracture in sheets stretched over rigid punches. *ASM Transactions Quarterly*, **56**, (1963), 25–48.
24. GOODWIN, G. M.: *Application of Strain Analysis to Sheet Metal Forming in the Press Shop*. Tech. Rep. 690093, SAE, 1968.
25. KEELER, S. P. and BRAZIER, W. G.: Relationship between laboratory material characterization and press shop formability. In *Microalloy 75*, 1977, pp. 517–530.
26. HALLQUIST, J. O.: *LS-DYNA Keyword Users Manual, Version 970*. 2003.

CALCULATING TURBULENT FLOWS BASED ON A STOCHASTIC MODEL

TIBOR CZIBERE

Department of Fluid and Heat Engineering, University of Miskolc
H-3515 Miskolc-Egyetemváros, Hungary

aramczt@uni-miskolc.hu

[Received: November 30, 2006]

Abstract. Relying on his theoretical and experimental examinations, O. Reynolds arrived at the conclusion that the Navier-Stokes equation of motion describing laminar flow continues to remain valid in terms of velocity fields interpreted by instantaneous values when the fluid is in turbulent motion. Th. von Kármán also used experimental experience to construct his similarity hypothesis [1], according to which, on the one hand, outside the viscous layer close to the wall, the turbulent velocity distribution does not depend on the viscosity of the medium, and on the other, the local (turbulent) flow patterns show mechanical similarities in points of the fully developed turbulent flow field; in other words each of them can be transferred into a common (turbulent) flow pattern by means of a suitably chosen transformation.

The turbulence model used in this paper also relies on the same hypothesis. The model's fundamental principle can be summed up in the following words: in any point of the flow field the Helmholtz-Thomson vortex theorem valid in the relative coordinate system - that is a coordinate system moving steadily at a velocity equal to the average Reynolds velocity in the given point - is suitable for describing the turbulent velocity fluctuation, thus it can be considered to be the equation of motion of turbulence, which then can be transformed, on the basis of von Kármán's similarity hypothesis, into the coordinate system of the common flow pattern mentioned. And a particular solution to the partial differential equation obtained can be used to represent the stochastic flow of the turbulence while the optional coefficients and phase constants appearing in it as integration constants are considered to be probability variables. By using the scalar components of the turbulent velocity fluctuation obtained in this way - in this special relative coordinate system - it is possible to produce the scalar elements of Reynolds' turbulent stress tensor, which can be re-transformed into the physical space on the basis of mechanical similarity. Thus, by using the stochastic turbulence model it becomes possible to produce Reynolds' turbulent stress tensor in a specific way, which in the transport equations of turbulent motion leads to formal changes that can be used in the numerical solutions with advantage.

Mathematical Subject Classification: 76F02,76F99

Keywords: Turbulent flow, moment and vortex transports, one- and two-equation models of turbulence numerical solution in pipe-flow

1. Governing equations of turbulent motion

The turbulent motion of a fluid continuum in the Eulerian approach can be described by the superposition of two velocity fields depending on place and time: one is velocity fluctuation changing rapidly and in a stochastic way in time, and the other velocity field determines the motion of the fluid continuum without fluctuations but showing changes in time. The latter can naturally be a motion constant with time, when we have to do with the steady flow of the continuum; by contrast the velocity field describing turbulent fluctuation is invariably a function of time. Each characteristic of the instantaneous state of motion (scalar, vector or tensor) can be considered to be composed of two components: instantaneous value = mean value + fluctuation. The mean value – i.e. the Reynolds time average – is an integral mean value of a given motion characteristic referring to a time interval t_0 that is relatively big compared to the period of turbulent fluctuation:

$$f(\mathbf{x}, t) = \frac{1}{t_0} \int_t^{t+t_0} f_T(\mathbf{x}, \tau) d\tau, \quad (1.1)$$

where \mathbf{x} is the vector of place, t is time; the function $f(x, t)$ may interpret a scalar, vector or tensor field; and the subscript T here refers to ‘instantaneous value’. The Reynolds time-mean of the fluctuation is naturally zero. Accordingly, the instantaneous velocity field of the fluid continuum performing the turbulent motion can be written in the form

$$\mathbf{v}_T(\mathbf{x}, t) = \mathbf{v}(\mathbf{x}, t) + \mathbf{v}'(\mathbf{x}, t), \quad (1.2)$$

where $\mathbf{v}(\mathbf{x}, t)$ is the Reynolds mean velocity field and $\mathbf{v}'(\mathbf{x}, t)$ is the velocity field of turbulent fluctuation. The curl of the velocity leads to the instantaneous vortex field, which is also the sum of two components, the Reynolds mean vortex field and the turbulent fluctuation field:

$$\boldsymbol{\Omega}_T(\mathbf{x}, t) = \nabla \times \mathbf{v}_T = \boldsymbol{\Omega}(\mathbf{x}, t) + \boldsymbol{\Omega}'(\mathbf{x}, t). \quad (1.3)$$

The surface forces (caused by molecular viscosity) arising between the fluid particles are also subject to stochastic fluctuation in the instantaneous velocity field of the turbulent flow; i.e. the instantaneous value of the tensor field expressing the stresses arising on the surface of the fluid components can be given similarly in the form

$$\mathbf{F}_T(\mathbf{x}, t) = \mathbf{F}(\mathbf{x}, t) + \mathbf{F}'(\mathbf{x}, t), \quad (1.4)$$

where tensor $\mathbf{F}(\mathbf{x}, t)$ expresses the Reynolds’ time-mean value, and tensor $\mathbf{F}'(\mathbf{x}, t)$ expresses the fluctuation caused by the turbulence; the time-mean value of the latter being also zero. With respect to the fact that pressure in a viscous fluid in motion is equal to the negative of the first scalar invariant of the stress tensor, the following relationship:

$$p_T = -\frac{1}{3}(F_{11} + F_{22} + F_{33}) - \frac{1}{3}(F'_{11} + F'_{22} + F'_{33}) = p + p',$$

where p' is turbulent pressure fluctuation, and p is thermodynamic pressure (the pressure in the thermodynamic equation of state of the medium in flow), holds for

the instantaneous value of pressure in a turbulent flow as follows from equation (1.4). Accordingly, the Reynolds time-mean of instantaneous turbulent pressure is equal to thermodynamic pressure. In our investigation we tend to suppose that the Stokes molecular viscosity law also holds for the instantaneous turbulent motion of a viscous fluid:

$$\mathbf{F}_T = -p_T \mathbf{I} + \eta \left[(\mathbf{v}_T \circ \nabla + \nabla \circ \mathbf{v}_T) - \frac{2}{3} (\nabla \cdot \mathbf{v}_T) \mathbf{I} \right], \quad (1.5)$$

where η is the dynamic viscosity factor (considered constant), and \mathbf{I} is unit tensor. Assuming that, on the one hand, the law of the conservation of mass continues to hold for the turbulent motion of the fluid continua, and that, on the other, the Navier-Stokes equation of motion gives an appropriate description of the instantaneous motion as well, in the velocity field of turbulent flow interpreted by means of instantaneous values, the equation of continuity expressing the conservation of mass can be written in the form

$$\frac{\partial \rho_T}{\partial t} + \nabla \cdot \rho_T \mathbf{v}_T = 0 \quad (1.6)$$

and the Navier-Stokes equation of motion can be given in the form

$$\rho_T \frac{\partial \mathbf{v}_T}{\partial t} + \rho_T (\mathbf{v}_T \cdot \nabla) \mathbf{v}_T = \rho_T \mathbf{g} + \text{Div } \mathbf{F}_T, \quad (1.7)$$

where \mathbf{g} is the specific value of the field force referring to a mass unit. If the medium in flow is incompressible ($\rho_T = \rho = \text{const}$), the equation of continuity takes the form $\nabla \cdot \mathbf{v}_T = 0$, from which it follows that for an incompressible medium the turbulent fluctuation is $\nabla \cdot \mathbf{v}' = 0$ also for the velocity field of $\mathbf{v}'(\mathbf{r}, t)$. Now, substituting the expression $\mathbf{v}_T = \mathbf{v} + \mathbf{v}'$ into the above equations and taking the time-mean value of each member, in the $\mathbf{v}(\mathbf{r}, t)$ Reynolds mean velocity field the equation of continuity and the equation of motion take the following forms:

$$\nabla \cdot \mathbf{v} = 0 \quad (1.8)$$

$$\rho \frac{\partial \mathbf{v}}{\partial t} + \rho (\mathbf{v} \cdot \nabla) \mathbf{v} = \rho \mathbf{g} - \nabla p + \eta \Delta \mathbf{v} + \text{Div } \mathbf{F}_R, \quad (1.9)$$

respectively, where \mathbf{F}_R is the Reynolds turbulent stress tensor:

$$\mathbf{F}_R = -\rho \overline{(\mathbf{v}' \circ \mathbf{v}')}. \quad (1.10)$$

This tensor expresses a surface force in the Reynolds equation of motion (1.9) in the same way as the viscous stress tensor does, which, however, originates not from the molecular viscosity of the fluid, but from the change of momentum due to turbulent velocity fluctuation.

It should be noted that for the laminar flow of an incompressible medium developing in a potential field of force ($\mathbf{g} = -\nabla U$; U being the potential of the field of force) the equation of motion (1.9) will take the form

$$\rho \frac{\partial \mathbf{v}}{\partial t} + \rho (\mathbf{v} \cdot \nabla) \mathbf{v} = -\rho \nabla U - \nabla p + \eta \Delta \mathbf{v} \quad (1.11)$$

of the Navier-Stokes equation of motion, which, when supplemented with the equation of continuity $\nabla \cdot \mathbf{v} = 0$, gives a system of equations (consisting of a total of four scalar differential equations) for the purpose of determining the four unknown functions

(the three components of velocity and the pressure). In the laminar case the three scalar equations of motion and the equation of continuity thus form a closed system of equations for determining the four unknown functions. In the case of turbulent flow, however, the equation of motion (1.9) – since the turbulent stress tensor \mathbf{F}_R introduces new unknowns into it – does not form a closed system with the equation of continuity (1.8) any more.

In order to develop the equation of equilibrium of internal energy, our starting point is the theorem of the conservation of energy referring to transport processes, which is written for an incompressible medium in the velocity field of turbulent flow interpreted by instantaneous values for the case without dissipation heat transfer:

$$\rho c_P \left(\frac{\partial T_T}{\partial t} + (\mathbf{v}_T \cdot \nabla) T_T \right) = \nabla \cdot (\lambda \nabla T_T) + (\boldsymbol{\sigma}_T \cdot \nabla) \cdot \mathbf{v}_T, \quad (1.12)$$

where c_P is the specific heat of the medium in flow under constant pressure, λ is its thermal conduction coefficient, and $\boldsymbol{\sigma}_T$ is the deviator of the turbulent stress tensor \mathbf{F}_T interpreted by instantaneous values, for which the Stokes formula of the form

$$\boldsymbol{\sigma}_T = \eta (\mathbf{v}_T \circ \nabla + \nabla \circ \mathbf{v}_T)$$

holds. Substituting relationship (1.2) into the above equation of the conservation of energy, and then taking the time-mean value of each member, a short calculation gives the scalar equation of the form

$$\rho c_P \left(\frac{\partial T}{\partial t} + (\mathbf{v} \cdot \nabla) T \right) = \nabla \cdot (\lambda \nabla T) - \rho c_P \nabla \cdot (\overline{\mathbf{v}' T'}) + \rho(\varphi + \epsilon), \quad (1.13)$$

where the first member on the right-hand side is an expression of molecular heat transport and the second one is that of turbulent heat transport; the third and the fourth member gives direct (viscous) dissipation and turbulent dissipation, resp.:

$$\varphi = \nu (\mathbf{v} \circ \nabla) : (\mathbf{v} \circ \nabla + \nabla \circ \mathbf{v}) \quad ; \quad \epsilon = \nu (\overline{\mathbf{v}' \circ \nabla}) : (\overline{\mathbf{v}' \circ \nabla + \nabla \circ \mathbf{v}'}), \quad (1.14)$$

where ν is the kinematic viscosity factor ($\nu = \eta/\rho$).

By way of summary of the above it can be stated that from the point of the solubility of a problem of non-isothermal turbulent flow three equations – the equation of continuity (1.8), the Reynolds equation of motion (1.9) and the energy equation (1.13) – are already available to determine the unknown velocity distribution $\mathbf{v}(\mathbf{x}, t)$, the pressure distribution $p(\mathbf{x}, t)$ and the temperature distribution $T(\mathbf{x}, t)$, but further unknown functions also appear in the equations: a) in equation (1.9) the turbulent stress tensor \mathbf{F}_R , b) in equation (1.13) the turbulent dissipation ϵ as well as the velocity-temperature correlation $\overline{\mathbf{v}' T'}$. Thus the number of unknowns is higher than the number of scalar differential equations at our disposal for solving them; i.e. the system of differential equations to be solved is underdetermined. It follows that in order to solve a given problem of turbulent flow, it is necessary to supplement the system of equations constituted by the equation of continuity, the Reynolds equation of motion and the equation of equilibrium of internal energy with further equations.

In order to develop the equation of equilibrium of the specific turbulent kinetic energy defined by equation $k = \overline{\mathbf{v}' \cdot \mathbf{v}'}/2$, the Navier-Stokes equation (1.7) of the fluid continuum moving in the velocity field $\mathbf{v}_T(\mathbf{x}, t)$ interpreted by instantaneous values

is first multiplied scalarly by the velocity vector \mathbf{v}' of turbulent fluctuation, then its time-mean value is taken, and then after ordering the following expression

$$\frac{dk}{dt} + \overline{(\mathbf{v}' \circ \mathbf{v}') : (\nabla \circ \mathbf{v})} + \overline{\mathbf{v}' \cdot \nabla \frac{\mathbf{v}' \cdot \mathbf{v}'}{2}} + \frac{1}{\rho} \overline{\mathbf{v}' \cdot \nabla p'} - \nu \overline{\mathbf{v}' \cdot \Delta \mathbf{v}'} = 0 \quad (1.15)$$

is obtained. Let us now take into account that for an incompressible fluid the following two equalities

$$\nabla \left[\overline{\mathbf{v}' \left(\frac{\mathbf{v}' \cdot \mathbf{v}'}{2} + \frac{p'}{\rho} \right)} \right] = \overline{\mathbf{v}' \cdot \nabla \frac{\mathbf{v}' \cdot \mathbf{v}'}{2}} + \frac{1}{\rho} \overline{\mathbf{v}' \cdot \nabla p'} \quad (1.16)$$

$$\Delta \frac{\mathbf{v}' \cdot \mathbf{v}'}{2} = \mathbf{v}' \cdot \Delta \mathbf{v}' + (\mathbf{v}' \circ \nabla) : (\mathbf{v}' \circ \nabla + \nabla \circ \mathbf{v}') - (\mathbf{v}' \circ \nabla) : (\nabla \circ \mathbf{v}')$$

hold. After ordering and taking the time-mean value, the latter gives the following equation

$$\overline{\mathbf{v}' \cdot \Delta \mathbf{v}'} = \Delta \frac{\overline{\mathbf{v}' \cdot \mathbf{v}'}}{2} - \overline{(\mathbf{v}' \circ \nabla) : (\mathbf{v}' \circ \nabla + \nabla \circ \mathbf{v}')} + \overline{(\mathbf{v}' \circ \nabla) : (\nabla \circ \mathbf{v}')},$$

which, multiplied by the kinematic viscosity factor ν and taking into account the definition equation (1.14) of the turbulent dissipation ϵ , results in the following:

$$\nu \overline{\mathbf{v}' \cdot \Delta \mathbf{v}'} = \nu \Delta k - \epsilon + \nu \overline{(\mathbf{v}' \circ \nabla) : (\nabla \circ \mathbf{v}')}. \quad (1.17)$$

Let us now determine first the divergence of tensor $\mathbf{v}' \circ \mathbf{v}'$:

$$\text{Div} (\mathbf{v}' \circ \mathbf{v}') = (\mathbf{v}' \circ \mathbf{v}') \cdot \nabla = (\mathbf{v}' \cdot \nabla) \mathbf{v}'$$

and then also the divergence of the vector obtained, and take the time-mean value of the latter:

$$\nabla \cdot [\text{Div} (\overline{\mathbf{v}' \circ \mathbf{v}'})] = \overline{(\mathbf{v}' \circ \nabla) : (\nabla \circ \mathbf{v}')}. \quad (1.17)$$

Using the former relations gives the following:

$$\nu \overline{\mathbf{v}' \cdot \Delta \mathbf{v}'} = \nu \nabla \cdot [\nabla k + \text{Div} (\overline{\mathbf{v}' \circ \mathbf{v}'})] - \epsilon \quad (1.17)$$

for the fifth term of equation (1.15). Substituting the relations (1.16) and (1.17) into equation (1.15) gives the equation of equilibrium of turbulent kinetic energy in the form

$$\frac{dk}{dt} + \overline{(\mathbf{v}' \circ \mathbf{v}') : (\nabla \circ \mathbf{v})} + \epsilon + \nabla \cdot \left[\overline{\mathbf{v}' \left(\frac{\mathbf{v}' \cdot \mathbf{v}'}{2} + \frac{p'}{\rho} \right)} \right] - \nu \nabla k - \nu \text{Div} (\overline{\mathbf{v}' \circ \mathbf{v}'}) = 0, \quad (1.18)$$

which can be used as the supplementary equation of the system of equations constituted by the equation of continuity (1.8), the equation of motion (1.9) and the equation of equilibrium of internal energy (1.13).

2. Vortex theorems in turbulent flow

The German H. Ertel and the Russian A. A. Friedmann [2] showed independently of each other that if in a fluid continuum moving in a given velocity field $\mathbf{v}(\mathbf{x}, t)$ there is also a second arbitrary vector field $\mathbf{a}(\mathbf{x}, t)$ given, then the necessary and sufficient condition that the vector lines determined by the equation $\mathbf{a} \times d\mathbf{x} = \mathbf{0}$ should be constituted during the complete time of the motion by the same fluid particles and that the intensity $\mathbf{a} \cdot d\mathbf{A} = a dA_n$ of the elementary vector tubes constituted by the vector lines should remain unchanged is that the vector function $\mathbf{a}(\mathbf{x}, t)$ should satisfy the requirement of the following equation:

$$\frac{\partial \mathbf{a}}{\partial t} + (\mathbf{v} \cdot \nabla) \mathbf{a} - (\mathbf{a} \cdot \nabla) \mathbf{v} + \mathbf{a} (\nabla \cdot \mathbf{v}) = \mathbf{0}. \quad (2.1)$$

After ordering and taking the rotations of all the members of the equation of motion (1.7) of the motion of the fluid developing in the turbulent velocity field $\mathbf{v}_T(\mathbf{x}, t)$ interpreted by instantaneous values, in case of a potential force field gives the equation of the form

$$\frac{\partial \boldsymbol{\Omega}_T}{\partial t} + (\mathbf{v}_T \cdot \nabla) \boldsymbol{\Omega}_T - (\boldsymbol{\Omega}_T \cdot \nabla) \mathbf{v}_T + \boldsymbol{\Omega}_T (\nabla \cdot \mathbf{v}_T) = \nu \Delta \boldsymbol{\Omega}_T, \quad (2.2)$$

which is nothing else but the Helmholtz-Thomson vortex theorem referring to the turbulent vortex field $\boldsymbol{\Omega}_T(\mathbf{x}, t)$ interpreted by instantaneous values. In line with the Ertel-Friedmann theorem of vector-line conservation (2.1), thus in case of the turbulent flow of a compressible barotrope medium in a potential force field the instantaneous vortex lines determined by the equation $\boldsymbol{\Omega}_T \times d\mathbf{x} = \mathbf{0}$ do not remain unchanged, but are diffused into the surroundings, however, they remain unchanged, while ν tends to 0.

The vortex theorem concerning the velocity field $\mathbf{v}(\mathbf{x}, t)$ interpreted by turbulent mean values is obtained from the vortex theorem (2.2) concerning the velocity field $\mathbf{v}_T(\mathbf{x}, t)$ interpreted by instantaneous values by substituting $\boldsymbol{\Omega}_T = \boldsymbol{\Omega} + \boldsymbol{\Omega}'$ and taking the time-mean values:

$$\frac{\partial \boldsymbol{\Omega}}{\partial t} + (\mathbf{v} \cdot \nabla) \boldsymbol{\Omega} - (\boldsymbol{\Omega} \cdot \nabla) \mathbf{v} + \boldsymbol{\Omega} (\nabla \cdot \mathbf{v}) = \nu \Delta \boldsymbol{\Omega} + \nabla \times \overline{(\mathbf{v}' \times \boldsymbol{\Omega}')}. \quad (2.3)$$

Comparing this now with Ertel-Friedmann's theorem of conservation (2.1), it can be stated that in the velocity field interpreted by the turbulent mean velocity the vortex lines determined by the differential equation $\boldsymbol{\Omega} \times d\mathbf{x} = \mathbf{0}$ do not remain unchanged with the limit of ν tending to 0, but become diffused in the surroundings during the motion. The extent of vortex diffusion is determined by the expression on the right-hand side of equation (2.3): the first member is the viscosity of the medium in flow and the second one expresses the extent of vortex diffusion caused by turbulent exchange of momentum.

The vortex theorem regarding the velocity field of turbulent fluctuation $\mathbf{v}'(\mathbf{x}, t)$ is obtained by the following train of thought. Let us consider the turbulent motion of a compressible barotrope fluid continuum in the surroundings of an arbitrarily fixed point P in the field. Let the turbulent mean velocity in the point be \mathbf{v}_P and the vortex vector $\boldsymbol{\Omega}_P = \nabla \times \mathbf{v}_P$. In the surroundings of the fixed point P in an arbitrary

running point Q

$$\mathbf{v}_T = \mathbf{v}_Q + \mathbf{v}' \quad ; \quad \boldsymbol{\Omega}_T = \nabla \times \mathbf{v}_T = \boldsymbol{\Omega}_Q + \boldsymbol{\Omega}' \quad (2.4)$$

are the turbulent instantaneous values. Since the extent of change in the time-mean velocity is by several orders smaller than that of turbulent fluctuation, the general validity is not restricted if – in the examination of the velocity field of turbulent fluctuation – the turbulent mean velocity field is considered to be steady (stationary) and thus velocity \mathbf{v}_P and the vortex vector $\boldsymbol{\Omega}_P$ are regarded as constant. The vortex theorem (2.2) concerning the instantaneous turbulent velocity field is evidently valid also when seen from the relative coordinate system, whose origin performs a steady motion at the same speed as velocity \mathbf{v}_P dominant in point P . In other words, it is possible to write the vortex theorem of the form

$$\frac{\partial \boldsymbol{\Omega}_T}{\partial t} + [(\mathbf{v}_T - \mathbf{v}_P) \cdot \nabla] \boldsymbol{\Omega}_T - (\boldsymbol{\Omega}_T \cdot \nabla) (\mathbf{v}_T - \mathbf{v}_P) + \boldsymbol{\Omega}_T [\nabla \cdot (\mathbf{v}_T - \mathbf{v}_P)] = \nu \Delta \boldsymbol{\Omega}_T$$

for the vortex field $\boldsymbol{\Omega}_T$ in the relative velocity field $\mathbf{v}_T - \mathbf{v}_P$. Let us now substitute the relationships (2.4) into this equation and then take boundary transition $Q \rightarrow P$ together with $\mathbf{v}_Q \rightarrow \mathbf{v}_P$ and $\boldsymbol{\Omega}_Q \rightarrow \boldsymbol{\Omega}_P$:

$$\begin{aligned} \frac{\partial}{\partial t} (\boldsymbol{\Omega}_P + \boldsymbol{\Omega}') + (\mathbf{v}' \cdot \nabla) (\boldsymbol{\Omega}_P + \boldsymbol{\Omega}') - [(\boldsymbol{\Omega}_P + \boldsymbol{\Omega}') \cdot \nabla] \mathbf{v}' + \\ + (\boldsymbol{\Omega}_P + \boldsymbol{\Omega}') \nabla \cdot \mathbf{v}' = \nu \Delta (\boldsymbol{\Omega}_P + \boldsymbol{\Omega}') . \end{aligned}$$

However, the vortex vector $\boldsymbol{\Omega}_P$ is constant in this equation, and therefore its derivatives (both according to time and to place) disappear. And since it can no longer lead to misunderstandings, subscript P can also be omitted from the vortex vector, and thus the former equation gives the vortex theorem of the form

$$\frac{\partial \boldsymbol{\Omega}'}{\partial t} + (\mathbf{v}' \cdot \nabla) \boldsymbol{\Omega}' - (\boldsymbol{\Omega}' \cdot \nabla) \mathbf{v}' + \boldsymbol{\Omega}' (\nabla \cdot \mathbf{v}') = (\boldsymbol{\Omega} \cdot \nabla) \mathbf{v}' - \boldsymbol{\Omega} (\nabla \cdot \mathbf{v}') + \nu \Delta \boldsymbol{\Omega}' \quad (2.5)$$

in the velocity field $\mathbf{v}'(\mathbf{x}, t)$ of turbulent fluctuation. Accordingly, the vortex lines determined by the equation $\boldsymbol{\Omega}' \times d\mathbf{x} = \mathbf{0}$ in the velocity field of turbulent fluctuation do not remain unchanged in the case $\nu \rightarrow 0$ either, but get diffused during the motion into the surroundings. With respect to the fact that, the higher Reynolds number the flow has (the better developed the turbulence is), the easier it is to neglect the intensity of viscous vortex diffusion as compared to that of turbulent vortex diffusion, the third term on the right-hand side of the above vortex theorem can be neglected, and the equation

$$\frac{\partial \boldsymbol{\Omega}'}{\partial t} + (\mathbf{v}' \cdot \nabla) \boldsymbol{\Omega}' - (\boldsymbol{\Omega}' \cdot \nabla) \mathbf{v}' + \boldsymbol{\Omega}' (\nabla \cdot \mathbf{v}') = (\boldsymbol{\Omega} \cdot \nabla) \mathbf{v}' - \boldsymbol{\Omega} (\nabla \cdot \mathbf{v}') \quad (2.6)$$

thus obtained can be considered to be the equation of motion of turbulent fluctuation arising in the vicinity of an arbitrary point P of the flow, which equation describes the instantaneous motion of a compressible barotropic fluid continuum in a relative coordinate system with the same velocity as the Reynolds mean velocity.

3. Stochastic turbulence model

The turbulent motion pattern arising in an arbitrary point of the flow field is examined in a suitably chosen special relative coordinate system that moves steadily at the same velocity as the Reynolds mean velocity in the given point and following von Kármán's [1] similarity hypothesis, it is assumed that, on the one hand, the turbulent motion patterns in all the points of the field are mechanically similar to each other, therefore all of them can be transformed into a common motion pattern, and, on the other hand, the viscosity of the medium filling the field of this common motion pattern is zero. Solving the equation of motion (2.6) of turbulent fluctuation in the relative coordinate system of the common motion pattern results in the scalar components of the velocity fluctuation, and they can be used to determine the scalar components of the Reynolds turbulent stress tensor, which, in line with the similarity hypothesis, are also components of the common motion pattern.

In flows surrounded by solid walls the velocity vector \mathbf{v} and the vortex vector $\mathbf{\Omega} = \nabla \times \mathbf{v}$ are not parallel vectors, and thus in these flows it is not always possible to interpret a special curvilinear orthogonal coordinate system, in which one set of coordinate lines is formed by the vortex lines (therefore one base vector is parallel to the vortex vector), i.e. in an arbitrary fixed point one coordinate surface will always be perpendicular to the vortex vector. If in this point the tangent plane of the other coordinate surface is given by the surface formed by the velocity vector \mathbf{v} and the vortex vector $\mathbf{\Omega} = \nabla \times \mathbf{v}$, then the normal of the third coordinate surface is necessarily parallel to the vector $\mathbf{v} \times (\nabla \times \mathbf{v})$, and the base vectors of the given special curvilinear orthogonal coordinate system (Figure 1) will be as follows:

$$\mathbf{e}'_3 = -\frac{\mathbf{\Omega}}{\Omega} ; \quad ; \quad \mathbf{e}'_2 = \frac{\mathbf{v} \times \mathbf{\Omega}}{|\mathbf{v} \times \mathbf{\Omega}|} = \frac{1}{\sqrt{1-S^2}} \left(\frac{\mathbf{v}}{v} \times \frac{\mathbf{\Omega}}{\Omega} \right)$$

$$\mathbf{e}'_1 = \mathbf{e}'_2 \times \mathbf{e}'_3 = \frac{1}{\sqrt{1-S^2}} \left(\frac{v}{v} - S \frac{\mathbf{\Omega}}{\Omega} \right) \quad ; \quad v = |\mathbf{v}| \quad ; \quad \Omega = |\mathbf{\Omega}| \quad ; \quad S = \frac{\mathbf{e}}{v} \cdot \frac{\mathbf{\Omega}}{\Omega} .$$

This special coordinate system will be the natural coordinate system in what follows. The transformation between the calculation coordinate system determined by the base vectors $\mathbf{e}_1, \mathbf{e}_2, \mathbf{e}_3$ and the previous natural coordinate system based on $\mathbf{e}'_1, \mathbf{e}'_2, \mathbf{e}'_3$ can be performed by means of the tensor (and its transposed) given by the following dyadic product sums of the base vectors:

$$\mathbf{E} = \mathbf{e}'_1 \circ \mathbf{e}_1 + \mathbf{e}'_2 \circ \mathbf{e}_2 + \mathbf{e}'_3 \circ \mathbf{e}_3 ; \quad ; \quad \mathbf{E}^T = \mathbf{e}_1 \circ \mathbf{e}'_1 + \mathbf{e}_2 \circ \mathbf{e}'_2 + \mathbf{e}_3 \circ \mathbf{e}'_3 .$$

The transformation of vector and tensor fields from the natural coordinate system x'_1, x'_2, x'_3 into the calculation coordinate system x_1, x_2, x_3 is:

$$\mathbf{a}(x_1, x_2, x_3) = \mathbf{E} \cdot \mathbf{a}(x'_1, x'_2, x'_3) \quad (3.1)$$

$$\mathbf{A}(x_1, x_2, x_3) = \mathbf{E} \cdot \mathbf{A}(x'_1, x'_2, x'_3) \cdot \mathbf{E}^T . \quad (3.2)$$

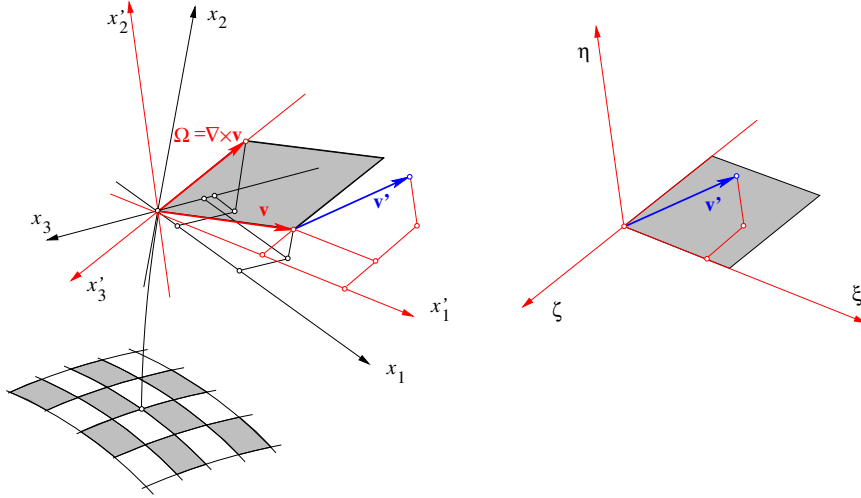


Figure 1. The three coordinate systems interpreted in an arbitrary point of the flow: the calculation coordinate system x_1, x_2, x_3 , the natural coordinate system x'_1, x'_2, x'_3 and the relative coordinate system ξ, η, ζ with steady motion at a velocity equalling v .

Turbulent fluctuation is investigated separately from the turbulent main motion arising in the Reynolds mean-velocity field $\mathbf{v}(\mathbf{x}, t)$ in the relative coordinate system, which moves steadily at a velocity equalling the Reynolds mean velocity valid in the given point and whose axis is parallel to that of the natural coordinate system (Figure 1) and whose base vectors are the same as those of the natural coordinate system. In this relative coordinate system the differential operators ∇ and $\boldsymbol{\Omega} \cdot \nabla$ are as follows:

$$\nabla = \frac{\mathbf{e}'_1}{H'_1} \frac{\partial}{\partial x'_1} + \frac{\mathbf{e}'_2}{H'_2} \frac{\partial}{\partial x'_2} + \frac{\mathbf{e}'_3}{H'_3} \frac{\partial}{\partial x'_3} \quad ; \quad \boldsymbol{\Omega} \cdot \nabla = -\boldsymbol{\Omega}(\mathbf{e}'_3 \cdot \nabla) = -\frac{\boldsymbol{\Omega}}{H'_3} \frac{\partial}{\partial x'_3},$$

where H'_i ($i = 1, 2, 3$) means the Lamé metric coefficients of the relative coordinate system x'_1, x'_2, x'_3 , which are identical with the metric coefficients of the natural coordinate system. Next – also with respect to the relationship $\boldsymbol{\Omega}' = \nabla \times \mathbf{v}'$ – the equation of motion of turbulent fluctuation is obtained from equation (2.6) – assuming an incompressible medium – in the given relative coordinate system in the following form:

$$\frac{\partial (\nabla \times \mathbf{v}')}{\partial t} + (\mathbf{v}' \cdot \nabla)(\nabla \times \mathbf{v}') - [(\nabla \times \mathbf{v}') \cdot \nabla] \mathbf{v}' = -\frac{\boldsymbol{\Omega}}{H'_3} \frac{\partial \mathbf{v}'}{\partial x'_3}. \quad (3.3)$$

According to hydro-mechanic evidence, we can talk about the similarity of two motion processes if their equations of motion can be transformed into each other by means of suitably chosen (geometric and dynamic) transformations. This requires that there exist accurately determined relationships between the scales (the conversion factors of the geometric and physical quantities in the equation of motion) used in the transformation, which will then create the necessary conditions of similarity. For the curvilinear orthogonal coordinates of place of the relative coordinate system

x'_1, x'_2, x'_3 the geometric transformations

$$H'_1 dx'_1 = M_L d\xi \quad ; \quad H'_2 dx'_2 = M_L d\eta \quad ; \quad H'_3 dx'_3 = M_L d\zeta \quad (3.4)$$

are introduced with the length scale M_L , which will transform the physical space of the velocity fluctuation into the points of the space described by the orthogonal coordinates ξ, η, ζ so that the point of origin $O(0, 0, 0)$ of the coordinate system ξ, η, ζ should correspond to the fixed point P (Figure 1). The corresponding base vectors of the two coordinate systems are identical with the base vectors of the natural coordinate system. Let us also introduce the physical transformations

$$dt = M_T d\tau \quad \text{and} \quad \mathbf{v}'(x'_1, x'_2, x'_3, t) = M_V \mathbf{w}'(\xi, \eta, \zeta, \tau) \quad (3.5)$$

for the time coordinate and the velocity fluctuation, respectively, where M_T is the time scale and M_V is the transformation scale of turbulent velocity fluctuation. This transformation maps the turbulent motion of the fluid continuum investigated arising in the vicinity of an arbitrary point P of the physical space onto the motion of a fluid model with zero viscosity filling an orthogonal coordinate system ξ, η, ζ , and thus this coordinate system can be called the pattern space of the turbulence.

The turbulent motion patterns arising in the different points of the flow space can naturally only be considered to be mechanically similar to each other if from the equation of motion (3.3) of the turbulent fluctuation the given transformation can produce a differential equation for the dimensionless velocity fluctuation $\mathbf{w}'(\xi, \eta, \zeta, \tau)$, which does not depend on the characteristics of the motion in point P . After performing the transformation described in detail above, the differential equation (3.3) assumes the following form:

$$\frac{M_V}{M_T M_L} \frac{\partial (\nabla \times \mathbf{w}')}{\partial \tau} + \frac{M_V^2}{M_L^2} [(\mathbf{w}' \cdot \nabla)(\nabla \times \mathbf{w}') - [(\nabla \times \mathbf{w}') \cdot \nabla] \mathbf{w}'] = -\frac{\Omega M_V}{M_L} \frac{\partial \mathbf{w}'}{\partial \zeta},$$

and this for the condition of mechanical similarity being searched for – i.e. the differential equation obtained for \mathbf{w}' should not be dependent on the characteristics of motion in point P evidently results in the following equality between the ‘constants’ in the equation holding:

$$\frac{M_V}{M_T M_L} = \frac{M_V^2}{M_L^2} = \frac{\Omega M_V}{M_L}. \quad (3.6)$$

Namely now the former differential equation determining the vector function $\mathbf{w}'(\xi, \eta, \zeta, \tau)$ assumes the form

$$\frac{\partial (\nabla \times \mathbf{w}')}{\partial \tau} + (\mathbf{w}' \cdot \nabla)(\nabla \times \mathbf{w}') - ((\nabla \times \mathbf{w}') \cdot \nabla) \mathbf{w}' = -\frac{\partial \mathbf{w}'}{\partial \zeta}, \quad (3.7)$$

which is in fact independent of the characteristics of motion in point P . However, according to the above, point P can be arbitrarily chosen, i.e. it may be any point in the turbulent flow space, consequently in every point of the flow space under examination the same dimensionless velocity fluctuation $\mathbf{w}'(\xi, \eta, \zeta, \tau)$ can be attached to the turbulent velocity fluctuation in the relative coordinate system ξ, η, ζ (the pattern space of the turbulence); and this at the same time expresses the mechanical similarity of turbulent velocity fluctuations and of the three-dimensional turbulence phenomenon itself as well.

The equality (3.6) between the conversion scales M_L , M_T and M_V contains two independent relationships. This means that one of the three scales can be chosen at will and that the development of the other two depends on this choice. Let e.g. the scale to be chosen at will be the length scale: $M_L = l$, then the others will take the forms, resp.:

$$M_T = 1/\Omega \quad ; \quad M_V = l\Omega . \quad (3.8)$$

The free choice of the length scale naturally only means here that its size l is indifferent in terms of the existence of mechanical similarity and that it is determined by other physical conditions.

In order to set up the turbulence model representing the internal mechanism of turbulent fluctuation, a particular solution of the differential equation (3.7) is to be found. The vector potential $\Psi(\xi, \eta, \zeta, \tau)$ can be attached to the fluctuation velocity field, from which it is possible to derive the velocity field $\mathbf{w}'(\xi, \eta, \zeta, \tau)$ by forming the rotation: $\mathbf{w}' = \nabla \times \Psi$. It is easy to understand that the vector $\nabla \times \mathbf{w}'$ can be written by using the three vectors Ψ , $\mathbf{w}' = \nabla \times \Psi$ and $\mathbf{u} = \Psi \times (\nabla \times \Psi)$ as follows:

$$\nabla \times \mathbf{w}' = a\Psi + b(\nabla \times \Psi) + c\Psi \times (\nabla \times \Psi) ,$$

where a , b , c are scalar values. The vector $\nabla \times \mathbf{w}'$ thus broken down is substituted now into the differential equation (3.7), which gives the following:

$$a \left\{ \frac{\partial \Psi}{\partial \tau} + (\mathbf{w}' \cdot \nabla)\Psi - (\Psi \cdot \nabla)\mathbf{w}' \right\} + b \frac{\partial \mathbf{w}'}{\partial \tau} + c \left\{ \frac{\partial \mathbf{u}}{\partial \tau} + (\mathbf{w}' \cdot \nabla)\mathbf{u} - (\mathbf{u} \cdot \nabla)\mathbf{w}' \right\} = -\frac{\partial \mathbf{w}'}{\partial \zeta} .$$

However, the vector potential Ψ can also be chosen so that on the one hand $\nabla \cdot \Psi = 0$, i.e. it is sourceless, and, on the other, its vector lines determined by the equation $\Psi \times d\mathbf{x} = \mathbf{0}$ should remain unchanged in the viscosity-free fluid model filling the system ξ, η, ζ ; and then in accordance with the Ertel-Friedmann conservation theorem (2.1), the two expressions in the figure bracket will disappear in the above equation. Finally, by introducing the term $\omega = -1/b$, the differential equation (3.7) to be solved assumes the following form:

$$\frac{\partial \mathbf{w}'}{\partial \tau} - \omega \frac{\partial \mathbf{w}'}{\partial \zeta} = 0 . \quad (3.9)$$

In order to solve this homogeneous first-order partial differential equation, the new independent variables $u = \zeta + \omega\tau$ and $z = \zeta$ are now introduced and then considering the identity $\mathbf{w}'(\xi, \eta, \zeta, \tau) \equiv \mathbf{w}'[\zeta(u, z), \tau(u, z); \xi, \eta]$ it is transformed for the coordinate planes u, z :

$$\frac{\partial \mathbf{w}'}{\partial z} = 0$$

The solution of this differential equation is the optional vector function of the form $\mathbf{w}'(u, \xi, \eta)$, which can be written by reversing the transformation in the following form:

$$\mathbf{w}'(\xi, \eta, \zeta, \tau) = \mathbf{w}'(\xi, \eta, \zeta + \omega\tau) .$$

Accordingly, the dimensionless velocity fluctuation \mathbf{w}' can be described by an arbitrary vector function that has the following independent variables: ξ , η , and $\zeta + \omega\tau$.

Since the differential equation (3.9) to be solved is linear, its solution can also be given in the form of the following sum:

$$\mathbf{w}'(\xi, \eta, \zeta, \tau) = c \sum_{n=1}^N \begin{pmatrix} A_{1n}(\xi, \eta) \cos [n(\zeta + \omega\tau) + \alpha_{1n}] \\ A_{2n}(\xi, \eta) \cos [n(\zeta + \omega\tau) + \alpha_{2n}] \\ A_{3n}(\xi, \eta) \cos [n(\zeta + \omega\tau) + \alpha_{3n}] \end{pmatrix} - c \sum_{n=1}^N \begin{pmatrix} A_{2n}(\xi, \eta) \sin [n(\zeta + \omega\tau) + \alpha_{2n}] \\ A_{3n}(\xi, \eta) \sin [n(\zeta + \omega\tau) + \alpha_{3n}] \\ A_{1n}(\xi, \eta) \sin [n(\zeta + \omega\tau) + \alpha_{1n}] \end{pmatrix}, \quad (3.10)$$

where c , ω , and α_{in} ($i = 1, 2, 3$) are constants, and $A_{in}(\xi, \eta)$ ($i = 1, 2, 3$) are scalar functions, which, in line with the above, are to be chosen while satisfying the condition $\nabla \cdot \mathbf{w}' = 0$. The phase angles $\alpha_{1n}, \alpha_{2n}, \alpha_{3n}$ are considered to be the three components of the three spatial dimensions, respectively, (and may be termed spatial phase angles), so the following relationship

$$\cos^2 \alpha_{1n} + \cos^2 \alpha_{2n} + \cos^2 \alpha_{3n} = 1 \quad (3.11)$$

has to hold between them. The physical meaning of the constant ω is: it is the smallest of the angular frequencies of the wave components of turbulent fluctuation. In order to determine the functions $A_{in}(\xi, \eta)$, substituting the vector function (3.10) into the equation of condition $\nabla \cdot \mathbf{w}' = 0$ gives after a short calculation the following:

$$A_{1n}(\xi, \eta) = C_{1n}(\eta)e^{n\xi} \quad ; \quad A_{2n}(\xi, \eta) = C_{2n} \quad ; \quad A_{3n}(\xi, \eta) = C_{3n}(\xi)e^{-n\eta},$$

where C_{2n} is constant, and $C_{1n}(\eta)$ and $C_{3n}(\xi)$ are arbitrary functions (may also be constants). However, the origin $O(0, 0, 0)$ of the coordinate system ξ, η, ζ belongs to an arbitrary point of the physical space, where the dimensionless velocity vector of turbulent fluctuation can be given as

$$\mathbf{w}'(0, 0, 0, \tau) = c\mathbf{u}'_0(\tau),$$

where

$$\mathbf{u}'_0(\tau) = c \sum_{n=1}^N \begin{pmatrix} C_{1n} \cos(n\omega\tau + \alpha_{1n}) - C_{2n} \sin(n\omega\tau + \alpha_{2n}) \\ C_{2n} \cos(n\omega\tau + \alpha_{2n}) - C_{3n} \sin(n\omega\tau + \alpha_{3n}) \\ C_{3n} \cos(n\omega\tau + \alpha_{3n}) - C_{1n} \sin(n\omega\tau + \alpha_{1n}) \end{pmatrix}. \quad (3.12)$$

When the dimensionless velocity fluctuation \mathbf{w}' is known, the physical transformation (3.5) can be used to determine in the natural coordinate system x'_1, x'_2, x'_3 the velocity fluctuation:

$$\mathbf{v}'(x'_1, x'_2, x'_3, t) = M_V \mathbf{w}'(0, 0, 0, \tau) = c l \Omega \mathbf{u}'_0(\tau). \quad (3.13)$$

Since the vector function $\mathbf{u}'_0(\tau)$ is dedicated to describing the stochastic process of turbulent fluctuation, in the following the coefficients C_{in} will be considered to be random amplitudes and the values α_{in} to be random phase angles ($i = 1, 2, 3$). One way of producing the coefficients C_{in} may be:

$$C_{in} = k_{in} \exp [-(n/K)^2],$$

where k_{in} are probability variables with even distribution in given intervals $[0, \delta_i]$, $|\delta_i| \leq 1$ and $K \gg 1$. The phase angles α_{in} ($i = 1, 2, 3$) are also probability variables with even distribution, among which, however, the relationship (3.11) holds, therefore

only two of the three values can be chosen at will; so finally there appear five independent probability variables in each element of the function series (3.12). Therefore it can be stated that our stochastic turbulence model handles the scalar components of the dimensionless velocity fluctuation as the series sum of cosine waves with random phase and random amplitude.

When formula (3.13) of the turbulent velocity fluctuation \mathbf{v}' is known, equation (1.10) can be used to determine the Reynolds turbulent stress tensor \mathbf{F}_R in the natural coordinate system x'_1, x'_2, x'_3 :

$$\mathbf{F}_R(x'_1, x'_2, x'_3, t) = -\rho(\overline{\mathbf{v}' \circ \mathbf{v}'}) = -\rho (l\Omega)^2 c^2 (\overline{\mathbf{u}'_0 \circ \mathbf{u}'_0}) .$$

If now the notations

$$\begin{aligned} \alpha &= \overline{u'_{0\xi}{}^2 / u'_{0\xi} u'_{0\eta}} & ; & \quad \beta = \overline{u'_{0\eta}{}^2 / u'_{0\xi} u'_{0\eta}} & ; & \quad \gamma = \overline{u'_{0\xi}{}^2 / u'_{0\xi} u'_{0\eta}} \\ \mu &= \overline{u'_{0\xi} u'_{0\xi} / u'_{0\xi} u'_{0\eta}} & ; & \quad \vartheta = \overline{u'_{0\eta} u'_{0\xi} / u'_{0\xi} u'_{0\eta}} & ; & \quad \kappa^2 = -c^2 \overline{u'_{0\xi} u'_{0\eta}} \end{aligned}$$

and the similarity tensor formed by using them

$$\mathbf{H} = \begin{pmatrix} \alpha & 1 & \mu \\ 1 & \beta & \vartheta \\ \mu & \vartheta & \gamma \end{pmatrix} \quad (3.14)$$

as well as the dominant turbulent shear stress

$$\Theta(x'_1, x'_2, x'_3, t) = \rho (\kappa l \Omega)^2 \quad (3.15)$$

are introduced, then the former formula of the turbulent stress tensor \mathbf{F}_R can be written in the following form:

$$\mathbf{F}_R(x'_1, x'_2, x'_3, t) = \Theta(x'_1, x'_2, x'_3, t) \mathbf{H} . \quad (3.16)$$

κ is a constant known in the literature as the Kármán-constant: $\kappa = 0.407$ (the free parameter c appearing in the formula (3.10) of the dimensionless velocity fluctuation serves to adjust it accurately). On the basis of the relationships (3.14) and (3.16) it can be realised that the physical meaning of the always positive Θ is: shear stress in the natural coordinate system.

Next, regarding turbulent temperature fluctuation also as the series sum of cosine waves with random phase and random amplitude, and similarly to the formulas (3.10)-(3.12) of the scalar components of dimensionless velocity fluctuation, the dimensionless temperature fluctuation

$$h'(\tau) = \hat{c} h'_0(\tau) = \hat{c} \sum_{n=1}^N \left[\hat{C}_{1n} \cos(n\omega\tau + \hat{\alpha}_{1n}) - \hat{C}_{2n} \sin(n\omega\tau + \hat{\alpha}_{2n}) \right] \quad (3.17)$$

is introduced where ω is identical with the value appearing in the formulas of dimensionless velocity fluctuation (thus the angular frequencies of the fluctuation will be identical in the velocity and temperature fields). The coefficients \hat{C}_{1n} , \hat{C}_{2n} and the phase angles $\hat{\alpha}_{1n}$, $\hat{\alpha}_{2n}$ are probability variables with even distribution, and thus among the latter the relationship

$$\cos^2 \hat{\alpha}_{1n} + \cos^2 \hat{\alpha}_{2n} = 1 \quad (3.18)$$

holds (therefore the phase angles $\hat{\alpha}_{1n}$, $\hat{\alpha}_{2n}$ determine a planar direction). In a non-isotherm turbulent flow it may be assumed that the larger the inhomogeneity of the temperature field interpreted with the mean values is, the larger the turbulent temperature fluctuation may be; in other words, the temperature fluctuation T' is proportional with the absolute value of the gradient of the temperature field T interpreted in terms of mean values. On the basis of this, and similarly to the velocity fluctuation, the temperature fluctuation in the natural coordinate system x'_1, x'_2, x'_3 can be written in the form

$$T'(x'_1, x'_2, x'_3, t) = l(x'_1, x'_2, x'_3) |\nabla T(x'_1, x'_2, x'_3, t)| h'(\tau)$$

and thus the following

$$\overline{\mathbf{v}'T'} = l^2 \Omega \overline{|\nabla T| \overline{w'(0, 0, 0, \tau)} h'(\tau)} = l^2 \Omega \overline{|\nabla T| c \hat{c} \overline{u'_0(\tau)} h'_0(\tau)}$$

is obtained for the mean value according to time $\overline{\mathbf{v}'T'}$ – i.e. the velocity-temperature correlation – in the natural coordinate system. Now the notations

$$\kappa \hat{\kappa} = -c \hat{c} \overline{u'_{0\eta} h'_0} \quad ; \quad \delta = \overline{u'_{0\xi} h'_0 / u'_{0\eta} h'_0} \quad ; \quad \chi = \overline{u'_{0\zeta} h'_0 / u'_{0\eta} h'_0}$$

are introduced, where the free parameter \hat{c} is used for the adjustment of the universal constant $\hat{\kappa} = 0.47$, the role of which in the turbulent boundary layers is similar to that of the Kármán-constant κ [3]. The direction vector

$$\hat{\mathbf{q}}(x'_1, x'_2, x'_3) = \delta \mathbf{e}'_1 + \mathbf{e}'_2 + \chi \mathbf{e}'_3 \quad (3.19)$$

of the specific turbulent heat flux density is interpreted in the natural coordinate system x'_1, x'_2, x'_3 , and it can be used to write the velocity-temperature correlation $\overline{\mathbf{v}'T'}$ in the form

$$\overline{\mathbf{v}'T'} = -\kappa \hat{\kappa} l^2 \Omega \overline{|\nabla T|} \hat{\mathbf{q}}$$

and thus the vector of the specific turbulent heat flux density appearing in the equation of equilibrium of the internal energy (1.13) in the natural coordinate system x'_1, x'_2, x'_3 is:

$$\mathbf{q}_{turb} = \rho c_P \overline{(\mathbf{v}'T')} = -\rho c_P \kappa \hat{\kappa} l^2 \Omega \overline{|\nabla T|} \hat{\mathbf{q}}. \quad (3.20)$$

With the help of the formula of turbulent velocity fluctuation (3.13) the following can be determined in the natural coordinate system x'_1, x'_2, x'_3 one after the other:

a) turbulent kinetic energy:

$$k = \frac{1}{2} \overline{\mathbf{v}' \cdot \mathbf{v}'} = -\frac{1}{2} (\alpha + \beta + \gamma) (\kappa l \Omega)^2, \quad (3.21)$$

b) the vector of triple auto-correlation:

$$\overline{\mathbf{v}' \cdot \mathbf{v}' \cdot \mathbf{v}'} = (l \Omega)^3 \hat{\mathbf{t}}, \quad (3.22)$$

$$\hat{\mathbf{t}} = \begin{pmatrix} \hat{t}_1 \\ \hat{t}_2 \\ \hat{t}_3 \end{pmatrix} = c^3 \begin{pmatrix} \overline{u'_{0\xi}{}^3} + \overline{u'_{0\xi} u'_{0\eta}{}^2} + \overline{u'_{0\xi} u'_{0\zeta}{}^2} \\ \overline{u'_{0\eta} u'_{0\xi}{}^2} + \overline{u'_{0\eta}{}^3} + \overline{u'_{0\eta} u'_{0\zeta}{}^2} \\ \overline{u'_{0\zeta} u'_{0\xi}{}^2} + \overline{u'_{0\zeta} u'_{0\eta}{}^2} + \overline{u'_{0\zeta}{}^3} \end{pmatrix}, \quad (3.23)$$

c) turbulent dissipation:

$$\begin{aligned} \epsilon &= \nu \overline{(\mathbf{v}' \circ \nabla) : (\mathbf{v}' \circ \nabla + \nabla \circ \mathbf{v}')} = \\ &= -\nu \kappa^2 \left\{ \frac{2\alpha + \beta + \gamma}{H_1'^2} \left(\frac{\partial(l\Omega)}{\partial x_1'} \right)^2 + \frac{\alpha + 2\beta + \gamma}{H_2'^2} \left(\frac{\partial(l\Omega)}{\partial x_2'} \right)^2 + \frac{\alpha + \beta + 2\gamma}{H_3'^2} \left(\frac{\partial(l\Omega)}{\partial x_3'} \right)^2 \right. \\ &\quad \left. + 2 \left(\frac{1}{H_1'H_2'} \frac{\partial(l\Omega)}{\partial x_1'} \frac{\partial(l\Omega)}{\partial x_2'} + \frac{\mu}{H_1'H_3'} \frac{\partial(l\Omega)}{\partial x_1'} \frac{\partial(l\Omega)}{\partial x_3'} + \frac{\vartheta}{H_2'H_3'} \frac{\partial(l\Omega)}{\partial x_2'} \frac{\partial(l\Omega)}{\partial x_3'} \right) \right\}. \end{aligned} \quad (3.24)$$

Since the length scale $M_L = l$, time scale $M_T = 1/\Omega$ and velocity scale $M_V = l\Omega$ of turbulence obviously play a decisive role in the formulas of the stochastic turbulence model, the question arises: what is their relation with the length, time and velocity scales of Kolmogorov? The π -theory of dimension analysis will be of assistance in answering it. If we accept that the process of turbulent fluctuation (its internal mechanism) is fundamentally determined by the length scale l , the vortex intensity Ω , the specific turbulent dissipation ϵ and the kinematic viscosity ν of the medium, then these four parameters are the dominant physical characteristics of the turbulence, the dimensions of which expressed in terms of the basis dimensions – length L and time T in our case – assume the following forms:

target variable (a function of the rest):	ϵ turbulent dissipation	$\sim L^2/T^3$
geometrical variable:	l length scale	$\sim L$
process variable:	Ω vortex intensity	$\sim 1/T$
material variable:	ν kinematic viscosity	$\sim L^2/T$

According to the π -theory of dimension analysis it follows from this that if the number of the dominant physical characteristics is: $n = 4$, and the number of basis dimensions is: $m = 2$, then the number of dimensionless physical characteristics determining the process is: $n - m = 2$; and between them exists an implicit relationship of the form $f(\pi_1, \pi_2) = 0$, where

$$\pi_1 = \frac{\nu}{l^2\Omega} \quad ; \quad \pi_2 = \frac{\epsilon}{l^2\Omega^3} \quad (3.25)$$

are the two dimensionless physical characteristics. Choosing the power function

$$f(\pi_1, \pi_2) = \pi_2 - C_E \pi_1^N = 0$$

as the implicit relationship, after substituting the dimensionless characteristics and ordering the equation, the relationship

$$\epsilon = C_E \nu^N (l\Omega)^{2(1-N)} \Omega^{N+1} \quad (3.26)$$

is given for the specific turbulent dissipation ϵ . From the analysis of experimental results the following conclusions can be drawn: on the one hand $N \approx 7/4$, and, on the other, the coefficient C_E is a constant directly proportional with the Reynolds number (calculated with the wall friction velocity).

It takes a short calculation to obtain from the formulas (3.25) the relationships

$$M_L = l = \left(\frac{\pi_2}{\pi_1^3} \right)^{1/4} \left(\frac{\nu^3}{\epsilon} \right)^{1/4} \quad ; \quad M_T = \left(\frac{\pi_2}{\pi_1} \right)^{1/2} \left(\frac{\nu}{\epsilon} \right)^{1/2} \quad ; \quad M_V = \frac{(\epsilon\nu)^{1/4}}{(\pi_1\pi_2)^{1/4}} \quad (3.27)$$

for the length scale l , the time scale $M_T = 1/\Omega$ and the velocity scale $M_V = l\Omega$ of the stochastic turbulence model. Since the length, time and velocity scales of Kolmogorov [4] are all determined by the formulas

$$M_{L,K} = (\nu^3/\epsilon)^{1/4} \quad ; \quad M_{T,K} = (\nu/\epsilon)^{1/2} \quad ; \quad M_{V,K} = (\epsilon\nu)^{1/4} \quad ,$$

equations (3.27) express at the same time the relation between the scales of the stochastic turbulence model and the Kolmogorov scales.

It is worth mentioning that the dimensionless characteristics π_1 is nothing else than the reciprocal value of the Reynolds number $\text{Re}_\Omega = l^2\Omega/\nu$ calculated with the peripheral velocity $l\Omega$ of the form (vortex) with radius l and angular velocity Ω . This Re_Ω -number is related to the turbulent Reynolds number, the Prandt $\text{Re}_T = l\sqrt{k}/\nu$ as follows

$$\text{Re}_T = \kappa \sqrt{-\frac{1}{2}(\alpha + \beta + \gamma) \text{Re}_\Omega} \approx 0.767 \text{Re}_\Omega \quad ,$$

thus the Re_Ω -number is a local dimensionless characteristic of the turbulence.

Summary. The stochastic turbulence model handles turbulent fluctuation processes as the series sum of cosine waves with random phase and random amplitude. It examines turbulent fluctuation, separated from the turbulent mainstream motion developing in the Reynolds mean velocity field, in a relative coordinate system moving steadily at a velocity identical with the Reynolds mean velocity; the base vectors of the coordinate system being identical with those of the natural coordinate system. In the relative coordinate system a particular solution of the equation of motion obtained for turbulent fluctuation can be used to produce one by one the following constant values: elements of the similarity tensor $\alpha, \beta, \gamma, \mu, \vartheta$; scalar components $\hat{t}_1, \hat{t}_2, \hat{t}_3$ of the triple auto-correlation vector; components δ and χ of the direction vector of turbulent heat flux density. Series calculations were performed in order to determine the constants listed and they were compared with the results of several laboratory experimental examinations, and the following proposals were arrived at:

$$\alpha = -3.2 \quad ; \quad \beta = -1.6 \quad ; \quad \gamma = -2.4 \quad ; \quad \mu = \vartheta = 0$$

$$\hat{t}_1 = 1.3 \quad ; \quad \hat{t}_2 = -0.9 \quad ; \quad \hat{t}_3 = -1.0 \quad ; \quad \delta = -0,4 \quad ; \quad \chi = 0 \quad .$$

These α, β, γ values also correspond to the measurement results published by Klebanoff in 1955 [5], according to which turbulence in the boundary layer along the planes is anisotropic, and the following proportionality

$$\overline{v'_1 v'_1} : \overline{v'_2 v'_2} : \overline{v'_3 v'_3} = 4 : 2 : 3$$

holds between the normal components of the Reynolds turbulent stress tensor.

4. Calculating turbulent flow based on the stochastic model

In the Reynolds equation of motion of turbulent flow a divergence of the turbulent stress tensor \mathbf{F}_R arises, which is the sum of the divergence of the deviator of the tensor and the gradient of its first scalar invariant. Thus the first scalar invariant of the turbulent stress tensor \mathbf{F}_R achieves the same role in the equation of motion as the (thermodynamic) pressure p forming the first scalar invariant of the viscous

stress tensor: in the equation of motion the negative gradients of both form part of the specific driving force. Going on with this train of thought: the deviator of the turbulent stress tensor \mathbf{F}_R together with the friction stress tensor forming the deviator of the viscous stress tensor are responsible for the resistance of the fluid to deformation. Thus the apparent increase in viscosity inherent in the turbulent motion of the flowing fluid is caused by the deviator of the Reynolds turbulent stress tensor. Following from equation (3.16), the deviator $\boldsymbol{\sigma}_R$ of the stress tensor \mathbf{F}_R can be expressed in the natural coordinate system x'_1, x'_2, x'_3 with the deviator of the similarity tensor:

$$\boldsymbol{\sigma}_R(x'_1, x'_2, x'_3, t) = \Theta(x'_1, x'_2, x'_3, t) \mathbf{H}_* ,$$

where Θ is the dominant turbulent shear stress according to equation (3.15), and \mathbf{H}_* is the deviator of the similarity tensor:

$$\mathbf{H}_* = \begin{pmatrix} \alpha_* & 1 & \mu \\ 1 & \beta_* & \vartheta \\ \mu & \vartheta & \gamma_* \end{pmatrix} = \begin{pmatrix} \frac{1}{3}(2\alpha - \beta - \gamma) & 1 & \mu \\ 1 & \frac{1}{3}(2\beta - \gamma - \alpha) & \vartheta \\ \mu & \vartheta & \frac{1}{3}(2\gamma - \alpha - \beta) \end{pmatrix} .$$

Then the turbulent stress tensor \mathbf{F}_R in the natural coordinate system can be written in the form

$$\mathbf{F}_R(x'_1, x'_2, x'_3, t) = S_I \mathbf{I} + \Theta \mathbf{H}_* , \quad (4.1)$$

where \mathbf{I} is the unit tensor, and S_I is the first scalar invariant of the stress tensor \mathbf{F}_R , which can be expressed using the specific turbulent kinetic energy k as follows:

$$S_I = -\frac{1}{3}\rho \left(\overline{\mathbf{v}'_1 \mathbf{v}'_1} + \overline{\mathbf{v}'_2 \mathbf{v}'_2} + \overline{\mathbf{v}'_3 \mathbf{v}'_3} \right) = -\frac{2}{3}\rho k . \quad (4.2)$$

Since the natural coordinate system x'_1, x'_2, x'_3 is not fixed in space, but changes from point to point in the flow space (Figure 1), it can only be used with limitations in the numerical solution of the concrete flow problems. It is expedient to perform the numerical calculations in a fixed coordinate system, consequently, the vector and tensor quantities have to be transformed from the natural coordinate system into a calculation coordinate system matching the problem to be solved according to equations (3.1)-(3.2). In the transformation the point-wise values of dominant turbulent shear stress Θ and scalar invariant S_I being scalar functions – do not change, and the transformed of the unit tensor \mathbf{I} also remains a unit tensor, thus the transformation of the turbulent stress tensor \mathbf{F}_R affects only the deviator \mathbf{H}_* :

$$\mathbf{G}(x_1, x_2, x_3, t) = \mathbf{E} \cdot \mathbf{H}_* \cdot \mathbf{E}^T . \quad (4.3)$$

Next the Reynolds turbulent stress tensor assumes the following form:

$$\mathbf{F}_R(x_1, x_2, x_3, t) = -\rho \frac{2}{3} k \mathbf{I} + \Theta \mathbf{G} \quad (4.4)$$

in the calculation coordinate system x_1, x_2, x_3 . Since the apparent increase in viscosity mentioned is caused by the deviator $\boldsymbol{\sigma}_R = \Theta \mathbf{G}$ the deviator \mathbf{G} defined by equation (4.3) will be called vortex viscosity tensor in what follows.

The tensor and its transformed of the natural x'_1, x'_2, x'_3 and the calculation coordinate system x_1, x_2, x_3 can be written in the following matrix form:

$$\mathbf{E} = \begin{pmatrix} E_{11} & E_{12} & E_{13} \\ E_{21} & E_{22} & E_{23} \\ E_{31} & E_{32} & E_{33} \end{pmatrix} ; \quad \mathbf{E}^T = \begin{pmatrix} E_{11} & E_{21} & E_{31} \\ E_{12} & E_{22} & E_{32} \\ E_{13} & E_{23} & E_{33} \end{pmatrix}. \quad (4.5)$$

The scalar elements are determined by the scalar components (physical coordinates) of the velocity vector \mathbf{v} and the vortex vector $\boldsymbol{\Omega} = \nabla \times \mathbf{v}$ in the calculation coordinate system x_1, x_2, x_3 :

$$\begin{aligned} E_{11} &= \frac{1}{\sqrt{1-S^2}} \left(\frac{v_1}{v} - S \frac{\Omega_1}{\Omega} \right) ; & E_{12} &= \frac{1}{\sqrt{1-S^2}} \frac{v_2 \Omega_3 - v_3 \Omega_2}{v \Omega} ; & E_{13} &= -\frac{\Omega_1}{\Omega} \\ E_{21} &= \frac{1}{\sqrt{1-S^2}} \left(\frac{v_2}{v} - S \frac{\Omega_2}{\Omega} \right) ; & E_{22} &= \frac{1}{\sqrt{1-S^2}} \frac{v_3 \Omega_1 - v_1 \Omega_3}{v \Omega} ; & E_{23} &= -\frac{\Omega_2}{\Omega} \\ E_{31} &= \frac{1}{\sqrt{1-S^2}} \left(\frac{v_3}{v} - S \frac{\Omega_3}{\Omega} \right) ; & E_{32} &= \frac{1}{\sqrt{1-S^2}} \frac{v_1 \Omega_2 - v_2 \Omega_1}{v \Omega} ; & E_{33} &= -\frac{\Omega_3}{\Omega} \\ v &= |\mathbf{v}| ; & \Omega &= |\nabla \times \mathbf{v}| ; & S &= \frac{v_1 \Omega_1 + v_2 \Omega_2 + v_3 \Omega_3}{v \Omega}. \end{aligned}$$

If now the expression (4.4) of the turbulent stress tensor \mathbf{F}_R is substituted into the equation of motion (1.9), then after the introduction of the so-called total potential determined by the equation

$$\Pi = U + \frac{p}{\rho} - \frac{S_I}{\rho} = U + \frac{p}{\rho} + \frac{2}{3}k, \quad (4.6)$$

the Reynolds equation of motion describing the turbulent motion of the incompressible fluid is obtained in the following form:

$$\frac{\partial \mathbf{v}}{\partial t} + (\mathbf{v} \cdot \nabla) \mathbf{v} = -\nabla \Pi + \nu \Delta \mathbf{v} + \frac{1}{\rho} \text{Div}(\boldsymbol{\Theta} \mathbf{G}). \quad (4.7)$$

This equation is the equation of equilibrium of the momentum transport of turbulent flow, where the terms have the following physical meanings: the two terms on the left-hand side are the substantial (complete in time) change of the momentum; the first term on the right-hand side is the specific driving force relating to mass unit, the second and the third terms are the specific resistance of the fluid to deformation, which result from, on the one hand, the molecular viscosity of the fluid, and, on the other, from the change of momentum resulting from the turbulent motion of the fluid particles.

In turbulent flow problems the equation of motion (4.7) and the equation of continuity

$$\nabla \cdot \mathbf{v} = 0 \quad (4.8)$$

expressing the conservation of mass of incompressible fluids are generally used as basic equations. But the Poisson-equation of the total potential Π may also be included among the basic equations, as it can be derived from the equation of motion (4.7) according to what follows under consideration of the equation of continuity (4.8). If

the medium in flow is incompressible, then taking the divergence of each member in equation (4.7) gives the following equation:

$$\nabla \cdot (\mathbf{v} \cdot \nabla) \mathbf{v} = -\Delta \Pi + \frac{1}{\rho} \nabla \cdot \text{Div} (\Theta \mathbf{G})$$

For an incompressible fluid – with respect to the expansion rule

$$(\mathbf{a} \circ \mathbf{b}) : (\mathbf{c} \circ \mathbf{d}) = (\mathbf{a} \cdot \mathbf{c})(\mathbf{d} \cdot \mathbf{b})$$

of the double scalar product of dyads – the following is obtained:

$$\nabla \cdot [(\mathbf{v} \cdot \nabla) \mathbf{v}] = \nabla \cdot [(\mathbf{v} \circ \mathbf{v}) \cdot \nabla] = (\mathbf{v} \circ \nabla) : (\nabla \circ \mathbf{v}) ,$$

which gives the following Poisson-equation referring to the total potential:

$$\Delta \Pi = -(\mathbf{v} \circ \nabla) : (\nabla \circ \mathbf{v}) + \frac{1}{\rho} \nabla \cdot \text{Div} (\Theta \mathbf{G}) . \tag{4.9}$$

It is easy to understand that supplementing the equation of motion (4.7) – either with the differential equation (4.8) or (4.9) – does not produce a closed system of equations in terms of solving the turbulent flow problem. Namely, in the system of equations formed by the four scalar differential equations the number of unknown functions – the three velocity components, the total potential Π and the dominant turbulent shear stress Θ – exceeds the number of equations, and thus the system of equations remains underdetermined. (The vortex viscosity tensor \mathbf{G} does not increase the number of unknowns, for in its elements besides the constant elements of the similarity tensor \mathbf{H} the velocity components and their place-derivates appear.)

Owing to its underdetermined character, in turbulent flow it is necessary to supplement this system of equations with further equations so that it can be solved. There are several possibilities for this.

a) For some turbulent flows with simpler geometrical configurations the scale function $l(\mathbf{x})$ of the turbulence is known, so it can be given in advance. In such a case it is possible to add the algebraic equation

$$\Theta(\mathbf{x}, t) = \rho (\kappa l \Omega)^2 \tag{4.10}$$

to the four partial differential equations and then the system of equations to be solved is formed by the four scalar partial differential equations and the algebraic equation (4.10) added. The system of equations formed by the total of five equations is suitable for determining the five unknowns: the three velocity components as well as Π and Θ ; this is the *algebraic version* of the stochastic turbulence model.

b) The four partial differential equations are supplemented with a fifth differential equation, in which, however, new unknowns may appear, and thus further algebraic equations have to be added, in which there are no more new unknowns, which results in a closed system of equations formed by differential and algebraic equations. As the fifth differential equation it is possible to choose equation (3.24) of the stochastic turbulence model after it has been transformed into the calculation coordinate system

x_1, x_2, x_3 :

$$\nu\kappa^2 \{ (2\alpha + \beta + \gamma) A^2 + (\alpha + 2\beta + \gamma) B^2 + (\alpha + \beta + 2\gamma) C^2 + 2(AB + \mu AC + \vartheta BC) \} + \epsilon = 0 \quad (4.11)$$

$$\begin{aligned} A &= \frac{\partial(l\Omega)}{H_1' \partial x_1'} = E_{11} \frac{\partial(l\Omega)}{H_1 \partial x_1} + E_{12} \frac{\partial(l\Omega)}{H_2 \partial x_2} + E_{13} \frac{\partial(l\Omega)}{H_3 \partial x_3} \\ B &= \frac{\partial(l\Omega)}{H_2' \partial x_2'} = E_{21} \frac{\partial(l\Omega)}{H_1 \partial x_1} + E_{22} \frac{\partial(l\Omega)}{H_2 \partial x_2} + E_{23} \frac{\partial(l\Omega)}{H_3 \partial x_3} \\ C &= \frac{\partial(l\Omega)}{H_3' \partial x_3'} = E_{31} \frac{\partial(l\Omega)}{H_1 \partial x_1} + E_{32} \frac{\partial(l\Omega)}{H_2 \partial x_2} + E_{33} \frac{\partial(l\Omega)}{H_3 \partial x_3} . \end{aligned}$$

With this addition, however, the five unknowns – the three velocity components, Π and Θ – in the original four partial differential equations have been increased by two more: the velocity scale $l\Omega$ and the specific turbulent dissipation ϵ , thus another two algebraic equations have to be added in order to obtain a closed system of equations. One is (4.10), and the other is equation (3.26) of turbulent dissipation ϵ :

$$\epsilon = C_E \nu^N (l\Omega)^{2(1-N)} \Omega^{N+1} . \quad (4.12)$$

The system of equations to be solved – the original four + the supplementary (4.11) – is thus formed by five scalar partial differential equations, as well as the two algebraic equations (4.10) and (4.12) added; that is a total of seven equations. The number of unknowns is also seven: $v_1, v_2, v_3, \Pi, \Theta, l\Omega$, and ϵ , thus the system of equations formed by the five partial differential equations + two algebraic equations is closed; this is the *one-equation version* of the stochastic turbulence model.

c) The equation of equilibrium (1.18) of turbulent kinetic energy can be used as the second differential equation to supplement the original four partial differential equations, after some formulas of the stochastic turbulence model have been introduced into it. The first such formula results from the formula (4.4) of the Reynolds turbulent stress tensor:

$$\overline{\mathbf{v}' \circ \mathbf{v}'} = \frac{2}{3} k \mathbf{I} - \frac{1}{\rho} \Theta \mathbf{G} , \quad (4.13)$$

the second is the formula of the velocity-pressure correlation $\overline{\mathbf{v}' p'}$, which, following Prandtl [6] is written in the form

$$\overline{\mathbf{v}' p'} = -\rho \nu_t \nabla k / C_k$$

where $C_k \approx 0.75$. Here ν_t is the Boussinesq vortex viscosity factor, which is equal to the product of the length scale l and the square root of the turbulent kinetic energy k ; with respect to the relationship (3.21) of the turbulence model, the following is obtained for it:

$$\nu_t = l\sqrt{k} = \kappa a l^2 \Omega \quad ; \quad a = \sqrt{-\frac{1}{2}(\alpha + \beta + \gamma)} .$$

Now the formula of the velocity-pressure correlation assumes the following form:

$$\overline{\mathbf{v}' p'} = -\rho \frac{\kappa a}{C_k} l^2 \Omega \nabla k . \quad (4.14)$$

The third formula results from the form of the triple auto-correlation determined by equation (3.22) in the natural coordinate system transformed into the calculation coordinate system:

$$\overline{\mathbf{v}' \cdot \mathbf{v}' \cdot \mathbf{v}'} = (l\Omega)^3 \mathbf{t} \quad ; \quad \mathbf{t} = \mathbf{E} \cdot \hat{\mathbf{t}}. \tag{4.15}$$

Finally, after substituting and ordering the relationships (4.13)-(4.15), the equation of equilibrium (1.18) of turbulent kinetic energy assumes the following form:

$$\frac{dk}{dt} = \frac{1}{\rho} \Theta \mathbf{G} : (\nabla \circ \mathbf{v}) - \epsilon - \nabla \cdot \left[\frac{1}{2} (l\Omega)^3 \mathbf{t} - \left(\frac{5}{3} \nu + \frac{\kappa a}{C_k} \frac{(l\Omega)^2}{\Omega} \right) \nabla k + \frac{\nu}{\rho} \text{Div}(\Theta \mathbf{G}) \right]. \tag{4.16}$$

This can be used as the second supplementary equation of the four original partial differential equations given by the equation of continuity and the three Reynolds scalar equations of motion. Thus – supplementing the four original scalar differential equations with the partial differential equations (4.11) and (4.16) and adding the algebraic equations (4.10) and (4.12) – a closed system of equations with eight members is obtained for determining the total of eight unknown functions ($v_1, v_2, v_3, \Pi, \Theta, l\Omega, k$ and ϵ); this is the *two-equation version* of the stochastic turbulence model. It is easy to see that also when the latter version is chosen, the first step of the calculation is given by performing the one-equation version under b), and only then comes as a second step the solution of the differential equation (4.16) by using the functions determined above, which gives the distribution of turbulent kinetic energy $k(\mathbf{x}, t)$.

d) Finally it is worth noting that it is possible to choose the equation of equilibrium (4.16) as the fifth equation supplementing the four original partial differential equations instead of (4.11). Then due to the appearance of the three new unknown functions (k, ϵ and $l\Omega$), it becomes necessary to add three more algebraic equations: equations (4.10) and (4.12) and equation

$$k = (a\kappa l\Omega)^2 \tag{4.17}$$

resulting from (3.21) via the notation $a^2 = -(\alpha + \beta + \gamma)/2$; thus a closed system of equations is obtained, which may be called the *second one-equation version* of the stochastic turbulence model, and which corresponds – essentially – to the one-equation model published by Bradshaw, Ferris and Atwell [7]. Then it is no coincidence that the value $1/a^2 = 0.278$ in equation (4.17) – calculated with the constants of the stochastic turbulence model – is a good approximation of the Bradshaw-constant (≈ 0.3) [8] expressing the ratio between turbulent shear stress and turbulent kinetic energy.

In order to solve the underdetermined character of the differential equation system describing turbulent flow the first three of the four versions described above are evidently easier to handle than the fourth one, and according to our experience so far the results obtained from them give a good approximation of reality, versions a)-c) are to be given preference to version d).

In the knowledge of the distributions of the dominant turbulent shear stress $\Theta(\mathbf{x}, t)$ and turbulent kinetic energy $k(\mathbf{x}, t)$ the further scalar elements of the Reynolds turbulent stress tensor \mathbf{F}_R can be determined on the basis of tensor equation (4.4) as:

$$\overline{v'_i v'_i} = \frac{2}{3}k - (\kappa l \Omega)^2 G_{ii} \quad ; \quad i = 1, 2, 3, \quad (4.18)$$

$$\overline{v'_i v'_j} = -(\kappa l \Omega)^2 G_{ij}. \quad (4.19)$$

It is worth noting here that these formulas of the scalar elements of the turbulent stress tensor can also be used in the one-equation version as well, if the distribution of turbulent kinetic energy k is calculated in the knowledge of the velocity scale $l\Omega$ using the relationship (4.17).

5. Turbulent flow in a straight pipe with circular cross-section

Let us take as an example a steady turbulent flow in a long straight pipe, which can be assumed to be rotation-symmetric and that only the axial component of the Reynolds time-mean average speed is not zero, and the other two components disappear. The computations are performed in the cylinder-coordinate system x, r, φ , and the following hold for the velocity and vortex components:

$$v_x = v(r) \quad ; \quad v_r = v_\varphi = 0 \quad ; \quad \Omega_x = \Omega_r = 0 \quad ; \quad \Omega_\varphi = -\frac{dv}{dr} \quad ; \quad \Omega = |\Omega_\varphi| = \left| \frac{dv}{dr} \right|.$$

From all this it also follows that the dominant turbulent shear stress is a function of only the coordinate r : $\Theta(r)$. The elements of the tensor \mathbf{E} of the transformation between the natural and the calculation coordinate systems and of the vortex viscosity tensor \mathbf{G} now take the forms:

$$\mathbf{E} = \begin{pmatrix} 1 & 0 & 0 \\ 0 & -1 & 0 \\ 0 & 0 & -1 \end{pmatrix} \quad ; \quad \mathbf{G} = \begin{pmatrix} \alpha_* & -1 & 0 \\ -1 & \beta_* & 0 \\ 0 & 0 & \gamma_* \end{pmatrix}.$$

A short calculation gives the following forms for the components in directions x and r of the divergence of the Reynolds turbulent stress tensor:

$$\text{Div} (\Theta \mathbf{G})|_x = -\frac{1}{r} \frac{d(r\Theta)}{dr} \quad ; \quad \text{Div} (\Theta \mathbf{G})|_r = \frac{\beta_*}{r} \frac{d(r\Theta)}{dr} - \frac{\gamma_*}{r} \Theta.$$

Then the two scalar equations of motion assume the forms:

$$0 = -\frac{\partial \Pi}{\partial x} + \frac{\nu}{r} \frac{d}{dr} \left(r \frac{dv}{dr} \right) - \frac{1}{r} \frac{d(r\Theta)}{dr} \quad (5.1)$$

$$0 = -\frac{\partial \Pi}{\partial r} + \frac{\beta_*}{r} \frac{d(r\Theta)}{dr} - \frac{\gamma_*}{r} \Theta \quad (5.2)$$

and the first supplementary differential equation assumes the form:

$$\nu \kappa^2 (\alpha + 2\beta + \gamma) \left(\frac{d(l\Omega)}{dr} \right)^2 + \epsilon = 0. \quad (5.3)$$

Since in these three differential equations there are altogether five unknown functions – velocity v , total potential Π , dominant turbulent shear stress Θ , velocity scale $l\Omega$

of fluctuation and specific turbulent dissipation ϵ –, two algebraic equations have to be added which contain no new unknown function:

$$\Theta = \rho(\kappa l\Omega)^2 \quad (5.4)$$

$$\epsilon = C_E \nu^N (l\Omega)^{2(1-N)} |dv/dr|^{N+1} . \quad (5.5)$$

It is easy to see that the system of equations (5.1)-(5.5) is a closed system from the point of determining the five unknown functions, thus this case represents an application of the *one-equation version* of the stochastic turbulence model.

In order to determine the elements of the turbulent stress tensor it is necessary to solve the second supplementary differential equation – the equation of equilibrium of the turbulent kinetic energy – as well:

$$0 = \frac{\Theta}{\rho} \frac{dv}{dr} + \varepsilon - \frac{1}{r} \frac{d}{dr} \left\{ r \left[\frac{\hat{t}}{2} \frac{dv}{dr} (l\Omega)^3 + \left(\frac{5\nu}{3} + \frac{\kappa a}{C_k} \frac{(l\Omega)^2}{\Omega} \right) \frac{dk}{dr} - \frac{\nu}{\rho} \left(\frac{\beta_*}{r} \frac{d(r\Theta)}{dr} - \frac{\gamma_*}{r} \Theta \right) \right] \right\} . \quad (5.6)$$

In this differential equation only the specific turbulent kinetic energy k appears as a new unknown function, therefore the system of equations (5.1)-(5.6) forms a closed system regarding the determination of the six unknown functions: velocity v , total potential Π , dominant turbulent shear stress Θ , the velocity scale $l\Omega$ of turbulent fluctuation, turbulent dissipation ϵ , and turbulent kinetic energy k . The numerical solution of this system of equations with six members represents the *two-equation version* of the stochastic turbulence model.

Equations (5.1)-(5.2) make it easy to see that the partial derivative of the total potential $\Pi(x, r)$ according to x is constant, which can be expressed by the drop in potential $\Delta\Pi$ measured on the pipe-section of length L as follows: $\partial\Pi/\partial x = -\Delta\Pi/L$. As usual, the viscous shear stress on the pipe wall is used to define the wall friction velocity v_* :

$$v_* = \sqrt{\frac{|\tau_{wall}|}{\rho}} = \sqrt{\frac{\Delta\Pi R}{2L}} ,$$

where R is the pipe radius. If the Reynolds number $\text{Re}_* = v_* R/\nu$ calculated with the wall friction velocity v_* as well as the dimensionless place coordinate $\xi = r/R$, the dimensionless velocity $V = v/v_*$ and the dimensionless velocity scale $Y = l\Omega/v_*$ are introduced, the differential equations (5.1) and (5.3) after the substitution of the algebraic equations (5.4) and (5.5) assume the forms:

$$\frac{dV}{d\xi} = \text{Re}_* (\kappa^2 Y^2 - \xi) \quad (5.7)$$

$$a_* \kappa \frac{dY}{d\xi} = \frac{\sqrt{C_E}}{\text{Re}_*^{(N-1)/2}} Y^{1-N} \left| \frac{dV}{d\xi} \right|^{\frac{N+1}{2}} , \quad (5.8)$$

where on the basis of analysing the measurement results $N \approx 7/4$, and

$$a_* = \sqrt{-\alpha - 2\beta - \gamma} .$$

The coefficient C_E depends, beyond depending on the Re_* -number, on the spatial coordinate ξ :

$$C_E = C_0 (1 - \xi)^3 \quad ; \quad C_0 = (0.09 \dots 0.16) Re_* .$$

Reducing equations (5.7) and (5.8) gives for the velocity scale Y the differential equation

$$\frac{dY}{d\xi} = \frac{Re_* \sqrt{C_E}}{a_* \kappa} Y^{1-N} \left| \kappa^2 Y^2 - \xi \right|^{\frac{N+1}{2}} .$$

It is easy to see that the introduction of the function

$$U = Y^N$$

results in the differential equation to be solved assuming the form

$$\frac{dU}{d\xi} = N \frac{Re_* \sqrt{C_E}}{a_* \kappa} \left| \kappa^2 U^{2/N} - \xi \right|^{\frac{N+1}{2}} ,$$

which is easy to integrate numerically with the Runge-Kutta method. When the distribution $Y(\xi)$ is known, integration of the equation (5.7) determines the dimensionless velocity distribution $V(\xi)$. The dimensionless velocity maximum playing the role of integration constant depends on the Re_* -number:

$$V_{\max} = 6 + \frac{1}{\kappa} \ln Re_* . \tag{5.9}$$

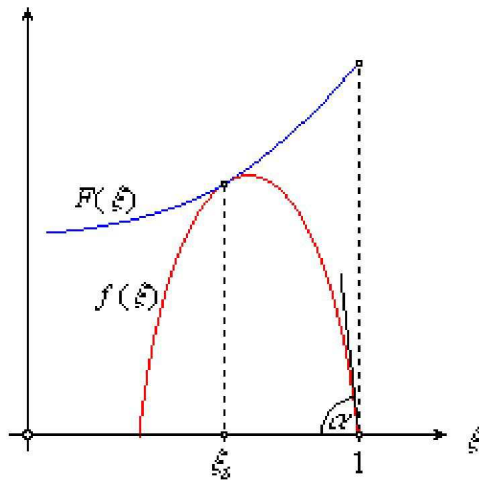


Figure 2. Smooth fitting of the turbulent distribution onto distribution in a viscous sub-layer

With respect to the fact that the differential equation (3.9) forming the basic equation of the stochastic turbulence model and the vector function (3.10) obtained as its solution for turbulent velocity fluctuation are valid for the fully developed turbulent motion – and this restriction applies to all the relationships derived from it –, the differential equations (5.7)-(5.8) do not hold in the thin viscous sublayer

adhering to the pipe wall. As a result, in the calculation of the functions $Y(\xi)$ and $V(\xi)$, the zero boundary conditions relating to the pipe wall can be fulfilled by the smooth fitting of the viscous sublayer onto the distributions disappearing next to the wall. For the turbulent distribution $F(\xi)$, the polynomial of the form

$$f(\xi) = (a + b\xi)(1 - \xi) \quad ; \quad \xi_\delta \leq \xi \leq 1 \tag{5.10}$$

is used to approximate the smoothly fitting distribution in place ξ_δ , where the coefficients a and b can be determined by fulfilling the conditions of smooth fitting, according to which the two functions fitting each other and their first derivatives are identical in place ξ_δ of the fitting (Figure 2), which results in the following:

$$a = F(\xi_\delta) \frac{1 - 2\xi_\delta}{(1 - \xi_\delta)^2} - F'(\xi_\delta) \frac{\xi_\delta}{1 - \xi_\delta} \quad ; \quad b = F(\xi_\delta) \frac{1}{(1 - \xi_\delta)^2} + F'(\xi_\delta) \frac{1}{1 - \xi_\delta} .$$

Experimental experience shows that the derivative of the velocity distribution $V(\xi)$ on the wall (in place $\xi = 1$) both for the laminar and turbulent cases is

$$V'(1) = -\text{Re}_* .$$

For $f(\xi)$ replacing $F(\xi)$

$$f'(1) = -\tan \alpha = -(a + b)$$

holds (Figure 2), thus for $V(\xi)$ the condition

$$a + b = \text{Re}_*$$

has to hold, which, after the substitution of the previous formulas of the coefficients a and b gives the equation

$$2V(\xi_\delta) + (1 - \xi_\delta) [v'(\xi_\delta) - \text{Re}_*] = 0 \tag{5.11}$$

for determining the coordinates ξ_δ of smooth fitting. When ξ_δ is known, it is possible to calculate also the coordinates a and b of the distributions in the viscous sublayer not only in terms of the dimensionless velocity scale $Y(\xi)$ and the dimensionless velocity $V(\xi)$, but also in terms of the other turbulent distribution as well. It follows from all this that the place coordinate ξ_δ determined by means of equation (5.11) can be considered to be the boundary of the viscous sublayer, where the turbulent distributions smoothly fit the laminar distributions fulfilling the zero boundary condition valid on the pipe wall.

When the dimensionless velocity scale $Y(\xi)$ is known, the as yet unknown further turbulent distributions can be determined: the dimensionless distribution of the dominant turbulent shear stress of the form

$$\frac{\Theta}{\rho v_*^2} = \kappa^2 Y^2 \tag{5.12}$$

and the dimensionless distribution of the specific turbulent dissipation of the form

$$\frac{\epsilon R}{v_*^3} = C_E \text{Re}_* Y^{2(1-N)} |\kappa^2 Y^2 - \xi|^{N+1} . \tag{5.13}$$

Finally the integration of differential equation (5.2) gives for the dimensionless total potential the equation

$$\frac{\Pi(x, \xi)}{v_*^2} = \frac{\Pi_0}{v_*^2} - \frac{\Delta\Pi}{v_*^2} \frac{x}{L} + \beta_* \kappa^2 Y^2 + (\beta_* - \gamma_*) \kappa^2 \int_0^\xi Y^2 \frac{d\xi}{\xi} \quad (5.14)$$

for the integration constant Π_0/v_*^2 neglecting the field forces, the following form is obtained:

$$\frac{\Pi_0}{v_*^2} = \frac{p_0}{\rho v_*^2} - \kappa^2 \frac{\alpha + \beta + \gamma}{3},$$

where p_0 is pressure in the middle of the initial cross-section of the pipe section (in place $x = 0$) and $\Delta\Pi$ is the total potential drop in section with length L . The calculation of the distribution of the total potential gives the last step of the *one-equation version* of the stochastic turbulence model.

In order to determine the distribution of the specific turbulent kinetic energy it is necessary to solve the – second supplementary – differential equation (5.6) numerically. When the distribution $Y(\xi)$ is known, the differential equation (5.6) can be made with some modification – including one integration in terms of ξ – suitable for determining the distribution of the dimensionless specific turbulent kinetic energy $K = k/v_*^2$:

$$\left\{ \frac{5}{3} + \frac{\kappa a}{C_k} \frac{Y^2}{|\kappa^2 Y^2 - \xi|} \right\} \frac{dK}{d\xi} - 2\kappa \frac{\beta_*}{a_*} \text{Re}_* \sqrt{C_E} Y^{2-N} |\kappa^2 Y^2 - \xi|^{\frac{N+1}{2}} + \\ + \text{Re}_* \frac{\hat{t}_2}{2} Y^3 - \kappa^2 (\beta_* - \gamma_*) \frac{Y^2}{\xi} - \text{Re}_*^2 F(\xi) = 0, \quad (5.15)$$

where $C_k \approx 0.75$, and

$$F(\xi) = \frac{1}{\xi} \int_0^\xi \left\{ \kappa^2 Y^2 (\kappa^2 Y^2 - \xi) + C_E Y^{2(1-N)} |\kappa^2 Y^2 - \xi|^{N+1} \right\} \xi d\xi.$$

When the distribution of the dimensionless velocity scale $Y(\xi)$ is known (i.e. it has been determined on the basis of the one-equation version), there is no obstacle in the way of the numerical solution of the differential equation (5.15). For the integration constant K_0 the formula

$$K_0 = -\kappa^2 \frac{\alpha + \beta + \gamma}{2}$$

can be recommended, which is also supported by measurement results.

Next – when the distributions $K(\xi)$ and $Y(\xi)$ are known – the formulas (4.18)-(4.19) can be used to calculate the scalar elements different from zero of the Reynolds turbulent stress tensor as well:

$$F_{R_{11}} = \frac{\overline{v'_x v'_x}}{v_*^2} = 2K(\xi) \frac{\alpha}{\alpha + \beta + \gamma} \quad ; \quad F_{R_{22}} = \frac{\overline{v'_r v'_r}}{v_*^2} = 2K(\xi) \frac{\beta}{\alpha + \beta + \gamma} \\ F_{R_{33}} = \frac{\overline{v'_\varphi v'_\varphi}}{v_*^2} = 2K(\xi) \frac{\gamma}{\alpha + \beta + \gamma} \quad ; \quad F_{R_{12}} = \frac{\overline{v'_x v'_r}}{v_*^2} = \kappa^2 Y^2(\xi).$$

In the viscous sublayer – similarly to equations (5.7)-(5.8) and for the same reason – the differential equation (5.15) also loses its validity, therefore the zero boundary conditions referring to the pipe wall for the main stresses can also be fulfilled by smooth fitting on the distributions disappearing on the wall. The connection between the distributions in turbulent and sublayer zones can be approximated by a third order polynomial for $v'_x v'_x / v_*^2$ and by a second polynomial for the other two main stresses. The place ξ_F of the fitting of the velocity distribution $V(\xi)$ is in the vicinity of the place of fitting of ξ_δ : $\xi_F \leq \xi_\delta$ (it is smaller for larger Re_* -numbers). In a second order approximation the main stress distribution $F(\xi)$ in the viscous sublayer is replaced by the following function

$$f(\xi) = F(\xi_F) \frac{(1-\xi)(b+\xi)}{(1-\xi_F)(b+\xi_F)} \quad ; \quad \xi_F \leq \xi \leq 1 ,$$

where the coefficient b can be determined as follows:

$$b = \frac{1 - (B+2)\xi_F}{B+1} \quad ; \quad B = \frac{F'(\xi_F)}{F(\xi_F)} (1 - \xi_F) .$$

In a third-order approximation the main stress distribution $F(\xi)$ in the viscous sublayer is replaced by the function

$$f(\xi) = F(\xi_F) \frac{(1-\xi)(\xi^2 + b\xi + c)}{(1-\xi_F)(\xi_F^2 + b\xi_F + c)} \quad ; \quad \xi_F \leq \xi \leq 1 .$$

In this case the value of the maximum of the main stress – assumed in the viscous sublayer – is also to be given, which according to experimental experience is a function of the Re_* -number:

$$f_m = \frac{7 \text{Re}_* - 475}{\text{Re}_* - 50}$$

and then the coefficients b and c as well as the place of maximum ξ_m are to be determined iteratively on the basis of the formulas

$$b = \frac{(B+1)(2-3\xi_m)\xi_m + (B+3)\xi_F^2 - 2\xi_F}{(B+1)(2\xi_m-1) - (B+2)\xi_F + 1}$$

$$c = (2-3\xi_m)\xi_m + (1-2\xi_m)b ,$$

while the condition $f(\xi_m) = f_m$ is simultaneously fulfilled. Determining also the distribution of the scalar elements of the Reynolds turbulent stress tensor in the viscous sublayer has performed the last step in the *two-equation version* of the stochastic turbulence model.

Figure 3 shows the solutions of the differential equations (5.7), (5.8) and (5.15) describing the turbulent flow in a pipe with circular cross-section for three different Re_* -numbers ($\text{Re}_{*1} = 100$, $\text{Re}_{*2} = 1000$ and $\text{Re}_{*3} = 10000$) against the dimensionless place coordinate $y^+ = \text{Re}_*(1 - r/R)$. Notations: $V(y^+)$ is velocity, $Y(y^+)$ is velocity scale and $K(y^+)$ is turbulent kinetic energy (all are made dimensionless by means of the wall friction velocity v_*). For the sake of better comparison, the Figure also includes the Prandtl universal turbulent velocity profile $V = \frac{1}{\kappa} \ln y^+ + 5$ and the laminar velocity distribution $V = y^+$ of the viscous sublayer. Our experience shows that for the stability of the calculation it is necessary to choose the division of the

interval $0 \leq \xi \leq 1$ to be at least 5000; and so that it increases with the Re_* -number (5000 is sufficient for $Re_* = 100$, while 15000 is recommended for $Re_* = 10000$).

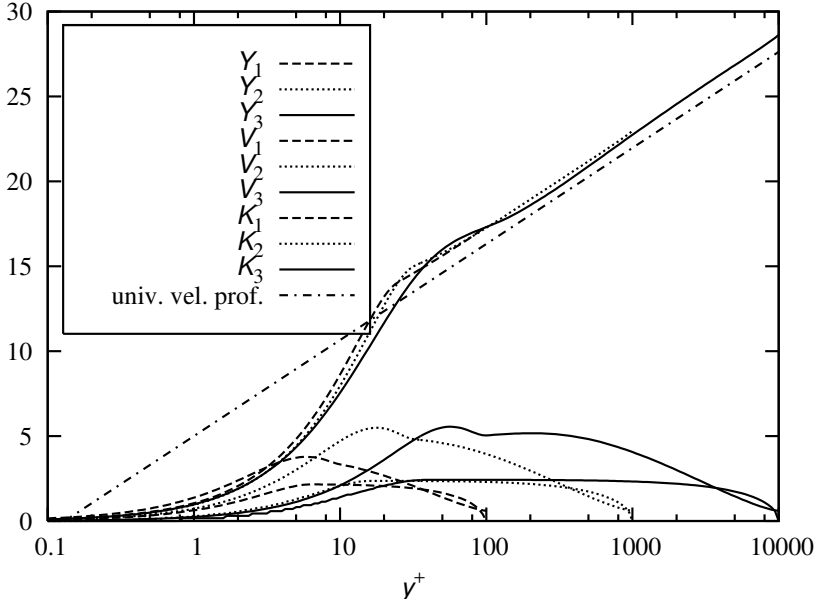


Figure 3. Solutions for Y , V , K of the differential equation of turbulent flow in a pipe for three different Re_* -numbers.

Figure 4 shows a comparison of calculated velocity distribution for two different Reynolds-numbers with the measurement results of Laufer [9]; the Reynolds-numbers of the identification are calculated using the velocity maximum because that was used in the measurements as well. Since it is expedient to use the number $Re_* = v_* R / \nu$ calculated with the wall friction velocity v_* for identifying the numerical calculations, the Re_m and Re_* numbers: $Re_{m_a} = 50000$ and $Re_{*a} = 1079.44$ as well as $Re_{m_b} = 500000$ and $Re_{*b} = 8826.69$ corresponding to each other in the two cases shown in the Figure are given. The figures show a good correlation between the calculated and measured results.

Figure 5 shows a comparison between the calculated results of the scalar elements along the main diagonal of the Reynolds turbulent stress tensor (i.e. the main stresses) while Figure 6 shows a comparison between the calculated results of turbulent shear stresses as well as those of velocity profiles in terms of the velocity maximum and the measurement results of Laufer [9] for the same two Re_m -numbers.

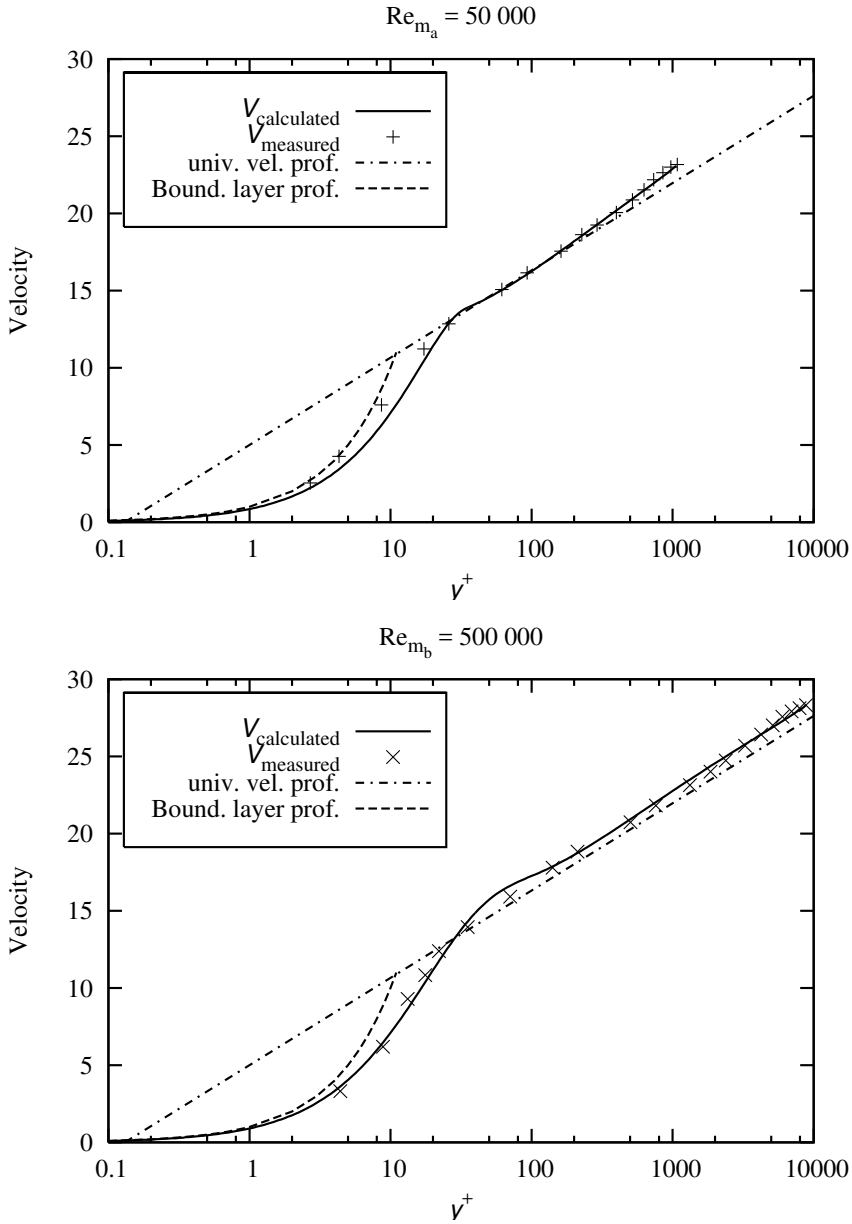


Figure 4. Comparison of calculated velocity distributions with the measurement results of Laufer [9].

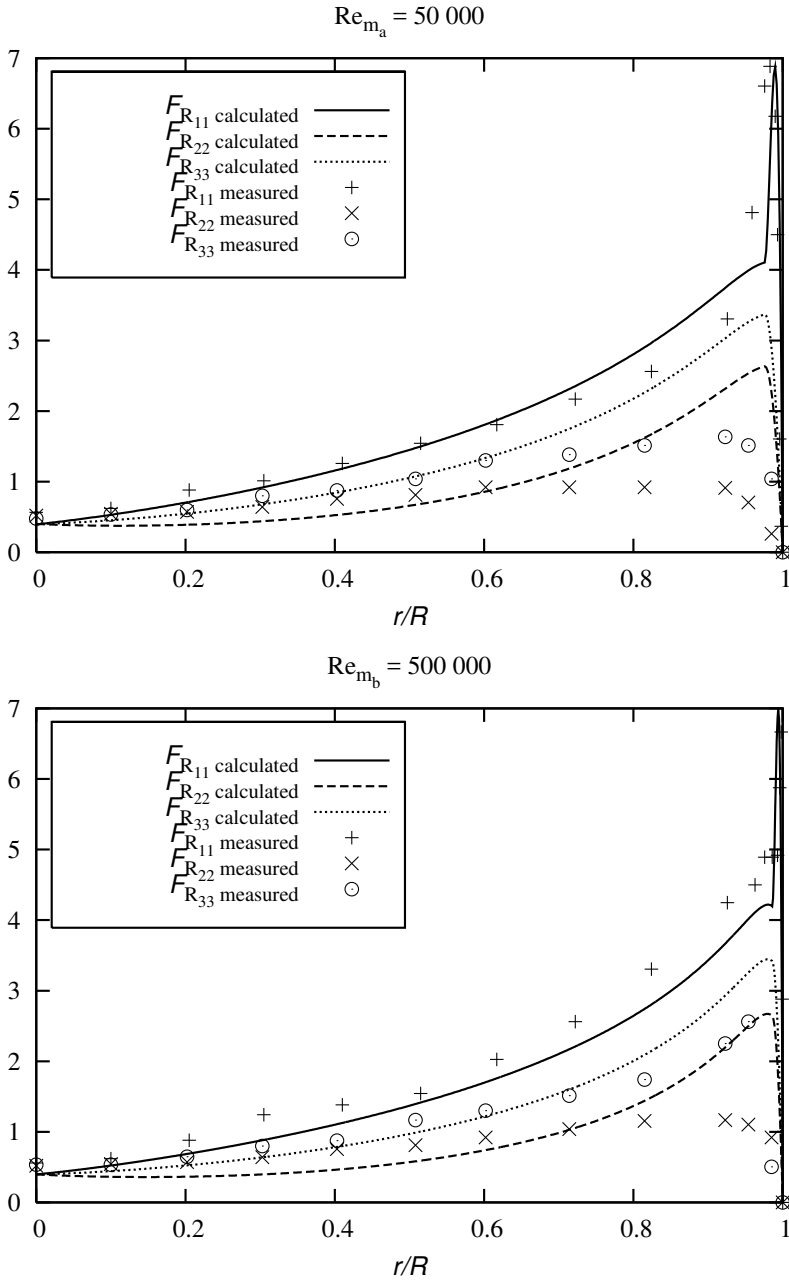


Figure 5. Comparison of calculated turbulent main stresses for two different Re -numbers with the measurement results of Laufer [9].

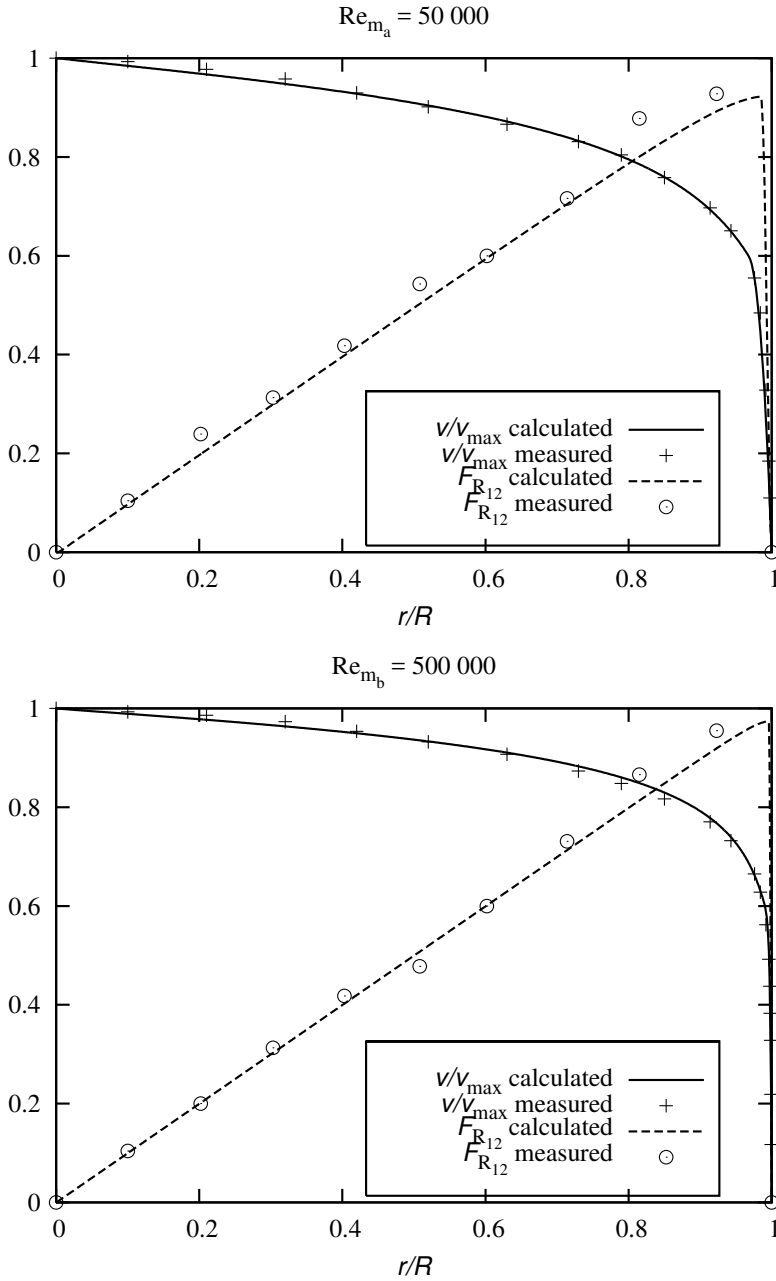


Figure 6. Comparison of the calculated results for the velocity profile and turbulent shear stress with the measurement results of Laufer [9].

For the sake of completeness let us sum up in short the formulas forming the *algebraic version* of the stochastic turbulence model as well. If the expression

$$Y = \frac{l\Omega}{v_*} = \frac{l}{R} \left| \frac{dV}{d\xi} \right| \quad (5.16)$$

is substituted into differential equation (5.7), and the equation – of second order for $dV/d\xi$ – obtained is solved, a differential equation of the form

$$\frac{dV}{d\xi} = \frac{1 \pm \sqrt{1 + 4\kappa^2 \text{Re}_*^2 (l/R)^2 \xi}}{2\kappa^2 \text{Re}_* (l/R)^2}$$

is obtained, where evidently the lower one of the double sign has physical reality (i.e. for a flow in pipes in the points of the cross-section $dV/d\xi \leq 0$). Taking this into account, the above equation is modified to some extent, then its integration produces an integral expression for determining the dimensionless velocity distribution $V(\xi)$:

$$V(\xi) = V_{\max} - \int_0^\xi \frac{2 \text{Re}_* \xi \, d\xi}{1 + \sqrt{1 + 4\kappa^2 \text{Re}_*^2 (l/R)^2 \xi}}, \quad (5.17)$$

where the integration constant V_{\max} is to be calculated using relationship (5.9). For determining the dimensionless velocity scale, on the basis of (5.16) the following formula is obtained:

$$Y(\xi) = \frac{2 \text{Re}_* (l/R) \xi}{1 + \sqrt{1 + 4\kappa^2 \text{Re}_*^2 (l/R)^2 \xi}}. \quad (5.18)$$

By using the following dimensionless scale function, calculation results with a good correspondence with the laboratory measurements are obtained:

$$l/R = (0.35 + 0.15\xi^2) (1 - \xi^2) \{1 - \exp[m(\xi - 1)]\},$$

where $m = \text{Re}_*/25$. When the distributions $Y(\xi)$ and $V(\xi)$ are known – as it has already been expounded concerning the one-equation version –, the formulas (5.12)-(5.14) can be used to determine the following one after the other: the dimensionless dominant turbulent shear stress $\Theta/\rho v_*^2$, the dimensionless specific turbulent dissipation $\epsilon R/v_*^3$ and the dimensionless total potential Π/v_*^2 .

Finally it should be noted that by using a special scale function the integration can be performed in the formula (5.17), resulting in a closed analytic expression for the turbulent profile fully developed in the pipe. The dimensionless scale function is

$$l/R = (1 - \xi^3)/3, \quad (5.19)$$

which substituted into equation (5.17) results after integration in the formula:

$$V(\xi) = V_m - \frac{1}{\kappa} \ln \frac{1 + \xi^{3/2}}{1 - \xi^{3/2}}. \quad (5.20)$$

Since this distribution does not automatically satisfy the zero boundary condition referring to the pipe wall either (i.e. it has a pole in place $\xi = 1$), the zero boundary condition can be fulfilled in this case in the viscous sublayer by a smoothly fitted distribution (Figure 2).

It should be noted that the turbulent velocity distribution calculated by formulas (5.17) and (5.20) of the algebraic version of the stochastic turbulence model is identical ‘within line thickness’ with the velocity distribution calculated on the basis of the one- and two-equation versions, which in turn shows a very good correspondence with the measurement results.

6. Summary

The underdetermined character of the system of differential equations formed by the equation of continuity and the three Reynolds scalar equations of motion can be eliminated on the basis of the stochastic turbulence model by adding the differential equation for the turbulent velocity scale, and the turbulent mean velocity field can be determined by solving the system of equations with a suitable numerical method. When the velocity scale is known, the distribution of the turbulent shear stress can be calculated. This method – where the original system of differential equations containing four members is supplemented with a further differential equation – is termed the *one-equation* version of the stochastic turbulence model.

In order to be able to determine the scalar elements along the main diagonal of the Reynolds turbulent stress tensor, the system of equations to be solved is to be supplemented with a second differential equation as well, i.e. the transport equation of the specific turbulent kinetic energy. After determining the distribution of the turbulent kinetic energy it becomes possible to calculate the distributions of the turbulent main stresses by using the formulas of the stochastic turbulence model. The method obtained – in a three dimensional case built on numerically solving a system of equations constituted by a total of six differential equations and two algebraic equations – forms the *two-equation version* of the stochastic turbulence model.

A comparison of the calculations performed for a flow in a pipe with a circular cross-section for two different Reynolds-numbers with the experimental results of Laufer [9] shows that the results calculated on the basis of the stochastic turbulence model exhibit a satisfactory correspondence with the measurements; for the distribution of velocity and shear stress the calculated and measured results are practically identical; for the turbulent main stresses the correspondence at present can be interpreted with a certain limit of error, which can be improved by a correction of the constants in the model.

References

1. KÁRMÁN, TH. V.: Mechanische Ähnlichkeit und Turbulenz *Proc. 3rd Congress of Applied Mechanics* (1930), 86–93.
2. KOTSCHIN, N. J., KIEBEL, L. A. and ROSE, N. W.: *Theoretische Hydromechanik* Akademie Verlag Berlin (1954) Vol. I, 138–142.
3. GERSTEN, K. and HERWIG, H.: *Strömungsmechanik* Vieweg Braunschweig/Wiesbaden (1992), p 465.
4. KOLMOGOROV, A. N.: The Local Structure of Turbulence in Incompressible Viscous Fluid for Very Large Reynolds Numbers *Dokl. Akad. Nauk. SSSR* 30, 1941, pp 301–305.

5. KLEBANOFF, P. S.: *Characteristics of Turbulence in a Boundary Layer with Zero Pressure Gradient* NACA Report 1247, 1955.
6. PRANDTL, L.: Über ein neues Formelsystem für die ausgebildete Turbulenz *Nachr. Akad. Wiss. Göttingen, Math. Phys. Klasse* 1945, 6–9.
7. BRADSHAW, P., FERRIS, D.H. and ATWELL N.P.: Calculation of Boundary Layer Development Using the Turbulent Energy Equation *Journal of Fluid Mechanics*, **28**, Pt. 3, (1967), 593–616.
8. WILCOX, D. C.: *Turbulence Modeling for CFD (2nd. ed.)* DCW Industries 2000, pp 40, 279.
9. LAUFER, J.: *The Structure of Turbulence in Fully Developed Pipe Flow* NACA Report 1174, 1954.

TWO-FOLD BIFURCATED EQUILIBRIUM PATHS WITH FULL SYMMETRY

ZSOLT GÁSPÁR^{1,2} AND FERENC PEZER²

¹Hungarian Academy of Sciences, Research Group for Computational Structural Mechanics

²Budapest University of Technology and Economics

H-1521 Budapest, Műegyetem rakpart 3-5.

gaspar@ep-mech.me.bme.hu, pezer@biomech.bme.hu

[Received: February 28, 2006]

Abstract. This paper deals with potential energy functions of elastic structures with two symmetry planes. Optimization leads to double cusp catastrophes at the critical point. Catastrophe theory distinguishes 15 classes of double cusp catastrophes. To classify the structures of the equilibrium paths we need some subclassification, due to the special role of the load parameter and because in some cases determinacy of the function is higher than four. Different types of the equilibrium paths are shown for the subclasses.

Mathematical Subject Classification: 74G60, 58K35

Keywords: stability, equilibrium paths, double cusp catastrophe

1. Introduction

Structures with a finite degree of freedom under conservative load are in equilibrium in a position where the gradient of the total potential energy function is zero. If the load is single-parametric, then the equilibrium paths consist of the equilibrium states belonging to the values of the load parameters. The equilibrium states are critical if the Hessian matrix of the energy function is singular. By optimizing the structures it can be achieved that the two lowest critical load parameters are equaled, that means the co-rank of the Hessian matrix is 2 at this critical point.

According to the Splitting Lemma [1] in this case the coordinates describing the position can be transformed in such a way that the total potential energy function splits into two parts: an active and a passive one. The active part is dependent only on two variables and at the critical value of the load parameter it has parts only exceeding the third order. The passive part depends on the other variables and has the form of the Morse saddle.

If the active part is symmetric only in one of its variables, then the function is called half-symmetric. Functions symmetric in both variables are called full symmetric.

The half-symmetric cases are divided by Thompson and Hunt [2] into three groups: the monoclinic, the homeoclinic, and the anticlinic point of bifurcations. (The third one of the above mentioned bifurcations belongs to the elliptic umbilic catastrophe, and the first two pertain to the hyperbolic umbilic catastrophe. The classification

of the hyperbolic umbilic catastrophe is justified by the significant role the load parameter plays in the equilibrium paths.) Equilibrium paths were created for both the perfect and imperfect structures, and the imperfection-sensitivity surfaces were analyzed. In these general cases the exact local examination requires no further analysis of the potential energy function at the critical point than to be approximated with the Taylor series expansion of the function up to the third order. Different types of the critical points are often illustrated by simple models (Thompson and Hunt [2], Gioncu [3], Gáspár [4]).

Thompson and Gáspár [5] made an analysis for all the half-symmetric cases by constantly changing one parameter during the investigation of a family of simple models, and thus identified the transitions between the above mentioned three classifications: the case of the triple root, the parabolic umbilic and the symbolic umbilic catastrophe. In these degenerated cases the exact local investigation required also the fourth order parts. Equilibrium paths in the neighborhoods of these cases were analyzed by Pajunen and Gáspár [6].

Augusti [7] had an investigation of two-fold bifurcations before, where the structures have two symmetry planes. In this case the energy function has a double cusp catastrophe point, and these catastrophes are not included in the 13 catastrophes listed in Thom's theorem (e.g. [8, 1]), because they are produced typically by specially assuming more than five parameters. By the root structure of the bivariate homogeneous cubic form the umbilical catastrophes are to be classified into 4 fundamental types (which are by names: elliptic, hyperbolic, parabolic and symbolic.) Poston and Stewart [9] classified the double cusp catastrophes into 15 types on the basis of the root structures of the binary quartic.

Gáspár [10] has drawn attention to structures where again another type of the double cusp catastrophes appears, by which the primary path can be intersected by any number of secondary equilibrium paths. Samuels and Stevens [11] investigate also the equilibrium paths of the typical double cusp catastrophes, and thus the Taylor expansion of the function is used only up to the fourth order. Gáspár and Lengyel [12] are investigating another family of structures, which creates 4 different types, including two degenerated ones.

The aim of this paper is to specify all the various types of the equilibrium paths of the full symmetry (perfect) structures. It will be shown that with the full symmetry 14 of the 15 types of the double cusp catastrophe are accessible. Some classes have subclasses because of the special role of the load parameter.

2. Accessible classes

Supposed the critical states are identified, where the co-rank of the Hessian matrix of the potential energy is 2, and the Taylor expansion of function up to the fourth order is generated, and the passive part is separated. In the active part (in case of critical load) there are no first and second degree terms, and because of full symmetry in both active variables (x, y) only even exponents are to be found in the factors, thus there are no cubic terms, either. At the critical load ($\lambda = 0$) the 4-jet of the energy

function is a homogeneous quartics:

$$j^4V(x, y, 0) = Ax^4 + Bx^2y^2 + Cy^4. \tag{1}$$

The roots of this polynomial correspond to a maximum number of four lines crossing the origin, where some of the lines may contain compound roots, and the lines may also be complex. Poston and Stewart [9] give transformations for the coefficients of the general homogeneous quartics by means of which they illustrate the connections between these above mentioned types in a three-dimensional space (Figure 1). Each type consists of the functions that belong to the points of the respective sections of space, surfaces, faces or heads, shown below.

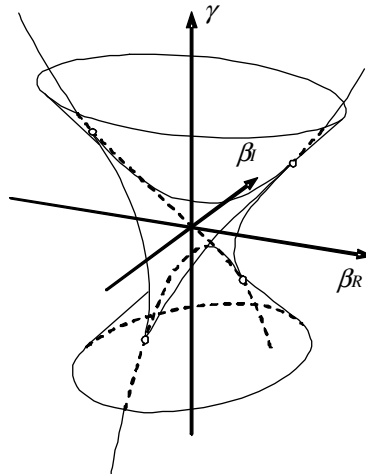


Figure 1. Classes of double cusp catastrophe

By means of the transformations defined by Poston and Stewart the points projected on the cylinder:

$$\begin{aligned} \alpha_R^H &= \text{sign}(A - B + C) , & \alpha_I^H &= 0 , \\ \beta_R^H &= 4 \frac{A - C}{|A - B + C|} , & \beta_I^H &= 0 , \\ \gamma^H &= \frac{A + B/3 + C}{|A - B + C|} . \end{aligned} \tag{2}$$

If $\alpha_R^H = 1$, then we have the points of $\beta_I = 0$ coordinate plain. If $\alpha_R^H = -1$, then a rotation needs to be performed to obtain the resulting section shown in Figure 1:

$$\begin{aligned} \tilde{\alpha}_R^H &= 1 , & \tilde{\alpha}_I^H &= 0 , \\ \tilde{\beta}_R^H &= \beta_I^H , & \tilde{\beta}_I^H &= -\beta_R^H , \\ \tilde{\gamma}^H &= \gamma^H . \end{aligned} \tag{3}$$

Thus we get the point belonging to the coordinate plain $\beta_R = 0$. Thus we generated 14 types out of the total 15, only the points found on the faces of the tetrahedron are not accessible.

Because of full symmetry the homogeneous fourth order polynomial may only have three co-efficients which are different from zero, to classify these, we do not need to use the transformations given by Poston and Stewart [9]. Moreover, since multiplying the whole energy function by a positive constant does not change the equilibrium paths, we only need to use two-dimensional figures to illustrate the classes.

Let us deal with the $A = C = 0$ case separately. Multiplying by a suitable positive constant the polynomial takes the form:

$$\pm x^2y^2. \tag{4}$$

In the other cases we choose the variables x, y in a way, that $|A| \geq |C|$, and after multiplying by a proper positive constant the polynomial yields the form:

$$\pm (x^4 + Bx^2y^2 + Cy^4) \tag{5}$$

where $-1 \leq C \leq 1$. The root lines of the polynomial (5) are as follows:

$$x_{1,2,3,4} = \pm \frac{y}{2} \sqrt{-2B \pm 2\sqrt{B^2 - 4C}}. \tag{6}$$

It can be concluded that in the points of the line $C = 0$ and of the curve $C = B^2/4$ the root can change from real into complex (and vice versa). The classes in case of a positive sign of (5) are illustrated in Figure 2.

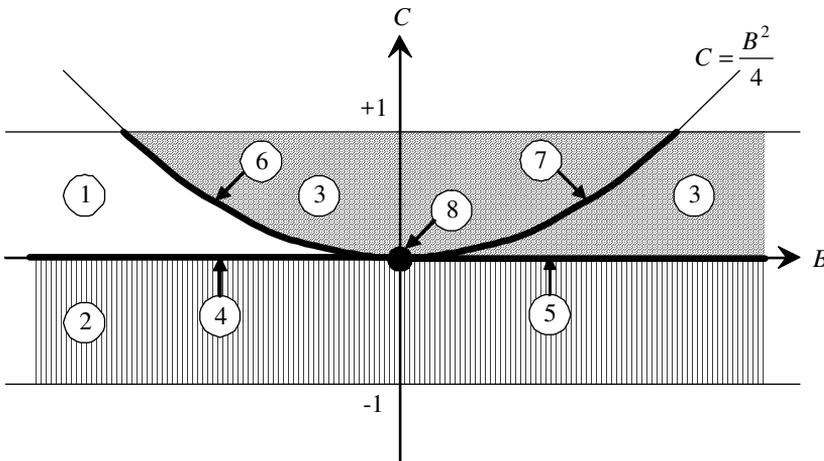


Figure 2. Classes if the sign of (5) is positive

If the sign of (5) is negative the same figure holds, but the sequential number of the types 2-8 gets a cap as well, indicating that in that case they refer to another class. The changing of the sign does not alter types 1 and 2. The root structure of types illustrated in Figure 2 are as follows (for each type it is indicated whether the root

lines are real (r) or complex (c), whether there are compound roots, and it is also shown where the corresponding points are located in Figure 1):

1. r_1, r_2, r_3, r_4 inside the tetrahedron,
2. r_1, r_2, c_3, c_4 outside both tetrahedron and bowls,
3. c_1, c_2, c_3, c_4 inside the top bowl,
4. $r_1 = r_2, r_3, r_4$ on faces of the tetrahedron having only one common point with the top bowl,
5. $r_1 = r_2, c_3, c_4$ on the surface of the top bowl,
6. $r_1 = r_2, r_3 = r_4$ on the top line of self-intersection,
7. $c_1 = c_2, c_3 = c_4$ on the top whiskers,
8. $r_1 = r_2 = r_3 = r_4$ on the common points of the top bowl and the whiskers.

The root structure of the types with cap is identical to that of the ones without cap, but in the description of their location word ‘top’ needs to be changed to ‘lower’. We note that function (4) in case of a positive sign belongs to type 6, but in case of a negative sign naturally it belongs to type $\hat{6}$.

3. Equilibrium paths

If we are to define the equilibrium path in the neighborhood of the critical point, then also the deviation of the load parameter from the critical value in the energy function must be taken into consideration. Because of full symmetry only terms of the state variables with even numbered order can be non-zero. If the coefficient of a term is not zero even in the critical point, then the effects of the load parameter on the coefficient can be neglected compared to the former term. The general form of the quadratic terms is the following:

$$-\lambda(ax^2 + by^2), \quad (7)$$

where a and b are positive numbers, because of the assumption that the critical point under investigation is reached from the state of a stable equilibrium (which means that in case of $\lambda < 0$ the $x = y = 0$ is a stable equilibrium position). The relation between the scale of x and y , and the scale of λ can be defined so that $a = b = 1$. The stability of the equilibrium position is described by calculating the eigenvalues of the Hessian matrix of the energy function in this point. If both are positive, than the position is stable, if there is a negative value, the state is unstable, but if there is a value which is zero, the state is critical.

3.1. Fourth order energy function. The above mentioned simplifications and the definition of the scale are used first to deal with the energy function:

$$V(x, y, \lambda) = x^4 + Bx^2y^2 + Cy^4 - \lambda(x^2 + y^2). \quad (8)$$

If a negative sign is chosen in term (5), then in the cases of the equilibrium paths below the direction of λ should be changed, and as a result the eigenvalues would also change sign. Hence these cases do not require a detailed examination, because by applying the principles the equilibrium paths are easy to obtain by means of the equilibrium paths analyzed here.

The gradient of V:

$$\text{grad } V = \begin{bmatrix} 4x^3 + 2Bxy^2 - 2\lambda x \\ 2Bx^2y + 4Cy^3 - 2\lambda y \end{bmatrix}, \tag{9}$$

the Hessian matrix of V:

$$\mathbf{H} = \begin{bmatrix} 12x^2 + 2By^2 - 2\lambda & 4Bxy \\ 4Bxy & 2Bx^2 + 12Cy^2 - 2\lambda \end{bmatrix}. \tag{10}$$

The line $x = y = 0$ is always a solution of the equation $\text{grad}V = 0$, and it has curve solutions in the coordinate planes $x = 0$ and $y = 0$ as well, and it may also have a further pair of solutions. These solutions are indicated in Table 1. (a suitable independent variable is defined in all cases), and in the last two columns also the eigenvalues of \mathbf{H} are given.

j	x	y	λ	S_{j1}	S_{j2}
1	0	0	λ	-2λ	-2λ
2	0	y	$2Cy^2$	$8Cy^2$	$2(B - 2C)y^2$
3	x	0	$2x^2$	$8x^2$	$2(B - 2)x^2$
4	$\pm y \sqrt{\frac{B-2C}{B-2}}$	y	$\frac{B^2-4C}{B-2} y^2$	$4 \frac{B^2-4C}{B-2} y^2$	$4(2C - B)y^2$
	x	$\pm x \sqrt{\frac{B-2}{B-2C}}$	$\frac{B^2-4C}{B-2C} x^2$	$4 \frac{B^2-4C}{B-2C} x^2$	$4(2 - B)x^2$

Table 1. The equilibrium paths and the eigenvalues of \mathbf{H}

Looking at the table it is easy to see that

- the part $\lambda < 0$ of the always existing equilibrium path $x = y = 0$ is stable, the part $\lambda > 0$ is unstable, and both eigenvalues are negative,
- in cases of the other paths both the numbers and the types of the equilibrium paths change on the lines $B = 2$ and $B = 2C$ further to the curves shown in Figure 2.

It shows that it is sometimes necessary to set up subclasses when investigating the catastrophe types analyzed above. The subclasses created are shown in Figure 3.

To define the pair of solutions marked 4 in the case of $B = 2C$, we have to use the upper solution, and in the case of $B = 2$ the lower solution must be used. In case of being part of both lines, (that is $B = 2$ and $C = 1$):

$$V(x, y, \lambda) = (x^2 + y^2)^2 - \lambda(x^2 + y^2), \tag{11}$$

or transforming it to polar coordinates:

$$V(r, \alpha, \lambda) = r^4 - \lambda r^2. \tag{12}$$

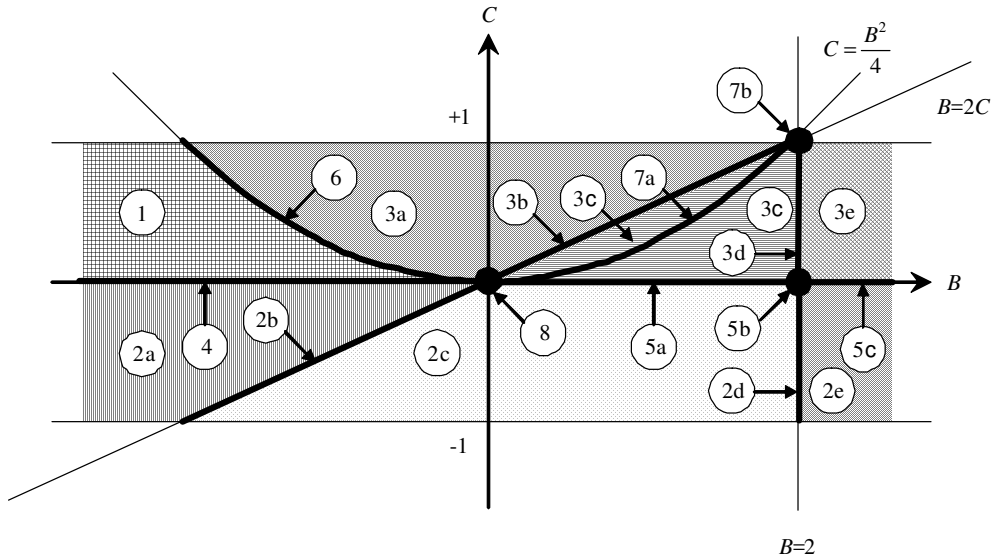


Figure 3. Subclasses if the sign of (5) is positive

since

$$\text{grad } V = \begin{bmatrix} 4r^3 - 2\lambda r \\ 0 \end{bmatrix}, \tag{13}$$

further to the primary equilibrium path $r = 0$, there is a secondary equilibrium surface given by the function $\lambda = 2r^2$. In its points the Hessian matrix is as follows:

$$H = \begin{bmatrix} 8r^2 & 0 \\ 0 & 0 \end{bmatrix}. \tag{14}$$

That means that all points of the surface are critical, and the other eigenvalue is positive. (We note that Gáspár and Mladenov [13] have shown structures which are producing secondary equilibrium surfaces even if there is no full symmetry.)

In Figure 4 we display three cases as an example choosing the energy function from the subclasses 1, 2c and 7b. Here we denote the stable equilibrium paths with continuous lines and the paths containing the critical states with dash-dot lines. In case of the unstable states where the energy function has a saddle point or a maximum point, dashed lines or dotted lines are used, respectively.

If we display the projection of the equilibrium paths on the xy plane, it becomes even more clear what types these paths represent in the corresponding subclasses, and what kind of transitions can become possible between the subclasses. This kind of display does not show the primary equilibrium path which is always the same. Paths represented by upward curves, downward curves and straight lines are denoted by dashed, dotted and continuous lines, respectively. In case of overlapping paths we plot all paths shifted a little. Near the paths we give the sign of the eigenvalues of

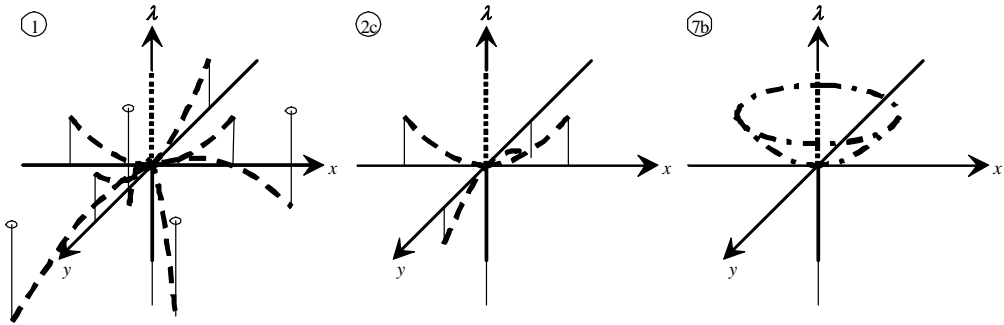


Figure 4. Equilibrium paths of subclasses 1, 2c and 7b

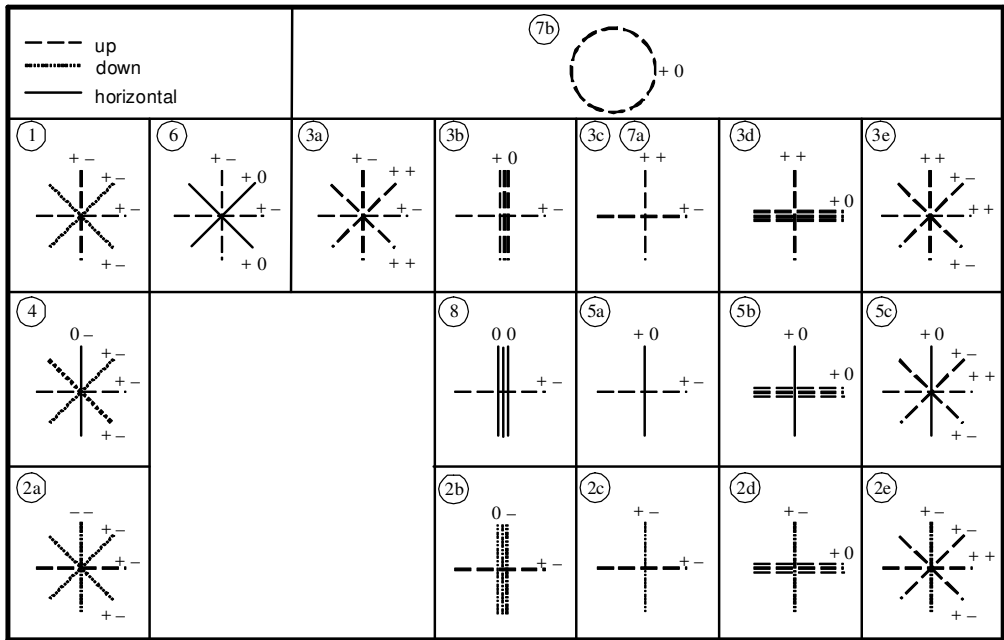


Figure 5. Projections of the equilibrium paths of the subclasses

the Hessian matrix of the energy function. In Figure 5 we display one case for each of all the subclasses, in the same arrangement as it was done in Figure 3. Subclass 8 has 10 neighbors, and subclass 7b has 5 neighbors.

3.2. Considering the determinacy. A function is called [1] k -determinate, if the k segment of the function by a simple transformation of coordinates remains equivalent to all the functions which are composed as a sum of the original function and another one which has terms exceeding k in order.

The function (5) is 4-determinate if there are quadratic polynomials which if multiplied by the first derivative of (5) and then these new polynomials are summed, the result would be either of the fifth order one factors (x^5, x^4y, \dots, y^5) . It can be done if $C \neq 0$ and $C \neq B^2/4$, namely in case of *subclasses 1, 2 and 3*. For example the derivatives are:

$$J_1 = 4x^3 + 2Bxy^2, \quad J_2 = 2Bx^2y + 4Cy^3 \quad (15)$$

and so:

$$x^4y = \frac{C}{4C - B^2}xyJ_1 - \frac{B}{8C - 2B^2}x^2J_2. \quad (16)$$

Because there are no factors with odd numbered order in the energy function under investigation, the functions of the other types are maximum 6-determinate.

In case of *subclasses 4 and 5* $C = 0$ and $B \neq 0$. The function (5) with the addition of the possible sixth order terms has the form:

$$f(x, y) = x^4 + Bx^2y^2 + Dx^6 + Ex^4y^2 + Fx^2y^4 + Gy^6 \quad (17)$$

which together with the

$$x = u - \frac{D}{4}u^3 \quad \text{and} \quad y = v + \left(\frac{D}{4} - \frac{E}{2B}\right)u^2v - \frac{F}{2B}v^3 \quad (18)$$

diffeomorphism (by leaving the factors with higher than the sixth order) can be transformed to the more simple form:

$$g(u, v) = u^4 + Bu^2v^2 + Gv^6. \quad (19)$$

Henceforward it is supposed that $G \neq 0$, and this way it can be shown that (19) is 6-determinate.

In case of *subclasses 6 and 7* $C = B^2/4$ and $B \neq 0$. The function (5) with the addition of the possible sixth order terms has the form:

$$f(x, y) = x^4 + Bx^2y^2 + \frac{B^2}{4}y^4 + Dx^6 + Ex^4y^2 + Fx^2y^4 + Gy^6 \quad (20)$$

which together with the

$$x = u + \left(\frac{F}{B^2} - \frac{E}{2B}\right)u^3 - \frac{F}{2B}uv^2 \quad \text{and} \quad y = v \quad (21)$$

diffeomorphism (by leaving the terms with higher than the sixth order) can be transformed to the more simple form:

$$g(u, v) = u^4 + Bu^2v^2 + \frac{B^2}{4}v^4 + Hu^6 + Gv^6 \quad (22)$$

where

$$H = \frac{4F}{B^2} - \frac{2E}{B} + D. \quad (23)$$

Henceforward it is supposed that $G \neq 0$ and $H \neq 0$, and this way it can be shown that (22) is 6-determinate.

In case of *subclass 8* $B = C = 0$. The function (5) with the addition of the possible sixth order terms has the form:

$$f(x, y) = x^4 + Dx^6 + Ex^4y^2 + Fx^2y^4 + Gy^6 \quad (24)$$

which together with the

$$x = u - \frac{D}{4}u^3 - \frac{E}{4}uv^2 \quad \text{and} \quad y = v \quad (25)$$

diffeomorphism (by leaving the factors with higher than the sixth order) can be transformed to the more simple form:

$$g(u, v) = u^4 + Fu^2v^4 + Gv^6. \quad (26)$$

Henceforward it is supposed that $F \neq 0$ and $G \neq 0$, and this way it can be shown that (26) is 6-determinate.

3.3. Sixth order energy function. The functions of the first three classes are 4-determinate, and therefore there is no need for sixth order factors. In case of *subclasses 4 and 5* based on (19) we analyze the function formulated as follows:

$$V(u, v, \lambda) = u^4 + Bu^2v^2 + Gv^6 - \lambda(u^2 + v^2). \quad (27)$$

The third terms causes only one important change: the former horizontal equilibrium path in the plane $u = 0$ becomes a fourth order curve:

$$\lambda = 3Gv^4. \quad (28)$$

In case of *subclasses 6 and 7* on the basis of (2) we analyze the function formulated as follows:

$$V(u, v, \lambda) = u^4 + Bu^2v^2 + \frac{B^2}{4}v^4 + Hu^6 + Gv^6 - \lambda(u^2 + v^2). \quad (29)$$

In case of *subclass 6* the two former horizontal equilibrium paths become curves, unless there is a very special ratio between the terms. The change of the load parameter:

$$\lambda = \frac{24G - 3HB^3}{8 - 4B}v^4. \quad (30)$$

While investigating subclass 7a we saw that there were no degenerated equilibrium paths, therefore the sixth order terms do not cause major changes. In subclass 7b the secondary equilibrium surface ceases to exist. In both vertical coordinate planes there will always be an upward quadratic curve, but only in case of identical signs of the sixth order terms will there be such (upward curves) equilibrium paths out of the coordinate planes, where

$$u = \pm \left(\frac{G}{H}\right)^{1/4} v \quad \text{and} \quad \lambda = \left(2 + 2\sqrt{\frac{G}{H}}\right)v^2. \quad (31)$$

In case of *subclass 8* based on (26) we analyze the function formulated as follows:

$$V(u, v, \lambda) = u^4 + Fu^2v^4 + Gv^6 - \lambda(u^2 + v^2). \quad (32)$$

Here remains the

$$v = 0 \quad \text{and} \quad \lambda = 2u^2 \quad (33)$$

equilibrium path. In the plane $u = 0$ there will be always a fourth order curve

$$\lambda = 3Gv^4 \quad (34)$$

where the eigenvalues of the Hessian matrix are:

$$24Gv^4 \quad \text{and} \quad 2(F - 3G)v^4. \tag{35}$$

If $3G > F$ the previous threefold solution falls apart, and the new pair of solution:

$$u = \pm \sqrt{\frac{3G - F}{2 - 2Fv^2}}v^2 \approx \pm \sqrt{\frac{3G - F}{2}}v^2, \tag{36}$$

$$\lambda = \frac{3G - F^2v^2}{1 - Fv^2}v^4 \approx 3Gv^4 \tag{37}$$

where the eigenvalues of the Hessian matrix are:

$$24Gv^4 \quad \text{and} \quad -4(F - 3G)v^4. \tag{38}$$

That means one remains the same, the other changes its sign compared to (35). If $3G < F$, (36) is imaginary, consequently out of the three overlapping paths there remains only the (34) equilibrium path. The projections of the equilibrium paths belonging to the energy function (32) are shown in Figure 6.

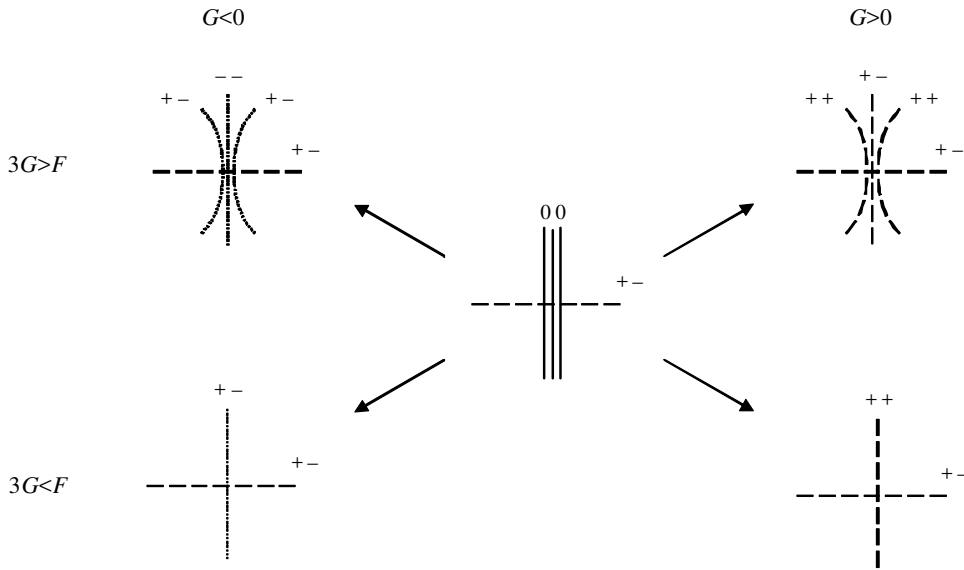


Figure 6. Projections of the equilibrium paths of subclass 8

4. Conclusions

We have analyzed the types of equilibrium paths in case of two coalescing critical loads and of full symmetry. Under these conditions out of 15 types of the double cusp catastrophes 14 are accessible. We have to analyze only 8 of the 14 classes, because in the other cases there is nothing more to do but change the sign in the factors which do not contain a load parameter, and thus the secondary paths will be mirrored on

a horizontal plane, and the eigenvalues of the Hessian matrix describing the stability have to be multiplied by -1.

References

1. POSTON, T., STEWART, I. N.: *Catastrophe Theory and its Applications*. London, Pitman, 1978.
2. THOMPSON, J. M. T., HUNT, G. W.: *Elastic Instability Phenomena*. Chichester, Wiley, 1984.
3. GIONCU, V., IVAN, M.: *Theory of Critical and Post-critical Behaviour of Elastic Structures*. (in Rumanian) Bucuresti: Editura Acad. Resp. Soc. Rom., 1984.
4. GASPÁR, Z.: Stability of elastic structures with the aid of catastrophe theory. In Kollar, L., ed., *Structural Stability in Engineering Practice*. London: Spon. 88-128., 1999.
5. THOMPSON, J. M. T., GASPÁR, Z.: A buckling model for the set of umbilic catastrophes. *Math. Proc. Camb. Phil. Soc.*, **82**, (1977), 497-507.
6. PAJUNEN, S., GASPÁR, Z.: Study of an interactive buckling model - From local to global approach. In Rondal, J., Dubina, D., Gioncu, V., eds, *Proc. 2nd Int. Conf. on Coupled Instabilities in Metal Struct. CIMS'96*. London: Imperial College Press. 35-42, 1996.
7. AUGUSTI, G.: Stabilita' di strutture elastiche elementari in presenza di grandi spostamenti. *Atti Accad. Sci. fis. mat., Napoli, Serie 3a*, **4**(5), (1964).
8. ZEEMAN, E. C.: *Catastrophe Theory: Selected Papers (1972-1977)*. Reading: Addison-Wesley, 1977.
9. POSTON, T., STEWART, I. N.: *Taylor Expansions and Catastrophes. Research Notes in Mathematics*, **7**. London, Pitman, 1976.
10. GÁSPÁR, Z.: Buckling models for higher catastrophes. *J. Struct. Mech.*, **5**, (1977), 375-368.
11. SAMUELS, P. AND STEVENS, J.: Instability of dual eigenvalue fourth-order systems. *J. Struct. Mech.*, **10**(2), (1982), 209-225.
12. GÁSPÁR, Z., LENGYEL, A.: A family of structures for the double cusp catastrophe. *Math. Proc. Camb. Phil. Soc.*, **139**, (2005), 523-540.
13. GÁSPÁR, Z., MLADENOV, K.: Post-critical behaviour of a column loaded by a polar force. In Iványi, M., ed., *Stability of Steel Structures, 1995 Budapest, Further Directions in Stability Research and Design*. Budapest: Akadémiai Kiadó, Vol. II., pp. 897-903, 1996.

OPTIMAL DESIGN OF ELASTO-PLASTIC STEEL FRAMES LOADED BY NORMAL AND EXTREME LOADS AND SUBJECTED TO DISPLACEMENT, DEFORMATION AND STRESS CONSTRAINTS

SÁNDOR KALISZKY AND JÁNOS LÓGÓ

Department of Structural Mechanics
Budapest University of Technology and Economics
H-1111 Budapest, Műegyetem rkp. 3, Hungary
LOGO@ep-mech.me.bme.hu

[Received: December 12, 2005]

Abstract. The paper presents a simple optimal elasto-plastic design method of steel frames and beams constructed of prismatic parts with I shape cross-sections in which the thicknesses of flanges are varying continuously. Two different loading conditions are considered. The normal load (dead load and live load) must be carried in elastic state while it is supposed that under the simultaneous action of an extreme load (explosion, impact, earthquake) and the dead load the structure is in fully plastic state. This state forms the basis of the optimal design. Using a quadratic weight function the determination of the optimal plastic moment distribution is reduced to the analysis of a fictitious linearly elastic structure of the same configuration as the one to be designed but with special bending stiffnesses [1,2,3]. In the knowledge of the optimal plastic moments the corresponding elastic bending stiffnesses and the elastic solution of the original structure subjected to the working load can be determined in which constraints on displacements and stresses are included. Besides, assuming that the complementary strain energy of the residual moments can be considered an average measure of plastic deformations, the plastic behaviour of the structure can also be controlled [4]. The proposed method is described in the form of two elastic solutions coupled in nonlinear form by the design variables. For the solution an iterative procedure and an approximate method are used. The application is illustrated by two numerical examples.

Keywords: optimal plastic design, plastic deformations, mathematical programming

1. Introduction

The application of optimal plastic design methods leads to saving in material but might result in repeated or accumulating plastic deformations and excessive residual displacements which can cause unserviceability or collapse of the structure. To prevent these undesirable phenomena different kinds of constraints are used in the design to control the plastic behaviour of structures (e.g. [1, 2]). Applying the plastic design methods in case of extreme loads (explosion, impact, earthquake) an additional requirement might also be necessary that under the normal working loads in elastic

state the elastic displacements and stresses should not exceed certain limits either. For this purpose further constraints are applied (e.g. [2, 3]).

The aim of this paper is to present a simple optimal plastic design method of elasto-plastic steel frames and beams constructed of prismatic parts with I shape sections in which the thicknesses of the flanges vary continuously. Two different types of load are taken into consideration. The normal load (the dead load \mathbf{P}^0 and the live load \mathbf{P}) must be carried in elastic state. Considering a possible abnormal situation, the structure is subjected together with the dead load also to an extreme load \mathbf{P}^{ex} . It is assumed that under the action of these two loads the structure is in a fully plastic state. In the following this state forms the basis of the optimal design in which the fully plastic moments are the design variables. It will be proved that using a quadratic weight function the optimal solution can be obtained from a fictitious moment distribution of a linearly elastic structure of the same configuration as the one to be designed but with special bending stiffnesses [4, 5, 6]. In the knowledge of the optimal plastic moments the corresponding elastic bending stiffnesses and the elastic solution can be determined in which limits for the elastic displacements and stresses are applied. In addition, it is assumed that the complementary strain energy of the residual moments can be considered an average measure of the residual plastic deformations, therefore introducing appropriate limits the plastic behaviour of the structure can also be controlled [1, 2, 3].

The formulation of the method is simple because it is described in the form of two elastic solutions. These solutions, however, are coupled by the design variables in nonlinear form therefore they cannot be solved independently but generally a certain iterative technique has to be used. Introducing some approximations a simple solution method is also presented. The application is illustrated by two numerical examples.

2. Assumptions, Notations

Consider linearly elastic-perfectly plastic frame-type or beam-type structures constructed of $k = 1, 2, \dots, m$ prismatic parts with I shape cross-sections. The prismatic parts are subdivided into $i = 1, 2, \dots, N_k$ finite elements. Hence, the total number

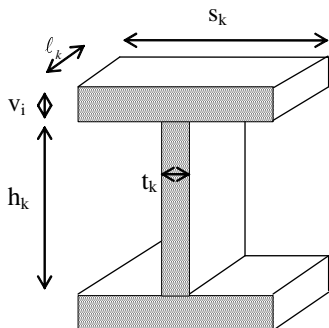


Figure 1. I shape cross-section

of the finite elements is $n = \sum_{k=1}^m N_k$.

The height and thickness of the webs and the width and thickness of the flanges of the cross-sections are denoted by h_k ; t_k and s_k ; v_i , respectively (Figure 1.). The thicknesses v_i of the flanges belonging to the i -th finite element are the design variables, but for convenience, instead of v_i the fully plastic moments M_{pi} of the cross-sections will be introduced as design

variables expressed in terms of v_i in the following form:

$$M_{pi} = \left(\frac{t_k h_k^2}{4} + s_k h_k v_i \right) \sigma_y . \tag{1}$$

Here σ_y is the yield stress of the material.

3. The weight function

In optimal design the objective function plays an important role. In this case the objective function is the weight of the structure expressed in terms of the relationship between the specific weight w_i of the finite element and the fully plastic moment M_{pi} of the cross-section. Since, for practical reasons, the size of cross-sections cannot be reduced below certain limits, we assume that the minimum applicable size is the area of the web. Hence, the corresponding minimum specific weight and plastic moment of the prismatic parts are as follows:

$$w_k^{\min} = t_k h_k \quad \text{and} \quad M_{pk}^{\min} = \frac{t_k h_k^2}{4} \sigma_y . \tag{2}$$

Here, for convenience, it is assumed, that the specific weight of the material is equal to the unit. After a simple calculation the specific weight function can be expressed in the form:

$$\left. \begin{aligned} &\text{if } |M_{pi}| \geq M_{pk}^{\min}, \quad w_i = \frac{1}{2} t_k h_k + \frac{2}{h_k \sigma_y} |M_{pi}|, \\ &\text{if } |M_{pi}| < M_{pk}^{\min}, \quad w_i = w_k^{\min}. \end{aligned} \right\} \tag{3}$$

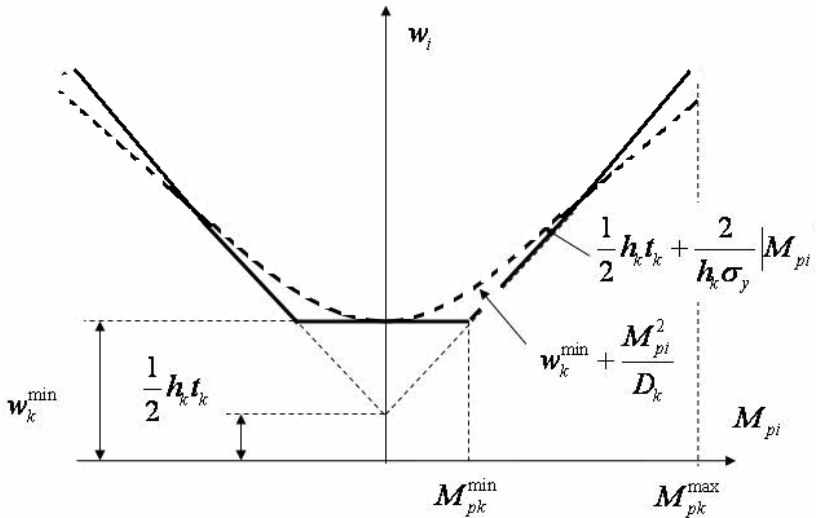


Figure 2. Different functions of the weight

This relations are illustrated by the full lines in Figure 2. On the basis of this weight function analytical solutions cannot be achieved and even the numerical solutions lead

to complicated calculations. To avoid these difficulties the relationships (3) will be approximated by a single quadratic function:

$$w_i = t_k h_k + \frac{M_{pi}^2}{D_k}, \quad (4)$$

illustrated by a dotted line in Figure 2. Here the constant D_k is chosen so, that in the domain $0 \leq |M_{pi}| \leq M_{pk}^{\max}$ the deviation between relations (3) and (4) is zero. The following formula is obtained:

$$D_k = \frac{\left(\frac{t_k h_k^2}{4} + h_k s_k v_k^{\max}\right)^3 \sigma_y^2}{3 h_k s_k^2 (v_k^{\max} - v_k^{\min})^2}. \quad (5)$$

Here v_k^{\max} is the maximum allowable thickness of the flanges. The corresponding plastic moment is as follows:

$$M_{pk}^{\max} = \left(\frac{t_k h_k^2}{4} + h_k s_k v_k^{\max}\right) \sigma_y. \quad (6)$$

The use of the above approximation was suggested by Megarefs and Hodge [4] and later generalized and extended to the optimal design of reinforced concrete structures by Kaliszky [5, 6]. The advantage of this approximation is that the weight function is expressed in term of a single function and because of its quadratic form the use of absolute value can be omitted. These advantages make it possible to reduce the optimum plastic design to a special elastic analysis to be shown next.

4. Optimal plastic design

Denoting by $\mathbf{M}(M_1, M_2, \dots, M_i, \dots, M_n)$ the moments of the structure arising in the plastic limit state under the action of the load ($\mathbf{P}^0 + \mathbf{P}^{ex}$) and making use of the weight function (4) the optimal plastic design can be formulated as below:

$$\min \sum_{k=1}^m \sum_{i=1}^{N_k} \left[w_k^{\min} + \frac{M_{pi}^2}{D_k} \right] \Delta_i \quad (7)$$

subject to

$$\mathbf{G}^* \mathbf{M} + (\mathbf{P}^0 + \mathbf{P}^{ex}) = \mathbf{0}; \quad (8)$$

$$-M_{pi} \leq M_i \leq M_{pi}; \quad (i = 1, 2, \dots, n). \quad (9)$$

Here \mathbf{G}^* is the equilibrium matrix and Δ_i denotes the length of finite elements. Searching for the minimum of the function (7) the constant terms w_k^{\min} can be omitted and because of the continuous variation of the flange thickness and consequently of the plastic moments in an optimal solution all the cross-sections are fully utilized. Hence,

$$|M_i| = M_{pi}; \quad (i = 1, 2, \dots, n) \quad (10)$$

Then relations (9) are automatically fulfilled and equations (9-10) can be written in the form:

$$\min \sum_{k=1}^m \sum_{i=1}^{N_k} \left[\frac{M_{pi}^2}{D_k} \right] \Delta_i \quad (11)$$

subject to

$$\mathbf{G}^* \mathbf{M} + (\mathbf{P}^0 + \mathbf{P}^{ex}) = \mathbf{0}. \quad (12)$$

Here equation (11) can be considered the minimum of the complementary potential energy of an elastic structure at which the prismatic parts have special bending stiffnesses D_k . Consequently, equations (11) and (12) together define the elastic solution of a fictitious structure and the problem of optimal plastic design is reduced to the analysis of an elastic structure of the same configuration as the one to be designed but of constant bending stiffnesses D_k throughout the prismatic parts. The solution of this fictitious elastic problem can be expressed in the following form:

$$\mathbf{M} = \mathbf{F}_k^{-1} \mathbf{G} \mathbf{K}_k^{-1} (\mathbf{P}^0 + \mathbf{P}^{ex}) = \mathbf{K}_k \mathbf{G} \mathbf{F}_k (\mathbf{P}^0 + \mathbf{P}^{ex}). \quad (13)$$

Here \mathbf{G} is the geometrical matrix, \mathbf{F}_k and \mathbf{K}_k denote the flexibility and stiffness matrices corresponding to the special stiffnesses D_k of the prismatic parts. After solving this simple problem the plastic moments which provide the minimum weight of the structure can be obtained:

$$\left. \begin{array}{l} \text{if } |M_i| \leq M_{pk}^{\min}, \quad M_{pi} = M_{pk}^{\min}, \\ \text{if } |M_i| > M_{pk}^{\min}, \quad M_{pi} = |M_i|. \end{array} \right\} \quad (14)$$

This is, however, not the final solution of the problem because the constraints of the elastic displacements, stresses and plastic deformations to be formulated next also have to be satisfied.

5. Constraint on elastic displacements and stresses

The elastic constraints can be formulated in the framework of the elastic analysis of the structure subjected to the normal load $(\mathbf{P}^0 + \mathbf{P})$. First we have to determine the moments of inertia I_i of the cross-sections which correspond to the plastic moments obtained in optimal design and given by equations (13), (14). This calculation leads to the following relation:

$$I_{ki} = \frac{h_k}{2\sigma_y} \left[M_{pi} - \frac{1}{3} M_{pk}^{\min} \right]. \quad (15)$$

In the knowledge of the moments of inertia the elastic limit moments of the cross-sections can also be obtained

$$M_{ki}^0 = \frac{2I_i}{h_k} \sigma_a = \left[M_{pi} - \frac{1}{3} M_{pk}^{\min} \right] \frac{\sigma_a}{\sigma_y}. \quad (16)$$

Here σ_a is the allowable elastic stress.

Introducing limits u_{r0} for the displacements at given points $(r = 1, 2, \dots, s)$ of the structure and denoting by M_{ei} the elastic moments under the action of the normal load $(\mathbf{P}^0 + \mathbf{P})$ the elastic analysis including the displacement and stress constraints are formulated as below:

$$\mathbf{M}_e = \mathbf{F}_e^{-1} \mathbf{G} \mathbf{K}_e^{-1} (\mathbf{P}^0 + \mathbf{P}) = \mathbf{K}_e \mathbf{G} \mathbf{F}_e (\mathbf{P}^0 + \mathbf{P}), \quad (17)$$

$$\frac{1}{E} \sum_{k=1}^m \sum_{i=1}^{N_k} \frac{M_{ei} \bar{M}_{ri}}{I_{ki}} \Delta_i - u_{r0}; \quad (r = 1, 2, \dots, s) \quad (18)$$

$$-M_{ki}^0 \leq M_{ei} \leq M_{ki}^0; \quad (i = 1, 2, \dots, N_k), \quad (k = 1, 2, \dots, m). \quad (19)$$

Here \bar{M}_{ri} denotes the moments calculated from the unit dummy forces \mathbf{P}_r acting at the points ($r = 1, 2, \dots, s$) in the directions of u_{r0} , E is the Young's Modulus of the material and \mathbf{F}_e and \mathbf{K}_e are the flexibility and stiffness matrices corresponding to the moments of inertia I_i given by equations (15) and (16), respectively.

6. Constraint on plastic deformation

To construct the plastic deformation constraint first the elastic moments \mathbf{M}_e^{ex} corresponding to the load $(\mathbf{P} + \mathbf{P}^{ex})$ have to be calculated assuming that the structure is elastic without limits:

$$\mathbf{M}_e^{ex} = \mathbf{F}_e^{-1} \mathbf{G} \mathbf{K}_e^{-1} (\mathbf{P}^0 + \mathbf{P}^{ex}) = \mathbf{K}_e \mathbf{G} \mathbf{F}_e (\mathbf{P}^0 + \mathbf{P}^{ex}). \quad (20)$$

Then the residual moments can be obtained

$$\mathbf{M}_r = \mathbf{M}_p - \mathbf{M}_e^{ex}. \quad (21)$$

As it was stated in Section 1 it is assumed that the complementary strain energy of the residual moments is considered an overall measure of the plastic behaviour of the structure (e.g. [6, 1, 2]). Hence, the plastic deformations can be controlled by the following constraint:

$$\frac{1}{2E} \sum_{k=1}^m \sum_{i=1}^{N_k} \frac{(M_{pi} - M_e^{ex})^2}{I_{ki}} \Delta_i - W_{p0} \leq 0. \quad (22)$$

Here W_{p0} is an appropriately chosen allowable plastic strain energy of the residual moments [1, 2].

7. Solution of problem

Equations (13)-(22) derived above are summarized as follows:

$$\left. \begin{array}{l} \mathbf{M} = \mathbf{K}_k \mathbf{G} \mathbf{F}_k (\mathbf{P}^0 + \mathbf{P}^{ex}) \\ \text{if } |M_i| \leq M_{pk}^{\min}, \quad M_{pi} = M_{pk}^{\min}, \\ \text{if } |M_i| > M_{pk}^{\min}, \quad M_{pi} = |M_i|. \end{array} \right\} (A)$$

$$\left. \begin{array}{l} \mathbf{M}_e = \mathbf{K}_e \mathbf{G} \mathbf{F}_e (\mathbf{P}^0 + \mathbf{P}) \\ \frac{1}{E} \sum_{k=1}^m \sum_{i=1}^{N_k} \frac{M_{ei} \bar{M}_{ri}}{I_{ki}} \Delta_i - u_{r0} \leq 0; \quad (r = 1, 2, \dots, s), \\ -M_{ki}^0 \leq M_{ei} \leq M_{ki}^0; \quad (i = 1, 2, \dots, s), \quad (k = 1, 2, \dots, m), \end{array} \right\} (B)$$

$$\frac{1}{2E} \sum_{k=1}^m \sum_{i=1}^{N_k} \frac{(M_{pi} - M_e^{ex})^2}{I_{ki}} \Delta_i - W_{p0} \leq 0; (C)$$

$$\left. \begin{array}{l} I_{ki} = \frac{h_k}{2\sigma_y} \left[M_{pi} - \frac{1}{3} M_{pk}^{\min} \right]; \\ M_{ki}^0 = \frac{2I_i}{h_k} \sigma_a \end{array} \right\} (D)$$

Here equations (A) provide the optimal plastic moment distribution, equations (B) describe the elastic solution with constraints on the elastic stresses and displacements

and equation (C) stands for the constraint on plastic deformations. These equations are coupled by the design variables M_{pi} throughout equations (D) in nonlinear form therefore the solution of the problem requires the application of an iterative procedure or an approximate solution can be used.

The idea of the approximate method is the proportional reduction of the optimal solution obtained by equation (13). First the optimal plastic moments M_{pi} have to be determined from equations (13), (14). Then making use of the relations (15) and (16) and introducing the unknown slack variables λ_r ; ($r = 1, 2, \dots, s$), κ'_i and κ''_i ; ($i = 1, 2, \dots, n$) and α equations (17)-(19) and (22) can be written in the following form:

$$\mathbf{M}_e = \mathbf{K}_e \mathbf{G} \mathbf{F}_e (\mathbf{P}^0 + \mathbf{P}), \quad (23)$$

$$\frac{1}{E} \sum_{k=1}^m \sum_{i=1}^{N_k} \frac{M_{ei} \bar{M}_{ri}}{I_{ki}} \Delta_i - \lambda_r u_{r0} = 0; \quad (r = 1, 2, \dots, s), \quad (24)$$

$$-\frac{\sigma_a}{\sigma_y} \kappa'_i M_{ki}^0 = M_{ei} = \frac{\sigma_a}{\sigma_y} \kappa''_i M_{ki}^0; \quad (i = 1, 2, \dots, N_k), \quad (k = 1, 2, \dots, m), \quad (25)$$

$$\frac{1}{2E} \sum_{k=1}^m \sum_{i=1}^{N_k} \frac{(M_{pi} - M_{ei}^{ex})^2}{I_{ki}} \Delta_i - \alpha W_{p0} = 0. \quad (26)$$

Solving these equations the maximum value of the slack variables can be calculated

$$\Psi = \max(\lambda_r, \kappa'_i, \kappa''_i, \alpha); \quad (r = 1, 2, \dots, s), \quad (i = 1, 2, \dots, n). \quad (27)$$

Then the plastic moment distribution \bar{M}_{pi} which satisfies the constraints of the elastic displacements, stresses and plastic deformations and, at the same time, can carry the load $(\mathbf{P}^0 + \mathbf{P}^{ex})$ in fully plastic state can be approximated in the following form

$$\left. \begin{array}{l} \text{if } \Psi \leq 1, \quad \bar{M}_{pi} = M_{pi}; \\ \text{if } \Psi > 1, \quad \bar{M}_{pi} = \frac{2\sigma_f}{h_k} \Psi I_{ki} + \frac{1}{3} M_{pk}^{\min}; \end{array} \right\} \quad (i = 1, 2, \dots, N_k), \quad (k = 1, 2, \dots, m). \quad (28)$$

If $\Psi \leq 1$, then the constraints are not active and therefore the exact solution is identical with the optimal plastic moment distribution given by equations (13), (14).

If $\Psi > 1$ then the application of the plastic moments \bar{M}_{pi} calculated from equation (15) on the basis of the increased moments of inertia assures the satisfaction of the constraints and larger than M_{pi} , therefore the structure can carry the load $(\mathbf{P}^0 + \mathbf{P}^{ex})$ in plastic state.

8. Examples

In the following the application of the method is illustrated by presenting the results of the optimal plastic design of two different structures. A computer program system was elaborated in standard FORTRAN language to solve the problem numerically. The finite element program provides the necessary information for the mathematical programming part. The optimization algorithm is based on sequential quadratic programming [7]. Due to the nature of the test problems the computer times were not significant and conducting a few iterations the optimal solutions were found.

Example 1. A Beam

Consider an elasto-plastic continuous simple supported beam subjected to dead load, normal and extreme loads shown in Figures 3.a-c. Corresponding to the two spans the beam is constructed of two prismatic parts with the length $\ell_1=5.40\text{m}$ and $\ell_2=4.50\text{m}$, respectively.

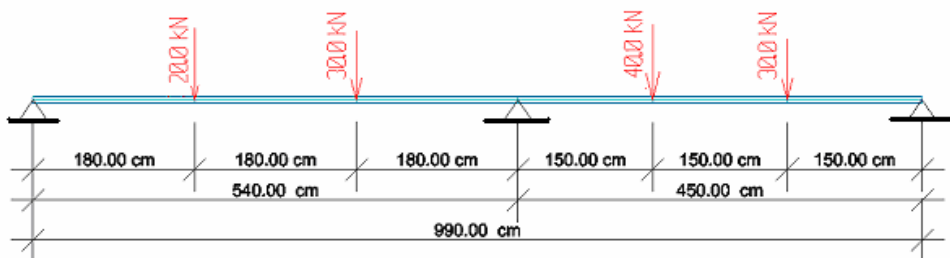


Figure 3.a. Dead load

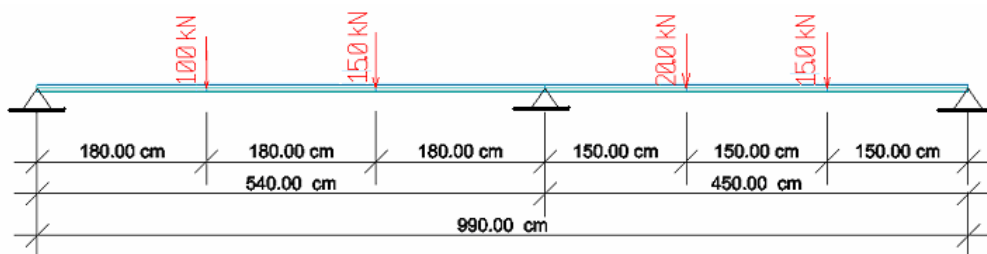


Figure 3.b. Normal load

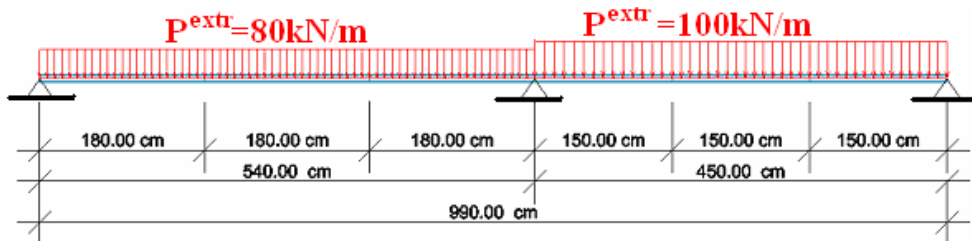


Figure 3.c. Extreme load

The I-shape cross-sections (Figure 1) of the two prismatic parts have the following data: $h_1 = 100\text{ mm}$, $t_1 = 10\text{ mm}$, $s_1 = 100\text{ mm}$ and $h_2 = 100\text{ mm}$, $t_2 = 12\text{ mm}$, $s_2 = 100\text{ mm}$. The limits of the thickness of the flanges are $v_1^{\min} = v_2^{\min} = 5\text{ mm}$ and $v_1^{\min} = v_2^{\min} = 40\text{ mm}$, respectively.

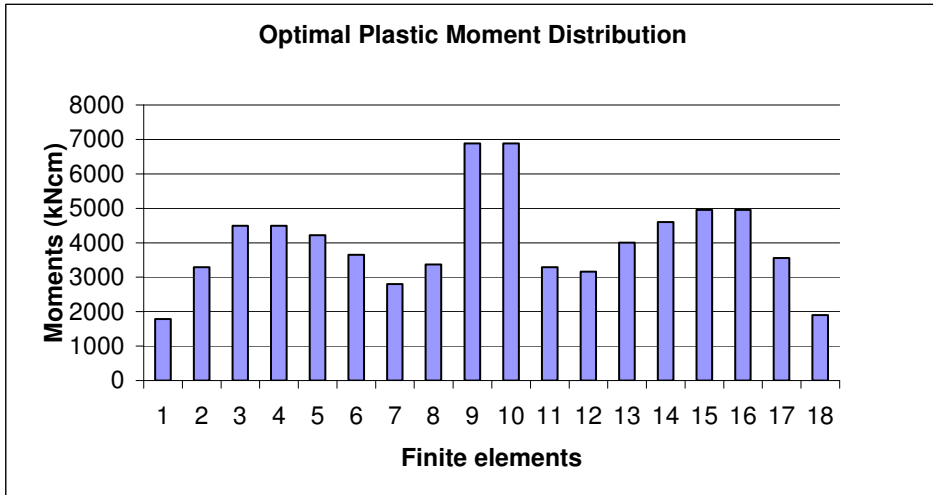


Figure 4. Plastic moment distribution

Each prismatic part is subdivided into 9 finite elements ($n=18$) with equal lengths $\Delta_1 = 60$ cm and $\Delta_2 = 50$ cm, respectively. The material constants are $\sigma_y = 21$ kN/cm² and $E = 21000$ kNcm².

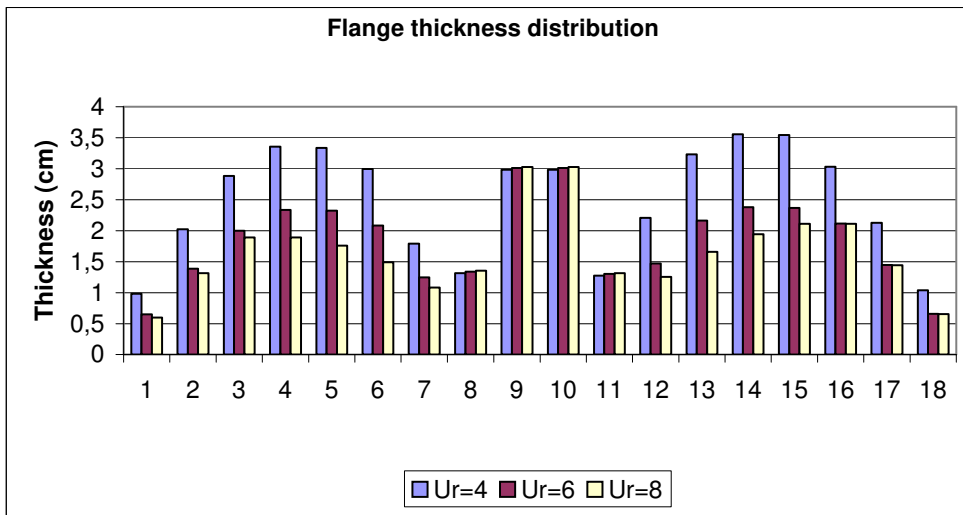


Figure 5. Flange thickness distribution at different elastic limit displacements

The allowable plastic strain energy of the residual moments is assumed to $W_{p0} = 20$ kNm. Three different elastic limit displacements $u_{01} = 4, 6, 8$ cm and $u_{02} = 4, 6, 8$ cm are taken into account at the middle of the spans.

The results are shown in Figures 4-5. In Figure 4 the variation of the optimal plastic moment distribution of the beam is plotted in case of $u_{01} = u_{02} = 8\text{cm}$. Figure 5 shows the distribution of the thicknesses of the flanges along the beam for different limit displacements.

Example 1. A Frame

Consider an elasto-plastic rectangular frame shown in Figure 6.a. The frame is subjected to dead load \mathbf{P}_0 , normal load \mathbf{P} and extreme load \mathbf{P}^{ext} given in Figure 6.b. The extreme load corresponds to the impact of a vehicle with mass $m=800\text{ kg}$ and velocity 5 m/s which is equivalent to $\mathbf{P}^{ext}=200\text{ kN}$ [7]. The beam and the columns are constructed of two prismatic parts ($k=1, \dots, 6$) as it is shown in Figure 6.a. and each prismatic part has 3 finite elements ($i = 1, \dots, 18$) with lengths $\Delta_1 = 75\text{ cm}$ and $\Delta_2 = 60\text{ cm}$, respectively.

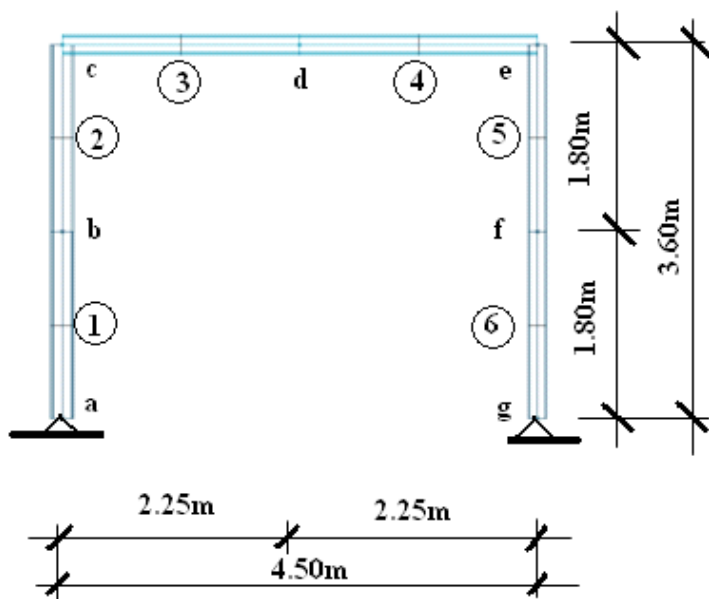
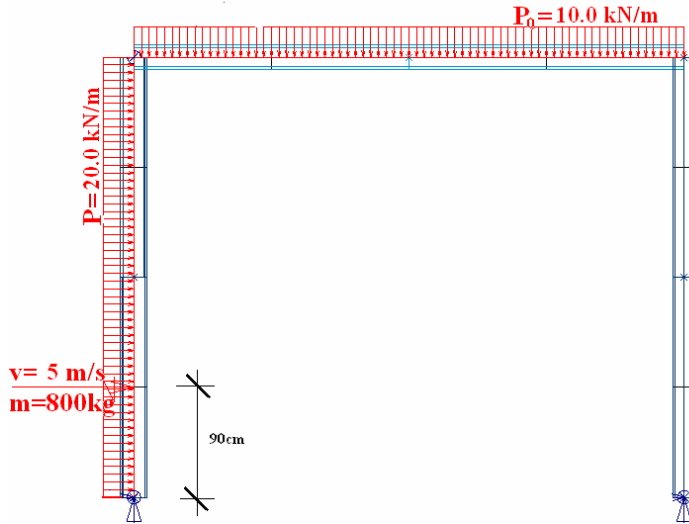


Figure 6.a. Dimensions of the frame

The allowable plastic strain energy of the residual moments is assumed to be $W_{p0} = 10\text{ kNm}$. Two different elastic limit displacements $u_{01} = 7.5; 12.5\text{cm}$ and $u_{02} = 7.5; 12.5\text{cm}$ are taken into account at points b and d, respectively. The prismatic parts have I-type cross-sections (Figure 1) with the assumed dimensions shown in Table 1. In the Table the minimum and maximum values of the thickness of the flanges are also given.

Solving the example the thicknesses of the flanges calculated at the finite elements in case of $u_{01} = u_{02} = 7.5\text{ cm}$ are shown in the last but one column of Table 1, while

Figure 6.b. Dead load P_0 , normal load P and extreme load P^{ext}

in the last column the constant thicknesses to be applied along the prismatic parts are given.

Table 1. Data of the cross-sections and the results

k	ℓ_k [cm]	h_k [mm]	t_k [mm]	s_k [mm]	v_k^{\min} [mm]	v_k^{\max} [mm]	v_i [mm]	$v_{k,applied}$ [mm]
1	60	220	12	140	8	44	12.2 23.0 27.6	28
2	60	220	14	160	8	50	27.5 31.5 35.5	36
3	75	200	12	160	8	50	40.6 30.5 30.0	42
4	75	200	12	160	8	50	29.6 29.1 28.6	30
5	60	180	12	140	8	44	36.7 24.2 18.6	38
6	60	180	10	140	8	44	13.6 8.00 13.6	14

9. Conclusions

The presented method can be used for the optimal plastic design of steel frames and beams composed of prismatic parts with I type cross-sections and subjected to three different kinds of loads. Under the action of the dead load and normal load the structure must be in elastic state with limited displacements and stresses while the extreme load together with the dead load is carried in fully plastic state when the plastic deformations are also controlled. Using a quadratic weight function the plastic optimal design is reduced to the analysis of a fictitious elastic structure with special bending stiffnesses. Because the equations are coupled by the design variables in nonlinear form an iterative procedure should be applied to the solution. The convergence of this iteration is generally good and the solution does not need lengthy calculations.

The approximate method is very simple and provides a good estimation of the optimal solution. It is on the safe side regarding the load carrying capacity of the structure and fulfils all constraints. The proposed method can be also applied to the optimal design of trusses.

Acknowledgement. The present study was supported by the Hungarian National Scientific and Research Foundation (OTKA) (grant T 042993) and Janos Bolyai Scholarship.

References

1. KALISZKY, S.: *Elasto-plastic analysis with limited plastic deformations and displacements*. Journal of Mechanics of Structures and Machines, **24**, (1996), 39-50.
2. KALISZKY, S. and LÓGÓ, J.: *Layout and shape optimization of elastoplastic disks with bounds on deformation and displacement*. Journal of Mechanics of Structures and Machines, **30**(2),(2002), 177-191.
3. SCHITTKOWSKI, K.: *NLPQL: A FORTRAN subroutine solving constrained nonlinear programming problems*. Annals of Operation Research, Vol.5 (1985/86), 485-500.
4. MEGAREFS, G. J. and HODGE JR., P. G.: *Method for plastic design of frames*. Journal of Struct. Division. Proc. of Am. Soc. Civil Engrs., **89**(ST.1), (1963), 197-214.
5. KALISZKY, S.: *Economic design by the ultimate-load method*. Concrete and Constructional Engineering. TX. (1965), 365-372, 424-433, 461-467.
6. KALISZKY, S.: *On the optimal design for reinforced concrete structures*. Acta Tech. Acad. Sci. Hung., **60**, (1968), 257-264.
7. KALISZKY, S. and LÓGÓ, J.: *Layout Optimisation of Elasto-plastic Structures Subjected to Normal and Extreme Loads*, In: *The Seventh International Conference on Computational Structures Technology*, ed. by B.H.V. Topping, CD paper 20 pages, Civil-Comp Press. ISBN 0-948749-94-6, 2004.

Notes for Contributors

to the Journal of Computational and Applied Mechanics

Aims and scope. The aim of the journal is to publish research papers on theoretical and applied mechanics. Special emphasis is given to articles on computational mechanics, continuum mechanics (mechanics of solid bodies, fluid mechanics, heat and mass transfer) and dynamics. Review papers on a research field and materials effective for teaching can also be accepted and are published as review papers or classroom notes. Papers devoted to mathematical problems relevant to mechanics will also be considered.

Frequency of the journal. Two issues a year (approximately 80 pages per issue).

Submission of Manuscripts. Submission of a manuscript implies that the paper has not been published, nor is being considered for publication elsewhere. Papers should be written in standard grammatical English. Two copies of the manuscript should be submitted on pages of A4 size. The text is to be 130 mm wide and 190 mm long and the main text should be typeset in 10pt CMR fonts. Though the length of a paper is not prescribed, authors are encouraged to write concisely. However, short communications or discussions on papers published in the journal must not be longer than 2 pages. Each manuscript should be provided with an English Abstract of about 50–70 words, reporting concisely on the objective and results of the paper. The Abstract is followed by the Mathematical Subject Classification – in case the author (or authors) give the classification codes – then the keywords (no more than five). References should be grouped at the end of the paper in numerical order of appearance. Author’s name(s) and initials, paper titles, journal name, volume, issue, year and page numbers should be given for all journals referenced.

The journal prefers the submission of manuscripts in \LaTeX . Authors should prefer the $\mathcal{A}\mathcal{M}\mathcal{S}\text{-}\text{\LaTeX}$ article class and are not recommended to define their own \LaTeX commands. Visit our home page for further details concerning the issue how to edit your paper.

For the purpose of refereeing, two copies of the manuscripts should initially be submitted in hardcopy to an editor of the journal. The eventual supply of an accepted-for-publication paper in its final camera-ready form (together with the corresponding files on an MS–DOS diskette) will ensure more rapid publication. Format requirements are provided by the home page of the journal from which sample \LaTeX files can be downloaded:

<http://www.uni-miskolc.hu/home/web/pumns/mechanics>

These sample files can also be obtained directly (via e-mail) from a member of the Editorial Board, Gy. Szeidl (Gyorgy.SZEIDL@uni-miskolc.hu), upon request.

Twenty offprints of each paper will be provided free of charge and mailed to the correspondent author.

The Journal of Computational and Applied Mechanics is abstracted in Zentralblatt für Mathematik and in the Russian Referativnij Zhurnal.

Responsible for publication: Rector of the Miskolc University

Published by the Miskolc University Press under the leadership of Dr. József PÉTER

Responsible for duplication: works manager Tibor KOVÁCS

Number of copies printed: 200

Put to the Press on March 1, 2011

Number of permission: TU 2011-120-ME

HU ISSN 1586–2070

A Short History of the Publications of the University of Miskolc

The University of Miskolc (Hungary) is an important center of research in Central Europe. Its parent university was founded by the Empress Maria Teresia in Selmecebánya (today Banská Štiavnica, Slovakia) in 1735. After the first World War the legal predecessor of the University of Miskolc moved to Sopron (Hungary) where, in 1929, it started the series of university publications with the title *Publications of the Mining and Metallurgical Division of the Hungarian Academy of Mining and Forestry Engineering* (Volumes I.-VI.). From 1934 to 1947 the Institution had the name Faculty of Mining, Metallurgical and Forestry Engineering of the József Nádor University of Technology and Economic Sciences at Sopron. Accordingly, the publications were given the title *Publications of the Mining and Metallurgical Engineering Division* (Volumes VII.-XVI.). For the last volume before 1950 – due to a further change in the name of the Institution – *Technical University, Faculties of Mining, Metallurgical and Forestry Engineering, Publications of the Mining and Metallurgical Divisions* was the title.

For some years after 1950 the Publications were temporarily suspended.

After the foundation of the Mechanical Engineering Faculty in Miskolc in 1949 and the movement of the Sopron Mining and Metallurgical Faculties to Miskolc, the Publications restarted with the general title *Publications of the Technical University of Heavy Industry* in 1955. Four new series - Series A (Mining), Series B (Metallurgy), Series C (Machinery) and Series D (Natural Sciences) - were founded in 1976. These came out both in foreign languages (English, German and Russian) and in Hungarian.

In 1990, right after the foundation of some new faculties, the university was renamed to University of Miskolc. At the same time the structure of the Publications was reorganized so that it could follow the faculty structure. Accordingly three new series were established: Series E (Legal Sciences), Series F (Economic Sciences) and Series G (Humanities and Social Sciences). The latest series, i.e., the series H (European Integration Studies) was founded in 2001. The eight series are formed by some periodicals and such publications which come out with various frequencies.

Papers on computational and applied mechanics were published in the

Publications of the University of Miskolc, Series D, Natural Sciences.

This series was given the name Natural Sciences, Mathematics in 1995. The name change reflects the fact that most of the papers published in the journal are of mathematical nature though papers on mechanics also come out.

The series

Publications of the University of Miskolc, Series C, Fundamental Engineering Sciences

founded in 1995 also published papers on mechanical issues. The present journal, which is published with the support of the Faculty of Mechanical Engineering as a member of the Series C (Machinery), is the legal successor of the above journal.



Journal of Computational and Applied Mechanics

Volume 7, Number 2 (2006)

Contents

Contributed Papers

- Alexander BARDELICK and Michael J. WORSWICK: Evaluation of load control end-feed in hydroforming of pre-bent dp600 steel tube using the extended stress-based forming limit curve (xsflc) failure criterion 133–154
- Tibor CZIBERE: Evaluation of load control end-feed in hydroforming of pre-bent dp600 steel tube using the extended stress-based forming limit curve (xsflc) failure criterion 155–188
- Zsolt GÁSPÁR and Ferenc PEZER: Two-fold bifurcated equilibrium paths with full symmetry 189–200
- Sándor KALISZKY and János LÓGÓ: Optimal design of elasto-plastic steel frames loaded by normal and extreme loads and subjected to displacement, deformation and stress constraints 201–212